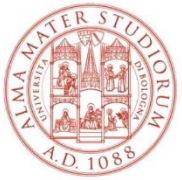

ALMA MATER STUDIORUM
UNIVERSITÀ DI BOLOGNA

DOTTORATO DI RICERCA IN

MECCANICA E SCIENZE AVANZATE DELL'INGEGNERIA

Ciclo 36°

Settore Concorsuale: 09/A2

Settore Scientifico Disciplinare: ING-IND/13

DEVELOPMENT OF GRIPPING DEVICES BASED ON ELECTROADHESIVE FORCES

Presentata da: ***Dott. Federico Bertolucci***

Coordinatore Dottorato **Supervisore**

Ch.mo Prof. Ing. Lorenzo Donati **Dott. Ing. Irene Fassi**

Esame finale anno 2024

Abstract

In a context of technological innovation, the aim of this thesis is to develop a technology that has gained interest in both scientific and industrial realms. This technology serves as a viable alternative to outdated and energy-consuming industrial systems. Electro-adhesive devices (EADs) leverage electrostatic forces for grasping objects or adhering to surfaces. The advantage of employing electrostatics lies in its adaptability to various materials without compromising the structure or chemistry of the object or surface. These benefits have led the industry to explore this technology as a replacement for costly vacuum systems and suction cups currently used for handling most products. Furthermore, the broad applicability of this technology extends to extreme environments, such as space with ultra-high vacuum conditions. Unfortunately, research in this area has yet to yield practical results for industrially effective gripper prototyping. This is primarily due to the inherent complexity of electro-adhesive technology, which operates on basic capacitive principles that does not find satisfying physical descriptions. This thesis aims to address these challenges through a series of studies, starting with the manufacturing process and testing of an EAD that has become the standard in our laboratory. It then delves into material and electrode geometry studies to enhance system performance, ultimately presenting potential industrial applications of the technology. All the presented results are encouraging, as they have yielded shear force values three times higher than those previously reported in the literature. The various applications have demonstrated the significant effectiveness of EADs as brakes or, more broadly, in exerting shear forces. This opens up the possibility of utilizing cutting-edge technologies to push the boundaries of technology to the fullest.

Summary

Summary iii

Chapter 1. Introduction and Motivation 1

Chapter 2. Electroadhesion 4

2.1 Electroadhesion working principle and modeling 4

2.2 Electroadhesion performance evaluation 11

2.3 Electro Adhesive Devices (EAD) 13

Chapter 3. Additive manufacturing technologies 17

3.1 3D Manufacturing technologies overview 17

Chapter 4. Inkjet printing technology 25

4.1 Introduction 25

4.2 Droplets deposition 27

4.3 Continuous Inkjet Printing 29

4.4 Drop on Demand Inkjet Printing 30

4.5 DoD inkjet printer description 32

Chapter 5. Inkjet printing of conductive materials: inks comparison 36

5.1 Introduction 36

5.2 Materials and methods 37

5.3 Results 39

Chapter 6. Assessing the relationships between interdigital geometry quality and inkjet printing parameters 43

6.1 Introduction 43

6.2 Geometry design and manufacturing 46

6.3 Experimental design 47

6.4 Measurements and analysis 49

6.5 Results and discussions 50

Chapter 7. EAD manufacturing 56

7.1 EAD design 56
7.2 EAD manufacturing 57
7.3 EAD test 59
Chapter 8. Increasing the performance of Electro-adhesive devices via inkjet printing 63
8.1 Introduction 63
8.2 Experimental design 64
8.3 Results and Discussion 71
Chapter 9. Empiric study of electrodes geometry design and its impact on EA performances 79
9.1 Introduction 79
9.2 Geometry study 80
9.3 2nd characterization study 86
Chapter 10. Some Applications 108
10.1 Introduction 108
10.2 Normal Force empirical evaluation 108
10.3 Shear Force as brake system for Embossed Paper 112
Chapter 11. Conclusions 114

List of figures

Figure 1 Volume element with dipole momentum **p** 5
Figure 2 Force diagram on two substrate with friction and electrostatic force acting 10
Figure 3 a) Electrostatic Shear Stress evaluation on shear force experiment. b) Normal force evaluation 11
Figure 4 a) Load signal vs time, the maximum give the EA force value . b) Breakdown experiment, voltage and current monitor. c) Breakdown optical image 12
Figure 5 Bottom up process building an EAD: Electrodes are deposited on plastic substrate and then insulating material is deposited 14
Figure 6 EAD a) bi-layer configuration and b) uni-layer configuration 15
Figure 7 Uni and Bi-layer configurations comparison on ESS performances on different objects 16
Figure 8 a) Different geometries of EAD electrodes. b) Comparison of shear pressure of different geometries 16
Figure 9 Schematic of spin coating process 20
Figure 10 Doctor Blade Coating technique for thin film deposition 21
Figure 11 Screen Printing manual technique 22
Figure 12 Spray coating technique scheme 23
Figure 13 Inkjet Printer example 24
Figure 14 Drop ejection from the nozzle with undesired satellites that provoke non-uniform line borders 26
Figure 15 Pictorial view of the region in which the rheological properties of a solution are optimal for DoD inkjet printing[40] 27
Figure 16 a) Continuous inkjet printing. b) Drop on Demand inkjet printing 30
Figure 17 a) Piezoelectric Nozzle. b) Voltage waveform and its effect on the ink in the reservoir 31
Figure 18 JetLab 4xl front view. Highlighted the pressure regulator system, x-y stage, or printing plate, the printing head with cartridges on it, and the heating system 32
Figure 19 Pressure control, from the left: Stages of purge control, monitor indicating the pressure in mmHg, Manual pressure regulator to finely tune the pressure on the device. 34
Figure 20 Drop view through IR camera system 35

Figure 21 Camera for printing inspection viey, normal to the printing plate 35
Figure 22 Example of drops and lines printed. Optical image taken with Dinoscope microscope. 40
Figure 23 Example of array printed. Optical image captured with optical Dino microscope 40
Figure 24 Example of arrays for the interdigital geometry 41
Figure 25 - Anapro DGP-40LT-15C on Caplinq Polyimide: a) distinct droplet spaced by 0.3 mm. b) part of an interdigitated geometry with droplet spaced by 0.17 mm along x and 0.2 mm. c) Droplets, line and array of Smart'ink 42
Figure 26 - Interdigital geometry with nominal dimensions and relevant parameters 46
Figure 27 - a) Microfab Jetlab 4xl, b) control panel for droplet formation parameter settings 47
Figure 28 - Example image of a sample acquired with Zeiss Stereo Discovery V20 optical microscope 50
Figure 29 - Interval plot of the mean value and standard deviation of the gap against drop spacing along the x-axis 51
Figure 30- Interval plot of the mean value and standard deviation of the gap against drop spacing along the y-axis 51
Figure 31 - Interval plot of the mean value and standard deviation of the gap against the printing speed 52
Figure 32 - Interval plot of the mean value and standard deviation of the gap against the nozzle temperature 52
Figure 33 - Example of printed sample with interconnected arrays (Δx = 80 μm, Δy = 110 μm, vp = 10 mm/s, Tn = 40°C) 53
Figure 34 - Individual value plot of the minimum value of the gap 53
Figure 35 - Individual value plot of gap length 54
Figure 36 - a) Example of disconnection at the array beginning (Δx = 140 mm, Δy = 170 mm, vp = 30 mm/s, Tn = 35°C); b) Example of intermediate disconnection (Δx = 110 mm, Δy = 140 mm, vp = 20 mm/s, Tn = 40°C) 54
Figure 37 Binarized image of a sample including internal holes, which are the black spots in the white comb-shapes (Δx = 140 mm, Δy = 170 mm, vp = 10 mm/s, Tn = 35°C 55
Figure 38 Interdigital geometry parameters 57
Figure 39 EAD manufacturing process steps 59
Figure 40 – Test bench for shear force evaluation and circuit schematic 60

Figure 41 - Electrical scheme of the voltage divider interfacing with the IPC input module EL3104 61

Figure 42 - Electrical scheme of the current monitor interfacing with the IPC input module EL3104 61

Figure 43 a) Sample layers structure: the dielectric insulating layer (light blue region) and the electrodes (grey rectangles) are deposited on a Polyimide deposition substrate. The thicknesses of the insulating and deposition layer are denoted with $tins$ and $tsub$ b) Interdigital geometry scheme: the EAD length (L) and width (W) define the electro-active area of the device. The comb-fingers width (w) and the electrodes gap (g) are highlighted. The main rectangle at the left and right of the active area are conductive regions to better power the device. 65

Figure 44 a) JetLab DoD inkjet printer system. b) Voltage monopolar waveform applied to the piezoelectric nozzle c) The printing plate defines the x-y plane (4), the motion of the printing head (1) defines the z-axis. (2) represents the ink cartridge. (3) is the PI printing substrate. .. 66

Figure 45 Dielectric ink deposition procedure: a) The electrodes are deposited and cured in oven. B) Then the first dielectric layer is printed out. c) The first dielectric layer is deposited and cured. Two more layers are deposited in the same way. c) EAD layer structure section and view from above. The ended sample is cured in oven for one hour. 68

Figure 46 Testbench for ESS assessment and Breakdown results CAD schematic draw. Both Voltage and Current are monitored as signals directly from the power supply and directly from the device, with a current monitor (CM) in series to the device, and a voltage monitor (VD) parallel to the device. 70

Figure 47 Optical image of an EAD produced by DoD inkjet printing 72

Figure 48 Preliminary ESS test to find the highest sustainable voltage value, which is found to be 3.2kV. An experiment at 0kV has been performed to evaluate the friction coefficient of the dielectric ink. The red line suggests the quadratic behaviour only for illustrative purposes. 72

Figure 49 Electro-adhesive shear stress at breakaway. Blue dots represent the test of the PI layer and the red square the dielectric ink, both used as gripping layers. The mean over all the samples is reported for each voltage value, and errors are evaluated as the standard deviation. 74

Figure 50 Weibull probability density function (WBL PDF) on the left, and probability paper on the right side representing experimental breakdown failure results of 14 samples. 74

Figure 51 Optical image of the electrical breakdown occurred within two comb-fingers. The dielectric layer has been removed by the energy released. 75
Figure 52 EADs with three different areas (L x W) for scalability evaluation. a) area of 6x24 = 144 mm2, b) area of 20x24 = 480 mm2, c) area of 40x24 = 960 mm2 76
Figure 53 ESS results regarding samples of three different areas: 144 mm^2 (green squares), 480 mm^2 (red rhombuses), 960 mm^2 (blue dots). 77
Figure 54 Different gap - EAD of PI - DC and AC ESS evaluation 81
Figure 55 Different Width - DC voltage ESS evaluation 82
Figure 56 Different materials under test, 2 electrodes configuration - ESS evaluation with DC voltage 83
Figure 57 Comparison between the pulling direction of the testing substrate with respect to the longest gap line 84
Figure 58 Evaluation of ESS performance activating the EAD before and after the contact with the testing substrate 85
Figure 59 Frequency scan at 4kV to understand its influence on ESS performance 86
Figure 60 Geometries chosen for second experimental campaign 89
Figure 61 Friction test results 91
Figure 62 AC results for Mylar 93
Figure 63 AC Results for Polyimide 94
Figure 64 AC results for PEEK 95
Figure 65 AC results for PET 96
Figure 66 AC Results for PEN 96
Figure 67 DC results Mylar 99
Figure 68 DC results PEEK 100
Figure 69 DC results Polyimide 100
Figure 70 DC results PET 101
Figure 71 DC results PEN 102
Figure 72 Mean power and activation energy of the different geometries and different materials 105
Figure 73 Handles to empirical evaluation of normal EA performance 109
Figure 74 Electrode geometry designed for EAD working in a delta robot application 111
Figure 75 EAD mounted on end-effector of delta robot 111
Figure 76 Normal prehension on a carboard pack 112

Figure 77 Top left: Manufacturing scheme of EAD produced. Right: DC and AC voltage results for ESS performance. Bottom Left: holding force with respect to normal paper..... 113

List of tables

Table 1 Differences in printing parameteres and rehological propertities of the two conductive ink 38

Table 2 - Experimental design summary..... 48

Table 3 - Complete experimental campaign conducted following the Run Order..... 48

Table 4 - ANOVA p-values (bold = significant factor, confidence level α = 5%) for the analysis on the mean value and standard deviation of the gap..... 50

Table 5. Waveform parameters settings for conductive Anapro Ag nanoparticle-based ink and Xerox xdi-dcs dielectric ink 67

Table 6 Production time of the EAD with the three different areas. The production time represents the total time for one sample and the time to be added for any other unit to be manufactured. 77

Table 7 Intuitive comparison between materials studied 88

Table 8 Capacitance of the EADs with different geometry and dielectric substrate..... 106

Table 9 Successful normal prehension cases..... 110

Chapter 1. Introduction and Motivation

The use of electroadhesion (EA) has garnered significant interest in recent decades, both in the scientific and industrial domains. This phenomenon, based on electrostatic or Coulombic forces, enables the manipulation of objects with diverse material properties and shapes, positioning itself as an alternative to similar technologies such as vacuum suction and magnetic adhesion[1]. Devices employing electro-adhesion, commonly referred to as electro-adhesive devices (EADs), provide a solution for object manipulation and, more broadly, offer a means to enhance friction between surfaces[2]. Their appeal is further heightened by the cost-effectiveness of the materials employed, primarily plastics, and the minimal energy consumption required for their operation. These systems operate capacitively and, when electrically activated, induce an electrostatic attraction between their surface and that of an object[3]. This force is harnessed for various purposes, including object manipulation, immobilization, or deceleration. This technology offers an advantageous alternative to vacuum suction due to its reduced energy consumption and greater adaptability to various substrates, even though, in general, it may exhibit less force. Unlike magnetic adhesion, which is dependent on the material's magnetic properties, whether ferromagnetic or rare-earth elements, electro-adhesion is versatile, making it well-suited for applications in automation and, notably, soft robotics[4]. Prototyping grippers with flexible and stretchable materials that readily conform to the object's structure is a feasible endeavor. Notably, two startups, Grabit Inc. and OmniGrasp, have ventured into introducing this technology to the market. The first one has introduced to the market a gripper with a deformable silicon-based end effector, designed to conform well to the irregular surface of fragile objects, such as fruits and eggs. The second one employs electro-adhesion as a brake on conveyor belts for handling packages. One of the early applications of electro-adhesion was an electrostatic chuck for handling silicon wafers. Since these are delicate objects with a surface that must not be contaminated by external agents and having a very smooth and uniform surface, they are perfect candidates for being handled by EADs[5]. The

interest in electro-adhesion has also extended to more advanced research environments, particularly in the aerospace sector, where vacuum systems may be ineffective for obvious reasons. Materials such as Polyimide, already widely employed in ultravacuum conditions, have been utilized to produce various EADs, providing a lightweight and adaptable solution for extreme space applications[6]. In terrestrial domains, the technology has found success in the packaging industry for the handling, management, and monitoring of packaging materials, particularly in aseptic environments within the food sector. In this context, Adaptronics S.r.l. was founded in Bologna by Dr. Agostini, with a mission to transfer university-developed technology into commercial products. Despite its wide range of potential applications, electro-adhesion is still in an early-stage phase when it comes to prototyping. While it had its initial application back in the 1960s[7], a fully-fledged, industrially viable prototype has not yet emerged. This is primarily due to the significant uncertainty surrounding several essential aspects of an electro-adhesive device. These uncertainties span from the materials used to the geometry of its constituent parts, and even to the theoretical models attempting to describe the physics of the system. These models often reference specific cases and have not managed to provide a sufficiently satisfying and general explanation[3], [8], [9]. The difficulty in modeling has underscored the need for empirically validated experiments. It is within this context that the work presented in this thesis comes to life. Beginning with the foundational knowledge of electro-adhesive technology and the manufacturing process for standard laboratory devices, a journey of refinement of techniques and the exploration of new materials and geometries to enhance electro-adhesive performance has been undertaken. The most appropriate manufacturing method to achieve the set objectives is examined, comparing it with various other processes within the realm of additive manufacturing, or 3D manufacturing. Inkjet printing has proven to be the most versatile technology for prototyping purposes[10]. Subsequently, an investigation into the printing of conductive inks to achieve the best print quality in terms of geometric precision and line uniformity is presented. A study on the relationship between print parameters and the print outcome on a substrate is conducted using statistical techniques such as Design of Experiments (DoE). To enhance the adhesive performance of the devices, a prototype of a device entirely printed using inkjet printing, with a particular focus on the electroactive substrate, has been constructed. This prototype has resulted in achieving values three times higher than those reported in the literature for shear force, a standard measure of electro-adhesive performance. Furthermore, a study of the electrode geometry of electro-adhesive devices, a fundamental component in creating the electric field that generates the electrostatic force, is presented. The study aims to find the

optimum balance between materials used and geometry to maximize adhesion on a specific material, in this case, poly-laminated cardboard. These studies have led to a new definition of standards and have facilitated a deeper understanding of the physical nature of electro-adhesive grip, often conflicting with predictive models found in the literature. Practical examples of how electro-adhesive devices are utilized are also provided.

Chapter 2. Electroadhesion

Electroadhesion (EA), also known as electrostatic adhesion, is a phenomenon in which two surfaces are attracted to each other due to the presence of electric charges. The technologies to create an EA effect have been extensively studied and have improved significantly over the last few decades, based on two fundamental physical principles[11]. The first principle, known as the Johnsen-Rahbek effect, dates back to the early 20th century. It relies on the force that arises between a flat, polished, high-resistance semi-conductive material and a metal surface when a voltage is applied between them[12][13]. The second is based on Coulombic forces arising between charges on the two surfaces. This principle, which is the focus of study in this thesis, has gained popularity in recent years due to several key factors, including its potential for attaching a wide range of materials and surfaces and its adaptability to various application environments. For these reasons several research groups have developed prototypes for fabric and textile handling[14], wall climbing robots[15], and microgrippers[16], to mention a few. The first company to commercialize this technology was Grabit, Inc. that proposed an auto-layering robot with and electroadhesive gripper, a gravity-fed conveyor with an electroadhesive film embedded and a conveyor electroadhesive belt acting like a magnet, holding virtually anything it touches in place. This physical principle has also been integrated with other technologies, such as gecko-inspired adhesives and dielectric elastomer transducers, to enhance adhesion performance and increase the adaptability of devices that utilize EA for gripping non-uniform objects[17].

2.1 Electroadhesion working principle and modeling

To generate electrostatic force, charges coupling is required. The most common way to generate a charged surface in EA application, is to polarize a dielectric material (or insulator) by applying high voltage, usually from 1 to a maximum of 10 kV. In this type of materials, all charges are attached to specific atoms or molecules and all they can do is move a bit within the atom or molecule, in a microscopic displacement.[18] When the voltage is applied creating an electric field **E** penetrating in the dielectric medium, electrons and the nuclei are pushed against

and in the direction of the field, respectively. They are separated until electrical balance is reached. This physical system is called *electric dipole* and has a dipole moment **p** with the same direction of **E**. This induced dipole moment is proportional to the field:

$$\boldsymbol{p} = \alpha \boldsymbol{E} \tag{1}$$

The constant of proportionality is called *atomic polarizability* and depends on the detailed structure of the atom or molecules. When dealing with a non homogeneous material, the polarizability can be considered as a tensor with three directions. The overall effect of creating dipole moments in a bulk material is to *polarize* the material itself. The *polarization* is defined as the number of dipole moments per unit volume, or

$$\boldsymbol{p} = \boldsymbol{P}\, d\boldsymbol{\tau} \tag{2}$$

Where $d\tau$ is the volume element. The total potential, in this context, is

$$V(\boldsymbol{r}) = \frac{1}{4\pi\varepsilon_0}\int_V \frac{\hat{\boldsymbol{r}}\cdot\boldsymbol{P}(\boldsymbol{r}')}{\boldsymbol{r}^2} d\tau \tag{3}$$

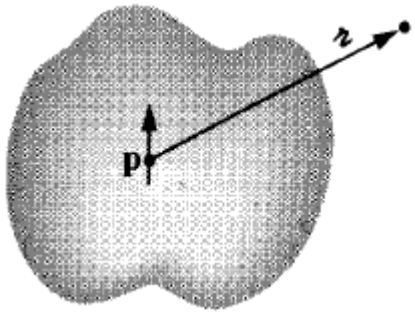

Figure 1 Volume element with dipole momentum **p**

With some simple algebra calculations, the last equation becomes

$$V(\boldsymbol{r}) = \frac{1}{4\pi\varepsilon_0}\oint_S \frac{\sigma_b}{r} da + \frac{1}{4\pi\varepsilon_0}\int_V \frac{\rho_b}{r} d\tau \tag{4}$$

Where $\rho_b = -\boldsymbol{\nabla}\cdot\mathbf{P}$ and $\sigma_b = \boldsymbol{P}\cdot\hat{\boldsymbol{n}}$ are respectively the volume charge density and the surface density, describing a bound charges inside the material. This result describes an actual accumulation of charge in the physical material and, in particular, the bound charges present on the surface. So, the polarization itself creates an electric field inside the matter. So, the overall electric field arising from a polarized material can be considered as the field attributable to bound charge plus the field due to free charges, that might consist of electrons on a conductor or ions embedded in the dielectric material. In general, free charges are due to defects or any charge residual that is not a result of polarization. The total charge density can be written as:

$$\rho = \rho_b + \rho_f \quad (5)$$

And Gauss's law reads

$$\varepsilon_0 \nabla \cdot \boldsymbol{E} = \rho = \rho_b + \rho_f = -\nabla \cdot \boldsymbol{P} + \rho_f \quad (6)$$

Where **E** is the total field. Combining the equations one of the most common equation in electrostatic theory is obtained

$$\nabla \cdot (\varepsilon_0 \boldsymbol{E} + \boldsymbol{P}) = \rho_f \quad (7)$$

$$\boldsymbol{D} = \varepsilon_0 \boldsymbol{E} + \boldsymbol{P} \quad (8)$$

It's known as *electric displacement* vector. In terms of **D,** Gauss's law reads

$$\nabla \cdot \boldsymbol{D} = \rho_f \quad (9)$$

Or, in integral form

$$\oint \boldsymbol{D} \cdot d\boldsymbol{a} = Q_{f_{enc}} \quad (10)$$

where $Q_{f_{enc}}$ denotes the total free charge enclosed in the volume. The parallel between **E** and **D** is subtle.

As I described the polarization as the lining up of electric dipoles with the electric field, for many substances the polarization is proportional to the field:

$$\boldsymbol{P} = \varepsilon_0 \chi_e \boldsymbol{E} \quad (11)$$

The constant of proportionality χ_e is called the *electric susceptibility* of the medium and its value depends on the microscopic structure of the material. If the dielectric is placed inside an external electric field, **P** cannot be computed directly from the last equation. A redundant effect of the electric field that polarized the material and the polarization that produces an electric field occur. It is simpler to deal with **D**:

$$\boldsymbol{D} = \varepsilon_0 \boldsymbol{E} + \boldsymbol{P} = \varepsilon_0 \boldsymbol{E} + \varepsilon_0 \chi_e \boldsymbol{E} = \varepsilon_0 (1 + \chi_e) \boldsymbol{E} \quad (12)$$

So

$$\boldsymbol{D} = \varepsilon \boldsymbol{E} \quad (13)$$

Where

$$\varepsilon = \varepsilon_0(1 + \chi_e) \quad (14)$$

is called *permittivity* of the material. In fact, ε_0 is called *permittivity of the free space* as there's no matter to polarize, so the susceptibility is 0. The materials differ form the *relative permittivity*, or *dielectric constant*, defined as

$$\varepsilon_r = 1 + \chi_e = \frac{\varepsilon}{\varepsilon_0} \quad (15)$$

A crystal is generally easier to polarize in some directions than in others. In bulk material is useful to consider the susceptibility as a tensor with nine coefficients, for each direction.

A useful consideration regarding the energy stored in the dielectric system can be easily done by considering a capacitor, and the work needed to charge it

$$W = \frac{1}{2}CV^2 \quad (16)$$

The capacitance value, when dealing with dielectric material filling the capacitor, exceeds the vacuum capacitance value of a factor of the dielectric constant, and so the work to charge it

$$C = \varepsilon_r C_{vac} \quad (17)$$

From the general formula for the energy stored in any electrostatic system, in the case of a filling dielectric material, the following case is obtained (demonstration on references).

$$W = \frac{\varepsilon_0}{2}\int \varepsilon_r E^2 \, d\tau = \frac{1}{2}\int \boldsymbol{D} \cdot \boldsymbol{E} \, d\tau \quad (18)$$

The force that the dielectric material suffers when placed in an electric field

When placed in contact with another surface, the polarized dielectric material induces image charges on it, creating a coulombic attractive force between the two surfaces. This electrostatic adhesive force is used to move or grab objects. The force generated in this way depends on the voltage applied and on its dynamic, as well as on depends on physical parameters of the entire system, from the dielectric properties of the material that influence the polarization behavior, to the waveform of the voltage applied.

In general, the force experiences a certain delay compared to the dynamics of the voltage applied to the system due to the physics of the system itself[19]. Therefore, both during the activation and deactivation of the potential, the force will take some time to exert itself and to dissipate[20]. This delay significantly impacts on the effectiveness of the technology applications, especially in potential industrial environment applications where very short

activation times are required. Therefore, the study of the technology, particularly of the materials used, must pay close attention to optimizing this aspect, especially during the prototyping phase of a device employing such technology. General models describing EA have been presented in literature based on the classical Maxwell stress tensor theory, considering a 2-D simplification [3][21][9]. The layout of the conductive plates that provide potential to the dielectric will be discussed later, but it is certainly worth noting that the electric field generated distributes within the dielectric according to the geometry of the two plates and the intensity of the potential.

Coulomb's law is the fundamental expression of this phenomenon, represented by equation (19):

$$\overline{\boldsymbol{F}}_{\boldsymbol{EA}} = \boldsymbol{Q}\,\overline{\boldsymbol{E}} \qquad (19)$$

$\overline{F}_{EA}$ is a 3x1 vector whose component represents the x, y, and z component of the electrostatic force, Q is the test charge, E is the electric field and is defined as:

$$\overline{\boldsymbol{E}}\,(\mathrm{r}) = \frac{\mathbf{1}}{\mathbf{4}\pi\boldsymbol{\varepsilon}_{\mathbf{0}}}\int_{V}\frac{\boldsymbol{\rho}\,(\boldsymbol{r}')}{\boldsymbol{r}^{2}}\,\hat{\boldsymbol{r}}\,\boldsymbol{d\tau} \qquad (20)$$

Equation (20) quantifies the electric field E as a volume integral of charge density ρ divided by the square of the distance from the source charge. ε_0 is the vacuum permittivity, with $\varepsilon_0 = 8.85 \times 10^{-12}\frac{C^2}{N\cdot m^2}$.

It is notable that the electric field distribution not only relies on the volume in consideration but also on how charges are distributed in space, dictated by the geometrical configuration of conductors where source charges are located. Consequently, calculating the electric field for complex-shaped conductors common in practical applications becomes challenging. Given these complexities, a more generalized discussion of the Coulomb force is more relevant since the EA force expression in equation (19) may not be applicable for modeling and simulating real-world scenarios. For a generic volume containing stationary charges in a vacuum, equation (19) can be substituted with the volume integral in equation (21):

$$\overline{\boldsymbol{F}}_{\boldsymbol{EA}} = \int_{V}\boldsymbol{\rho}\,\overline{\boldsymbol{E}}\,\boldsymbol{d\tau} \qquad (21)$$

The force per unit of volume is defined by the force density vector:

$$\overline{f} = \rho\,\overline{E} \qquad (22)$$

Now, considering Maxwell's first equation:

$$\nabla \cdot \bar{E} = \frac{\rho}{\varepsilon_0} \quad (23)$$

And by substituting (23) in (24) we derive:

$$\overline{f} = \varepsilon_0(\nabla \cdot \bar{E})\ \bar{E} \quad (24)$$

To move forward, we introduce the Maxwell Stress Tensor, a 3x3 matrix defined as:

$$T_{ij} \equiv \varepsilon_0[E_j E_i - \frac{1}{2}\delta_{ij}E^2] \quad (25)$$

Where i and j are the x, y, and z coordinates, while δ_{ij} is the Kronecker delta.

The total 3x3 matrix is usually represented by the symbol $\overleftrightarrow{T}$ and can be also written as follows:

$$\overleftrightarrow{T} \equiv \varepsilon_0\, \bar{E} \otimes \bar{E} - \varepsilon_0 \frac{1}{2}(\bar{E} \cdot \bar{E}) \quad (26)$$

It's important to extend these considerations to cases where the field generated by stationary charges propagates in matter. By modifying equation (22) to:

$$\overline{f} = \rho_f\, \bar{E} \quad (27)$$

Where ρ_f is the free charge density, we can readily obtain equation (28):

$$\overline{f} = (\nabla \cdot \overline{D})\ \bar{E} \quad (28)$$

Where D is the electric displacement field defined as:

$$\overline{D} = \varepsilon_0\, \varepsilon_r\ \bar{E} \quad (29)$$

for linear, isotropic, and homogeneous dielectric materials.

With ε_r called dielectric constant Following the earlier steps, the Maxwell Stress tensor is now defined as:

$$\overleftrightarrow{T} \equiv \overline{D} \otimes \bar{E} - \frac{1}{2}\bar{E} \cdot \overline{D} \quad (30)$$

In conclusion, the divergence of equation (28) is exactly equal to what we found in equation (24). Therefore, equations (24) and (30) can be rephrased as:

$$\overline{f} = \nabla \cdot \overleftrightarrow{T} \quad (31)$$

As a result, substituting equation (31) into equation (21), the electro-adhesive force can be expressed as:

$$\overline{F}_{EA} = \int_V \nabla \cdot \overleftrightarrow{T}\, d\tau \qquad (32)$$

Which, thanks to Gauss theorem becomes:

$$\overline{F}_{EA} = \int_S \overleftrightarrow{T} \cdot \hat{n} d\sigma \qquad (33)$$

$\overleftrightarrow{T}$ is an electrostatic stress tensor (electrodynamic stress tensor in the most general case and represents the force per unit of area acting on the surface S. T_{ij} elements are the force per unit of area oriented in the i^{th} direction acting on an element of surface oriented in the j^{th} direction. Diagonal terms of $\overleftrightarrow{T}$ (i.e. T_{xx}, T_{yy}, T_{zz}) represent pressures while off-diagonal terms (i.e. $T_{xy}, T_{xz}\ etc.$) are the shear stresses [22].

Equation (33) offers a simplified model of the practical scenario in EAD applications. However, the real situation, involving the combine action of the electroadhesive force and the static friction component $\overline{F}_S = \overline{F}_N \mu_S$, the situation becomes more complex:

- $\overline{F}_{EA}$ and $\overline{F}_S$ are not entirely independent as they mutually influence and are influenced by the effective contact area between the EAD and the object.

- A similar relationship exists for the total adhesive force $\overline{F}_{EA}$, which relies on the loading force $\overline{F}_N$, itself capable of altering the contact area.

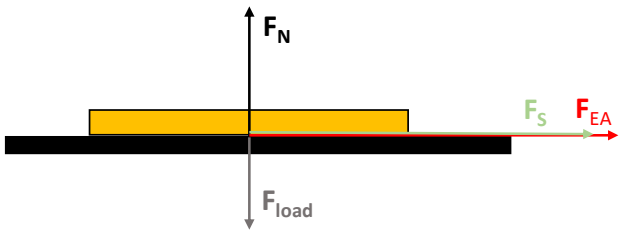

Figure 2 Force diagram on two substrate with friction and electrostatic force acting

While these interdependencies are unavoidable in real-world scenarios, it is still feasible to empirically assess adhesive force as a relatively independent variable by increasing the loading force to the saturation point of the effective contact area. The same level of independence cannot be claimed for $\overline{F}_{EA}$and $\overline{F}_S$, which interact in a more intricate and less easily definable manner. The approach proposed here, however, remains an approximate method for practical EA force evaluation. The dynamic nature of environmental conditions, surface properties, and the effects of polarization/depolarization on material responses make it challenging to predict EAD

performance using analytical models. Therefore, empirical modeling based on experimental data emerges as the essential approach for a comprehensive evaluation of EAD performance, significantly contributing to the design and manufacturing process of EADs.

2.2 Electroadhesion performance evaluation

The performance of a capacitive device utilizing electroadhesion is associated with two key aspects: the electrostatic force it generates and the maximum electric field[9], or voltage, the device can withstand before an electrical breakdown event occurs[23]. The electrostatic force produced by a device employing electroadhesion is typically evaluated in two different configurations. The first, more common and yielding better results, involves assessing the shear force or shear pressure, referred to as Electrostatic Shear Stress (ESS), generated by the adhesion between the capacitive system and the surface of an object or substrate, hereafter named *testing, or test substrate*. The experiment, of an intuitive and straightforward nature, entails pulling away from contact the testing material while keeping the device stationary, or vice versa, once the device is powered, collecting force data using a load cell (Figure 3). The force-versus-time graph, particularly the peak force at the initial detachment, is considered the point of maximum electro-adhesive force.

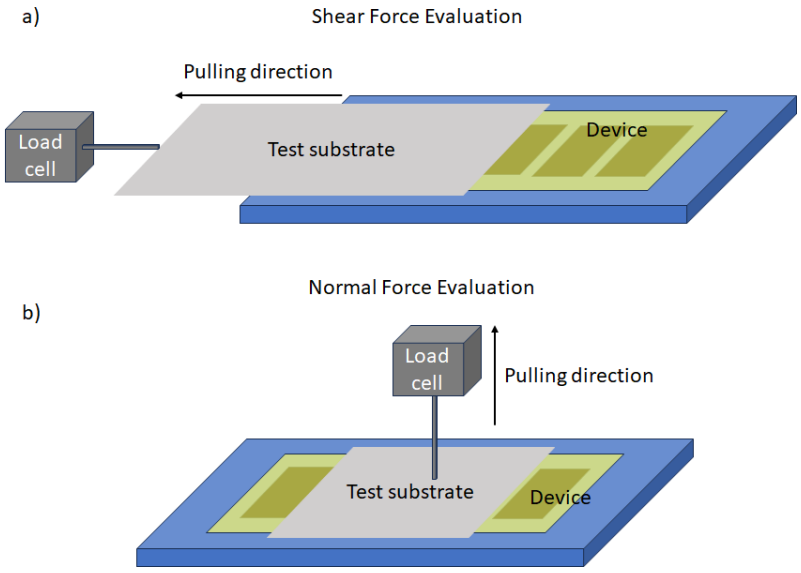

Figure 3 a) Electrostatic Shear Stress evaluation on shear force experiment. b) Normal force evaluation

Typically, the system is powered with high voltage, in the order of kilovolts. In this configuration, the electro-adhesive force $\overline{F}_{AD}$ takes on the characteristics of a frictional force that adds to the mechanical frictional force between the two objects.

$$\overline{F}_{SS} = (\overline{F}_{AD} + \overline{F}_N)\,\mu \quad (34)$$

Where μ is the static friction coefficient, $\overline{F}_N$ is the normal force due to the weight.

$$ESS = \frac{\overline{F}_{SS}}{Area_{EA}} \quad (35)$$

This is why a test without powering the device is conducted to eliminate the mechanical frictional force and assess only the component due to electroadhesion.

The second configuration, on the other hand, involves evaluating the electroadhesive force normal to the surface of the object it adheres to. The underlying logic for the setup to measure the normal electroadhesive force is similar to that used for assessing the shear force. In this case, the direction in which to pull the substrate or device relative to each other, and thus the direction of the force measured by the load cell, is perpendicular to the surface. This eliminates the component of mechanical friction from the measurement[24].

The breakdown of the device involves the rupture of one of the dielectric materials comprising it, which means an instantaneous release of the energy accumulated in the capacitive system through a current discharge within the material[25]. This leads to the breaking of polymer chains or the crystal lattice, transforming the material from a dielectric to a resistive state. For example, the phenomenon is analogous to lightning, which occurs due to the difference in potential between statically charged clouds and the ground, though in this case, it occurs in the air. In our case, it happens within a dielectric material (Figure 4c).

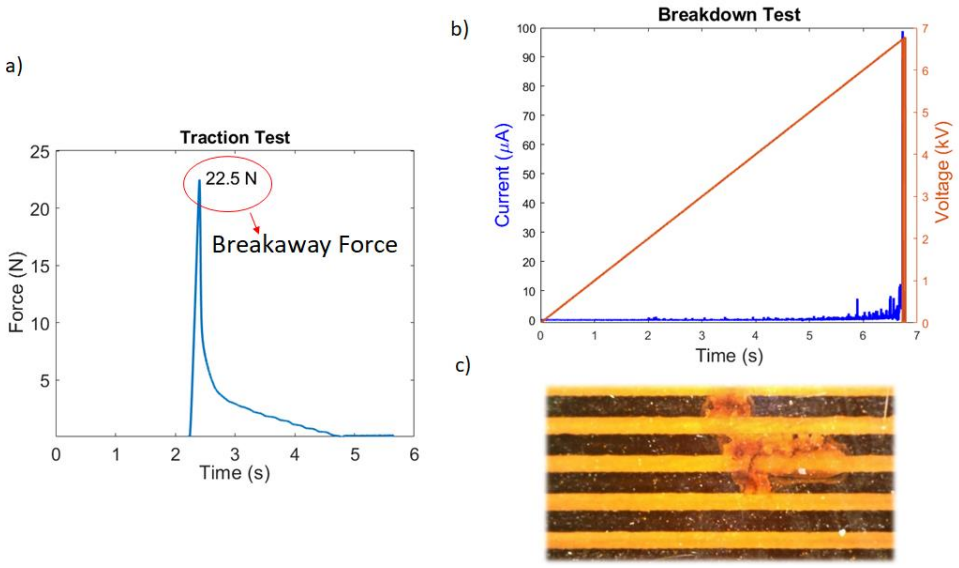

Figure 4 a) Load signal vs time, the maximum give the EA force value . b) Breakdown experiment, voltage and current monitor. c) Breakdown optical image

One of the fundamental properties of a dielectric material, typically listed in its datasheet if it is industrially produced, is called Dielectric Strength[26]. This represents the maximum electric field value (and therefore potential, considering the geometric and stoichiometric components of the system) that the material can withstand before a breakdown event occurs. Therefore, to characterize devices using electroadhesion, it is essential to evaluate the dielectric strength of the system, composed of layers of dielectric materials. In particular, phenomena and impurities at the interface between various materials will affect this value, making it dependent not only on the types of materials used but also on the precision and the type of manufacturing process utilized. To determine the maximum applicable voltage for the device, a standard procedure is followed. This procedure typically involves applying a slow-rising voltage ramp, for example, at a rate of 1 kV/s [27], while monitoring both the current and voltage. When the current monitor detects a constant current flow, it indicates that a breakdown event has occurred, and the system has transitioned from a capacitive to a resistive state. The voltage value at that moment is considered the breakdown voltage or dielectric strength.

2.3 Electro Adhesive Devices (EAD)

A device that physically embodies a capacitive system, utilizing Coulombic forces to adhere to a surface, is referred to as an electro adhesive device (EAD)[6][28]. While the physical description of such systems is not straightforward, and indeed only imprecise models have been developed and presented in the literature[8], [29], [30], the basic architecture of an EAD is quite simple. It consists of a pair of electrodes deposited on a substrate, typically dielectric, and immersed in a dielectric matrix, often elastomeric, to insulate them. The electrodes are separated by a certain distance and, when powered, they create the plates of a capacitor, polarizing the dielectrics and charging the entire system. Numerous examples can be found in the literature regarding manufacturing techniques used to produce these devices. Many of these are described in Chapter 3. , and below are provided some examples of the application of these techniques used in notable cases. Production methods can be categorized into three main categories: additive, subtractive, and additive-subtractive[11]. The additive method, named also bottom-top process, involves the deposition of conductive or dielectric layers one after another. The method used in this thesis work to construct EADs, described in detail in Chapter 7. entails the placement of a dielectric substrate, or the use of one commercially available, followed by

the deposition of conductive material for the production of electrodes, and finally, electrical insulation through the deposition of additional dielectric material.

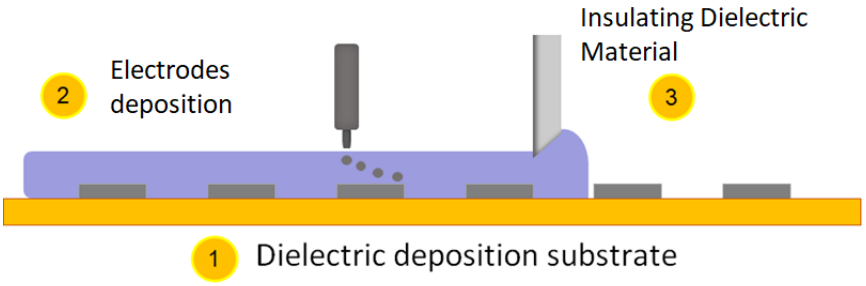

Figure 5 Bottom up process building an EAD: Electrodes are deposited on plastic substrate and then insulating material is deposited

This method involves the use of techniques such as inkjet printing, screen printing, blade casting, or spin-coating. The subtractive method, also known as the top-bottom process, on the other hand, involves thee removal of material from a bulk source, shaping it into the desired form and size. This process includes a first step of removing conductive or electric material and a second step of bonding or laminating the various layers. This method utilizes laser cutters or milling, as well as chemical etching for the removal of unwanted material, surface plasma treatment, and lamination for bonding processes. The drawback of these methodologies lies in the limited repeatability and accuracy of the process, but it allows for the creation of samples at a reduced cost. An additive-subtractive process, as the name suggests, combines both processes by first eliminating unwanted material and then using additive manufacturing techniques to deposit material, such as insulating dielectric. The most common example is chemical etching followed by insulation in the manufacture of circuit boards.

2.3.1 Electrodes deposition

In the construction of an EAD, as well as its performance (see 2.2), a significant emphasis lies in the choice of materials and electrode deposition techniques. In particular, extensive studies have been conducted on dielectric elastomer transducers and actuators (DET and DEA), devices that leverage the polarization of a capacitive system for use as sensors or actuators. These systems typically undergo substantial deformations, necessitating electrodes capable of accommodating such deformations. Generally, for EADs, a fundamental requirement for proper functionality is the maintenance of electrical conductivity even during flexion. This is how various techniques have been studied for electrode deposition on the dielectric substrates used

in EADs based on the specific application requirements[14]. For the production of deformable electrodes, screen printing and blade casting technologies have yielded excellent results, effectively working with highly viscous solutions[31]. In the realm of flexible electronics and, generally, for printing flexible yet non-deformable electrodes, inkjet printing and chemical vapor deposition have gained more popularity as they avoid direct contact with the surface[32]. An exception is made for some outstanding work in which an ink containing carbon black suspended in PDMS was printed using Drop-on-Demand (DoD) inkjet printing. The capability of digitally precise deposition of this mixture has enabled the construction of MEMS with stretchable electrodes. Another key aspect regarding the electrodes and their impact on the overall functionality of the EAD is the geometry in which they are deposited[30]. This directly affects the intensity and spatial distribution within the dielectric materials of the electric field produced by the electrode system. Various shapes and configurations have been studied to achieve the best device performance (for a discussion on the performance of an electro-adhesive device, refer to 2.2 . Two configurations have been identified as superior in terms of performance. The uni-layer configuration (Figure 6b), which is easier to manufacture, involves electrodes on a single plane, interposed with each other, immersed in dielectric layers [17].

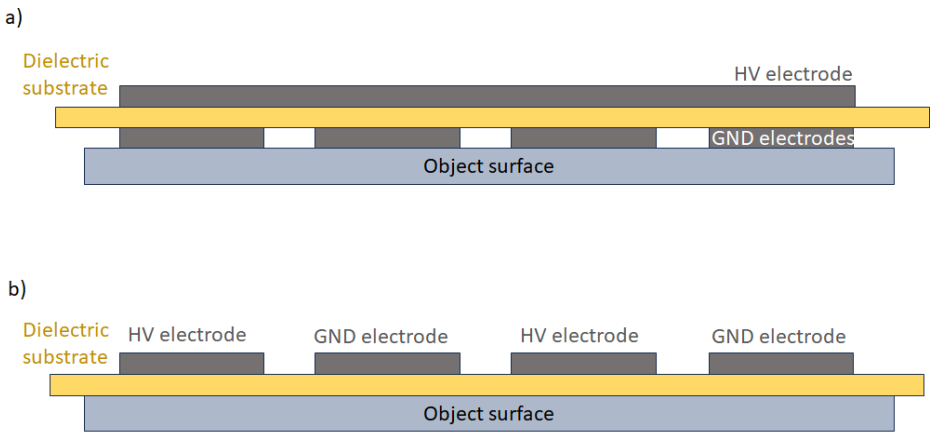

Figure 6 EAD a) bi-layer configuration and b) uni-layer configuration

As discussed earlier in this chapter, this configuration produces a periodic electric field in space. The bi-layer configuration (Figure 6a) entails positive and negative electrodes deposited on two sides of a substrate, which is positioned between them. One electrode is deposited as a single layer of conductive material and powered positive or negative, while the other electrodes are deposited with a periodic structure. Although the bi-layer configuration has exhibited higher electro-adhesive force for some applications (Figure 7), due to ease of production and the relatively close performance to the uni-layer configuration, it has been considered preferable in

this thesis work and used in the production of EADs. For further details on the bi-layer configuration, as it is not the subject of this thesis, reference is made to [33].

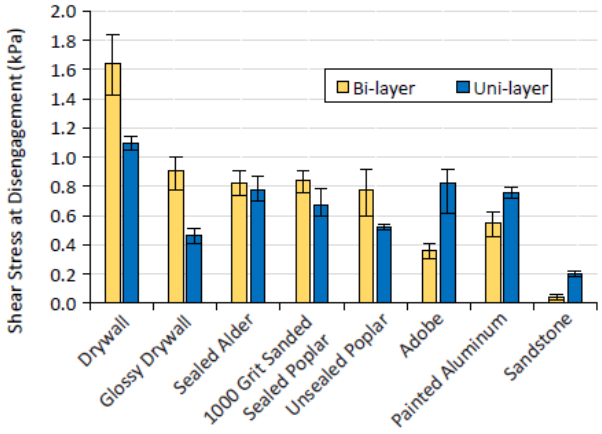

Figure 7 Uni and Bi-layer configurations comparison on ESS performances on different objects

Many electrode configurations have been proposed for the uni-layer configuration. In the literature, examples of concentric, spiral, comb-shaped, and Hilbert curve-shaped electrodes can be found Figure 8a. Each of these examples involves two electrodes interposed, separated by a very fine gap. By supplying the electrodes with a voltage generator, the charges carried on the electrodes and the gap that separates them create the capacitive system and distribute the electric field in the dielectrics that form the device. In general, the solution with concentric circle-shaped electrodes has proven to be the most effective in terms of electroadhesive force (Figure 8b) , but it is not significantly different from the comb-shaped geometry. This is why the latter, also known as the interdigitated geometry, has become a reference in the field of electroadhesion and is the most widely used worldwide. It is, in fact, the one used in this thesis work as the basis for constructing the electrodes that make up the EADs described below.

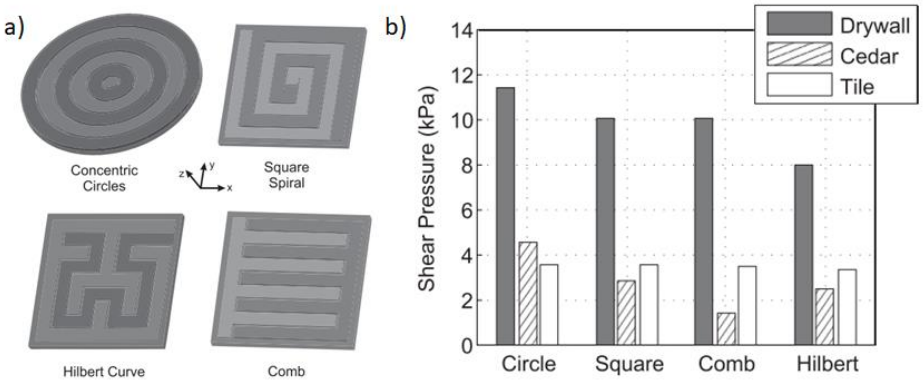

Figure 8 a) Different geometries of EAD electrodes. b) Comparison of shear pressure of different geometries

Chapter 3. Additive manufacturing technologies

3.1 3D Manufacturing technologies overview

Additive manufacturing (AM) defines a layer-by-layer manufacturing processes that have been recognized as effective methods for achieving 3D bulk structures[10], [34]. Over the last decade, AM technologies have seen extensive development in their use for producing intricate 3D components, involving essential modifications and enhancements to create suitable conditions for microfabrication. Scalable AM technologies, such as stereolithography, selective laser sintering, 3D printing (3DP), inkjet printing processes, screen printing, spray sputtering, fused deposition modeling, laminated object manufacturing, spin-coating, and blade casting, constitute the first group of technologies that show promise for achieving genuine 3D micromanufacturing. Direct write (DW) technologies were initially developed primarily for two-dimensional (2D) writing purposes. However, some DW methods, such as laser chemical vapor deposition, focused ion beam, aerosol jet processing, laser-induced forward transfer, matrix-assisted pulsed-laser direct write, and nozzle dispensing processes (including precision pump and syringe-based deposition methods), also can be applied to produce high-resolution 3D microstructures and components. Nozzle dispensing techniques are currently employed to manufacture 3D micro-periodic structures for various applications. While the aerosol jet process is less commonly used for microfabrication of microstructures, it holds significant potential for 3D applications.

In this chapter, we will briefly discuss these primary advanced additive manufacturing techniques, emphasizing inkjet printing over other deposition methods, highlighting its advantages and respective applications.

3.1.1 Stereolithography

This process is based on layer-by-layer photosensitive resin polymerization using ultraviolet (UV) light, used in various areas such as micromachines and microsensors, microfluidic style. For the formation of each printed layer, three steps must be conducted sequentially: the first step is to expose resin to UV light, secondly the cured part needs to be mechanically moved either to separate from the surface of resin vat (for bottom-up systems) or to lower into the resin (for top-down systems) for resin renewal, and the third part is re-positioning. Three main techniques can be distinguished:

- *Laser Scanning Stereolithography*: the photopolymer is solified line-by-line with a laser spot of 13 μm focused by a dynamic lenses system. A fixed UV light beam focuses on the resin surface and solidifies the curable resin to produce objects above the printing platform. In addition, another important laser scanning process, two-photon polymerization, is considered as a unique photopolymerization process. It differs from conventional (single-photon) stereolithography by focusing femtosecond laser pulses to a very narrow spot in which the resin is polymerized via absorbing two photons simultaneously. Therefore, two photon polymerization has advantages in fabricating micro/nano-scale structures.
- *Projection* S*tereolithography*: a whole layer of the photopolymer is cured once via exposure through provided masks, and makes it possible to cure each layer simultaneously with a single exposure. Quite different mask technologies have been developed to better and faster perform the manufacturing process, that in origin was dirty and slow. A liquid crystal display system can be used as dynamic mask, in which each cell can change its transparency with changing the orientation of the molecules it contains, but this technology is limited as it has a very low transmission in UV and poor contrast. A great innovation has been brought by Texas Instrument inc. developing the digital micromirror device, an array of up to several millions of mirrors that can be controlled independently to generate mask patterns.
- *Continuous Stereolithography*: is devised to print objects without stops from layer to layer, and is achieved by creating a persistent liquid interface (dead zone) with an oxygen-permeable window below the UV image projection plane. The oxygen-containing dead zone is able to inhibit the photopolymerization between the window and the polymerizing part, which allows the part to be continuously exposed while elevating. Thus, the latter two steps that existed in traditional stereolithography can be

eliminated. By using this technique, the parts can be drawn out of the resin continuously at rates of hundreds of millimeters per hour.

- *Volumetrical Stereolithography*: it produces 3D objects with the formation of 3D volumes as a unit operation. The superposition of patterned optical fields from three orthogonal beams were projected into a photosensitive resin. By the compensation between each beam, volumetric 3D geometries can be formed in a single exposure from the superimposed profile. By employing two perpendicular irradiation patterns at blue and near-UV wavelengths to independently effect either polymerization initiation or inhibition, the system allows the fabrication of objects by volumetric photopolymerization patterning in bulk resin. In the foreseeable future, volumetric stereolithography is expected to be further developed in many aspects, such as resolution, process and physical system, and combined with various fields.

3.1.2 Sheet Lamination

It's an additive manufacturing process in which sheets of material are bonded to form an object. The sheet lamination process is based fundamentally on the several steps. A thin-layered materials such as aluminum foil or sheets of paper are coated with adhesive and successively glued together layer by layer. A mechanical cutter or laser is used to precisely cut the successive layers before bonding them together (which can be form-then-bond or bond-then-form). Then, the form-then-bond method allows the removal of excess material prior to bonding, which facilitates effective thermal bonding of ceramic and metallic materials and the fabrication of internal features. Excess materials leftover after cutting can be used as support and subsequently removed or recycled. The ease of material handling results in a reduction of tooling cost and manufacturing time for the sheet lamination process, which is also suitable for manufacturing large structures. Moreover, objects created via sheet lamination do not require support structures, as the unused build material that surrounds them holds everything in place and can be used for a variety of materials such as polymer composites, ceramics, paper, and metal-filled tapes. Postprocessing such as high-temperature treatment may be required depending on the type of materials and desired properties. Lamination can result in a reduction of tooling cost and manufacturing time and is one of the best additive manufacturing methods for larger structures. However, it has low surface quality (without postprocessing) and its dimensional accuracy is inferior to powder-bed methods. Also, removing the excess parts of laminates after

formation of the object is time-consuming compared to the powder-bed methods. Therefore, it is not recommended for complex shapes.

3.1.3 Coatings methods

Spin-Coating

It is a process of applying a solution to a horizontal rotating disc, resulting in ejection and evaporation of the solvent and leaving a liquid or solid film. Spin-coating is a unique technique in the sense that it is possible to apply a highly uniform film to a planar substrate over a large area (Ø ¢ 30 cm) with a highly controllable and reproducible film thickness. Spin-coating has been a highly effective technique for the production of thin films in various fields, including microelectronic, microfabrication, photovoltaics, and material science, and it has been widely used in various applications such as coating of photoresist on silicon wafers, sensors, protective coatings, paint coatings, optical coatings and membranes. It offers numerous advantages, including reproducibility, homogeneity, and control over film thickness, morphology, and surface topography. This technique has played a significant role in the field, particularly for experimental purposes during materials screening and device optimization. However, there are certain limitations to consider as it is not directly compatible with roll-to-roll (R2R) high-volume production, and it lacks the capability to pattern formed films. The process involves a rotating disc rapidly accelerated after the solution is deposited. The adhesive forces at the liquid/substrate interface and the centrifugal forces acting on the rotating liquid result in strong sheering of the liquid which causes a radial flow in which most of the polymer solution is rapidly ejected from the disc, as depicted in Figure 9.

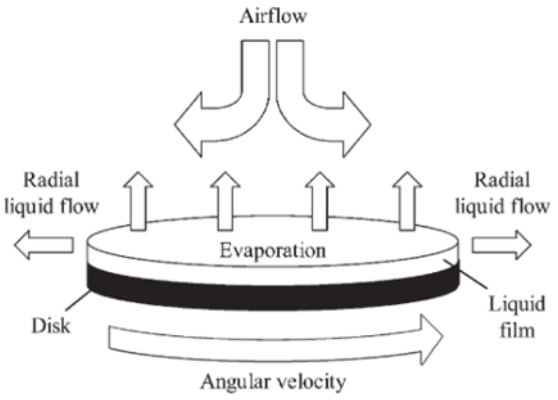

Figure 9 Schematic of spin coating process

This process combined with subsequent evaporation of the liquid causes the thickness of the remaining liquid film to decrease. For a polymer solution, the evaporation process causes the polymer concentration to increase (and thus the viscosity) at the liquid/vapor interface, and so a concentration gradient is formed through the liquid film, which, after evaporation of most of the remaining solvent, consequently results in the formation of a uniform practically solid polymer film.

Blade Casting

Named also doctor blading, allows for the formation of films with a well-defined thickness. In contrast to spin-coating the technique is quite parsimonious and with some practice the loss of coating solution can be minimized such that less than 5% is lost. The technique works by placing a sharp blade at a fixed distance from the substrate surface that is to be coated (typically 10–500mm). The coating solution is then placed in front of the blade that is then moved linearly across the substrate leaving a thin wet film after the blade. The final wet thickness of the film is ideally half the gap width but may vary due to the surface energy of the substrate, the surface tension of the coating solution and the viscosity of the coating solution. Compared to spin-coating, where the wet film formation is fast, doctor blading is relatively slow and if the dissolved material has a propensity to aggregate or crystallize at high concentration this often happens during doctor blading. The inks/pastes used in these processes usually require large amounts of binders and thickeners to produce the high viscosities (1000–10000 mPa s) required for reproducible and reliable production of films. Viscosities can be increased with the addition of polymeric additives such as glycerol or ethylene glycol or ethyl cellulose.

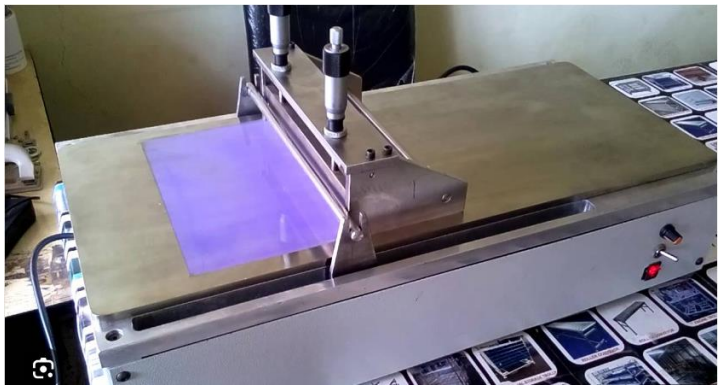

Figure 10 Doctor Blade Coating technique for thin film deposition

3.1.4 Printing methods

Screen printing

Screen printing, an ancient art that has been widely used in garment manufacturing, is based on the direct contact transfer of ink from a stenciled mesh to a substrate. In the past, the scientific principles governing this process were not well understood. However, recent research has shed light on the underlying mechanisms. It is a very versatile printing technique that allows for full 2-dimensional patterning of the printed layer. It is parsimonious and there is essentially no loss of coating solution during printing. Its main distinction from all other printing and coating techniques is a large wet film thickness and a requirement for a relatively high viscosity and a low volatility of the coating solution. The pattern is obtained by filling the screen with an emulsion that is impervious to the coating solution in the areas where no print should appear. The area of the printed pattern is kept open (without emulsion). The screen is then filled with coating solution and brought into proximity of the substrate.

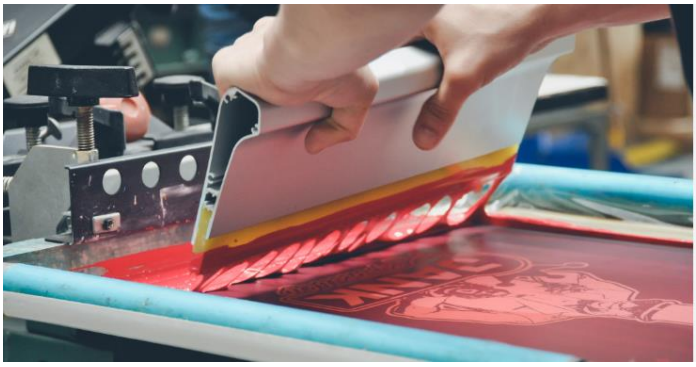

Figure 11 Screen Printing manual technique

This process is influenced by various parameters, such as ink viscosity, cohesive and adhesive forces, pseudoplasticity, and mesh angle relative to the substrate. The viscosity of the ink, adhesion to the substrate, and cohesive forces primarily determine the deposition height and print resolution. Larger filaments produce thicker circular depositions and affect print quality, reducing resolution. The interaction between manufacturing parameters and ink properties significantly impacts print quality. Ink printability is determined by several rheological parameters. Ideally, screen-printing inks are pseudoplastic, meaning they reduce viscosity with shear, allowing ink to flow during extension and recover during separation. Other rheological characteristics, such as viscoelasticity and thixotropicity, should be minimized to avoid prolonging filament formation and delays in viscosity recovery. Viscosity, yield stress, and surface tension are interrelated but have contrasting effects on printability. Achieving an optimal balance between these factors is essential for high-quality screen printing. Overall, understanding these principles is crucial for optimizing screen printing processes and developing printable inks with high conductivity, strain resistance, and fine resolution. Recent

research has focused on improving ink properties to achieve high-resolution prints, making screen printing a promising technique for various applications.

Spray coating

Spray coating is a technique that involves propelling printing ink through a nozzle to create a fine aerosol. This process may include the use of a carrier gas and electrostatic charging to help direct the aerosol onto the target surface. While spray coating is theoretically compatible with patterning of coated films at a millimeter scale, but achieving a smooth surface can be challenging. The complexity lies in the formation of the aerosol and the evaporation of some of the solvent. Aerosol droplets must level themselves on the substrate, which is not always guaranteed. The ease of ink preparation can vary from simple to complex, and a wide range of viscosities can be employed. There isn't a straightforward relationship describing wet film thickness, as both thin and thick films can be prepared using this method. To date, there have been relatively few instances of spray coating being utilized in organic photovoltaics.

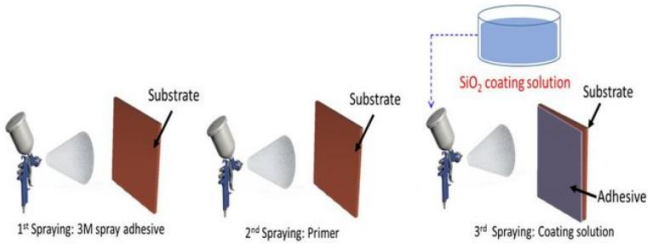

Figure 12 Spray coating technique scheme

Inkjet printing

In recent years, inkjet printing has gained significant popularity due to its remarkable versatility in creating precisely digitized 2D and 3D structures without the need for masks and without direct contact with the printing substrate. This characteristic prevents potential surface damage and malfunctions in the final device. It has been demonstrated that inkjet printing is capable of producing 3D microstructures, both polymeric and metallic, such as silver or gold micropillars, with applications in micro-mechanical systems. A key strength of this technology lies in its ability to print a wide variety of materials, including polymers, organic materials, biologically active fluids, organic transistors, OLEDs (Organic Light-Emitting Diodes),

thermoplastics, ceramic materials, and piezoelectric substances. Inkjet printing is particularly valuable during the prototyping phase of a device but is often not suitable for large-scale production. It is also a valuable tool for confirming physical principles and models. Greater emphasis should be directed toward the advancement of inkjet printing systems capable of producing high-quality, true 3D microcomponents from functional materials, including metals, ceramics, and smart materials. This development is crucial to attain the desired thermal, mechanical, and electrical properties for the MEMS/MOEMS (Micro-Electro-Mechanical Systems/Micro-Opto-Electro-Mechanical Systems) industry. The integration of inkjet printing processes with printed electronics technology enables the manufacturing of genuine MEMS components. In the coming years, we anticipate an expansion in both the quantity and diversity of products created using inkjet technology. Moreover, the availability and capabilities of inkjet-based prototyping and production tools are expected to increase. Commercialization efforts are currently underway for various products using inkjet-based methods, such as DNA microarrays, color displays, electronics assembly, and photonic elements. It is within this context that inkjet printing demonstrates its distinct versatility, finding utility in various applications. The array of printable materials, the ability to create custom shapes, and the unique attribute of being a contactless technology, preserving the properties of the substrate, make inkjet technology a more advantageous choice in research and prototyping. By obviating the need for masks and dispensing controlled ink quantities, the process becomes expedited and waste-free. However, it is worth noting that this technology is not suitable for mass production or adaptable to roll-to-roll processes

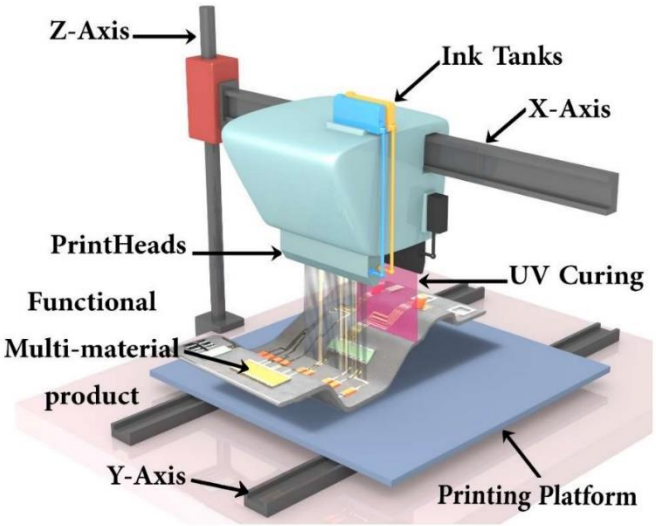

Figure 13 Inkjet Printer example

Chapter 4. Inkjet printing technology

4.1 Introduction

Inkjet printing has represented a significant innovation in both everyday life and experimental research. From the deposition of ink on common paper in the daily use of household printers to the precise dispensing of minute quantities of material in advanced additive manufacturing research, this technology has demonstrated remarkable versatility and innovative potential over the past decades[35]. In the field of research, this technology has led to substantial advancements in flexible electronics printing, with the possibility to use conductive and dielectric materials, as well as the deposition of organic substances and polymers[36], [37]. It is within this context that it greatly innovated the field of micro-robotics, often referred to as MEMS (Micro-Electro-Mechanical Systems)[38], and in the domain of soft robotics.

In all inkjet printing technologies, the solution to be printed is placed in cartridges, or small tanks, connected to a nozzle with an orifice diameter below hundreds of microns. The liquid flowing through the orifice is then deposited onto a specific substrate forming continuous lines. The method of liquid emission from the orifice determines the type of technology. In Continuous Inkjet printing technology, as the name suggests, the fluid, or ink, is continuously emitted, as stream of droplets, from the nozzle, depositing continuous lines on the substrate. In Drop on Demand (DoD) inkjet printing technique, ink is emitted in consecutive different drops from the orifice. This allows for precise digital deposition, drop after drop. The main rheological properties of the liquid used as ink are crucial for achieving a stable jet or drops to deposit a straight line on the substrate. In particular, surface tension and viscosity determine the ink's ability to be ejected smoothly from the nozzle without causing any disturbances that might lead to instability [ref]. Additionally, these properties create the optimal conditions for ensuring stable droplets during their flight to the substrate, whether in continuous or DoD mode. Surface tension, defined as the free energy of the molecules on the surface, in combination with the substrate's wettability, influences whether the drop will be absorbed by the substrate, thus

defining the ink's printability. Two dimensionless numbers have been established to quickly assess the printability of the ink, based on these two rheological factors[39]. The Reynolds number R_e, represents the ratio between inertial and viscous forces in a moving fluid, and its defined as:

$$R_e = \frac{\rho d V}{\eta} \quad (36)$$

where ρ is the density of the fluid, V is the stream velocity, η is its viscosity and d is the characteristic length. In this case d can be related to the diameter of the orifice of the nozzle. The *Weber number* W_e depends on the ration between inertia and surface tension:

$$W_e = \frac{\rho d V^2}{\sigma} \quad (37)$$

where σ is the surface tension. Combining them, the *Ohnesorge number* Oh is defined as

$$Oh = \frac{\sqrt{W_e}}{R_e} = \frac{\eta}{\sqrt{\sigma \rho d}} \quad (38)$$

If *Oh* is high (>1) the viscous forces prevail and prevent the droplets formation where, if it's too low, the jet will dissipate in several uncontrolled drops, usually called satellites Figure 14.

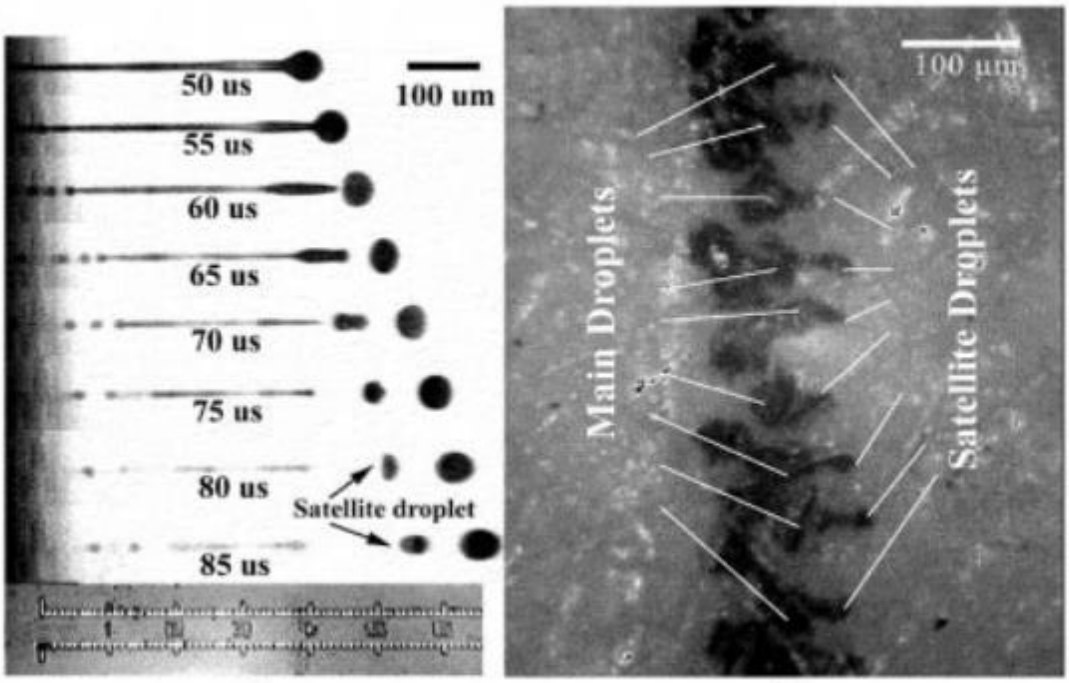

Figure 14 Drop ejection from the nozzle with undesired satellites that provoke non-uniform line borders

To fast understand the 'printability' of a fluid, the inverse of the Raynolds number, named Z, is used. When $4 < Z < 14$, the liquid shows the perfect combination of rheological properties to be printed.

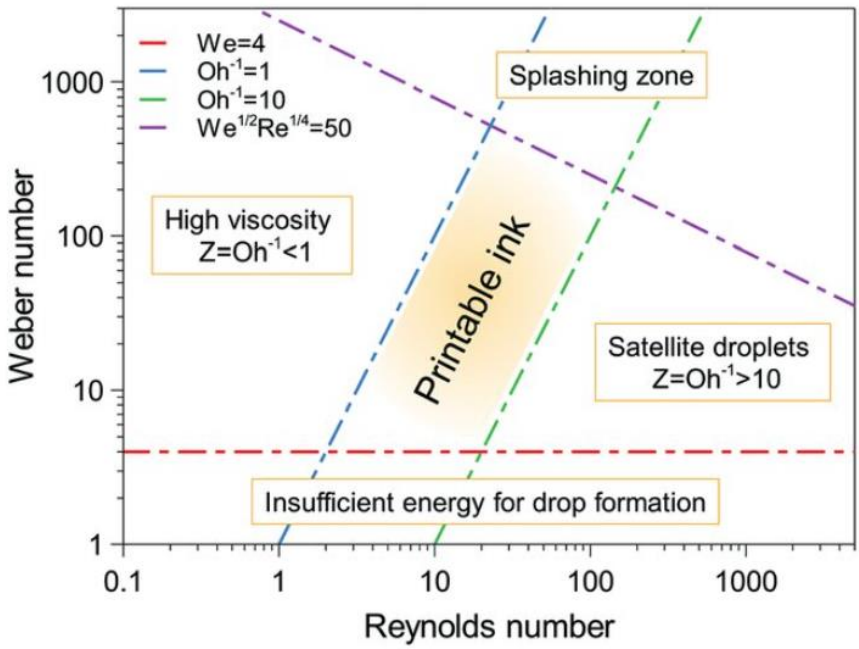

Figure 15 Pictorial view of the region in which the rheological properties of a solution are optimal for DoD inkjet printing[40]

Reproduced from J. Eur. Ceram. Soc., vol. 31, B. Derby, Inkjet printing ceramics: from drops to solid, pp. 2543-2550, Copyright (2011), with permission from Elsevier. 63

4.2 Droplets deposition

An important stage in the generation of the image or pattern involves the impact of the liquid drop on a substrate and the subsequent phase change that converts the liquid into a solid. This liquid-to-solid phase change can occur through various mechanisms, including solvent evaporation, cooling through a transition temperature, thermal curing and chemical reaction. In all these cases, solidification takes place after deposition, and the printed pattern must maintain some stability in the liquid state before solidifying. To comprehensively understand the processes that take place between the printed drop and the substrate before achieving the final structure, it's essential to identify the interactions occurring between the substrate and the fluid drop prior to solidification, as a comprehensive understanding of the potential mechanisms involved in the process has not been fully achieved. When a liquid comes into contact with a solid surface, it tends to adopt an equilibrium shape, determined by the balance of three key

surface energies: the surface energy between the liquid and its surrounding environment, the surface energy between the solid and the surrounding environment, and the surface energy between the liquid and the solid. This equilibrium shape is characterized by the equilibrium contact angle and can be described by the Young equation [41]. The Young equation is applicable in the immediate vicinity of the contact line at equilibrium. However, gravitational forces may influence the droplet's shape at locations far from the contact line. In cases where gravitational forces are significant, the profile of the deposited liquid must be calculated by solving the Young-Laplace equation across the entire liquid surface, taking into account parameters like pressure, density difference, gravity, distance, and principal drop radii of curvature. For inkjet printing, individual droplets typically have Bond numbers much less than 1, rendering the need for this calculation unnecessary. It is assumed that the liquid will adopt truncated sphere geometries to minimize surface energy. The equilibrium wetting of a droplet on a substrate can also be influenced by the use of heterogeneous and structured substrates. These substrates introduce additional energy barriers that can lead to metastable energy states different from equilibrium. Additional vibrational energy may be applied to overcome these energy barriers, prompting the droplet to adopt the expected truncated sphere geometry. The surface energy balance at equilibrium is altered on rough surfaces due to increased contact area between the droplet and the substrate. By minimizing contact with roughness asperities while maintaining this form of wetting, it is possible to achieve a contact angle approaching 180 degrees. This behavior represents the wetting of a liquid on a chemically heterogeneous substrate where the variation in surface energy is significantly smaller than the size of the droplet. Using patterned surfaces with heterogeneities in either surface energy or topography of a similar magnitude to the droplet enables the controlled wetting of predefined substrate areas.

When two droplets come into contact, an instant inversion of the radius of curvature occurs at the point where the liquid bridge initiates. However, experiments with spherical droplets in contact reveal that the droplet's curvature flattens, resulting in a finite contact area. This flattening can be attributed to the compression of the volume between the approaching droplets, increasing pressure and adjusting the surface equilibrium accordingly. The flow within the liquid bridge depends on the properties of the droplet liquid, including density, surface tension, and viscosity. After coalescence, there's a driving force to minimize surface energy in compliance with the Young equation. Consequently, the droplet tends towards a spherical cap geometry, necessitating the advancement and retraction of the contact line on the substrate. The

retraction of the coalesced droplets is significantly influenced by environmental conditions, with orders of magnitude difference in timescales between ambient and saturated conditions.

The environment's saturation plays a crucial role in the relaxation time, mainly due to its impact on the evaporation rate. If a minor retraction of a deposited droplet can prevent overlap with a newly deposited one, this retraction leads to the formation of discontinuous regions of single or multiple droplets, breaking up a continuous bead. To create a two-dimensional pattern, a series of droplets must be deposited on a substrate. For this pattern to consist of continuous deposits larger than a single droplet, droplets must coalesce to form a liquid structure on the substrate. Understanding the process of droplet coalescence is essential for determining achievable structures through coalescence. This understanding guides the design of droplet deposition patterns and ink formulations. One of the simplest structures formed through droplet coalescence is a bead, created by the repeated coalescence of droplets in one direction across a substrate. When two droplets are deposited so that they overlap, they tend to coalesce, forming a single liquid body if the first droplet doesn't solidify before the next one is deposited. Consequently, a linear series of droplets on a substrate forms a liquid bead. To achieve a continuous bead, the droplets must be positioned closely enough to interact and coalesce.

4.3 Continuous Inkjet Printing

One of the earliest inkjet systems to be developed used a single continuous jet and employed electrostatic charging and deflection to select and control the placement of drops. Regular disturbances on the jet caused by the vibration of a piezoelectric structure, induce the jet to break up into a stream of drops. Drops not chosen for printing are collected in a catcher or gutter, and the liquid is returned to the supply system for reconditioning and reuse. To select drops for printing, an electrode is positioned near the point where drops form from the continuous jet. Applying a potential to this electrode induces an opposite electrical charge on the surface of the forming drop. For this to happen, the liquid must be sufficiently conductive. When the drop separates, the charge is retained on that specific drop, and the potential of the electrode can be adjusted to apply a different charge to the next drop (or set to zero for no charge). In this manner, each subsequent drop can be charged as needed. The selection process is completed by guiding the stream of drops through a fixed electric field, maintained between two additional electrodes, before they reach the catcher. Uncharged drops will continue in a straight path, while charged drops will be deflected by the field in proportion to the charge they carry. If the substrate surface moves perpendicularly to both the jet and the electric field, then

by selecting the timing and level of drop charging, successive drops can be deflected to create an image on the surface (Figure 16a). For text printing, this image would typically be one or a few characters high (in the direction of the deflecting field) and many characters long (in the direction of substrate movement) to form the desired text. Common applications for these types of inkjet systems include marking and date coding on foods and other products, as well as addressing and personalizing direct mail. Printing is feasible on substrates moving at high speeds (several meters per second), capable of keeping up with most production lines, but the print quality is best described as 'utilitarian'. Because the jet is continuously produced (preventing nozzle dry-out), and the ink system can be designed to make adjustments to the ink (e.g., by replacing solvent lost to evaporation), this method is capable of printing volatile liquids. Despite the rapid drop generation rate, the restricted printing width and the complexities associated with this method limit its suitability for use in digital fabrication[42], [43].

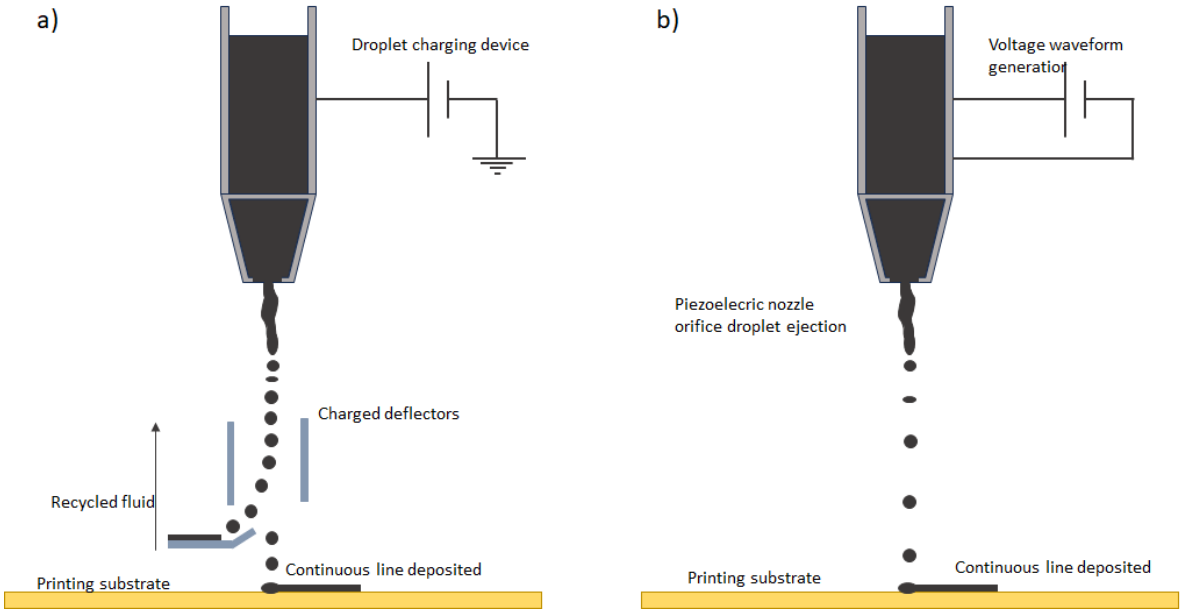

Figure 16 a) Continuous inkjet printing. b) Drop on Demand inkjet printing

4.4 Drop on Demand Inkjet Printing

In Drop on Demand (DoD) inkjet printing, ink is ejected from the nozzle tip in the form of consecutive droplets (Figure 16b)[44]–[46]. To create these droplets, the nozzle contains a piezoelectric actuator used to perturb the ink, which is stored in a reservoir within the nozzle

body.

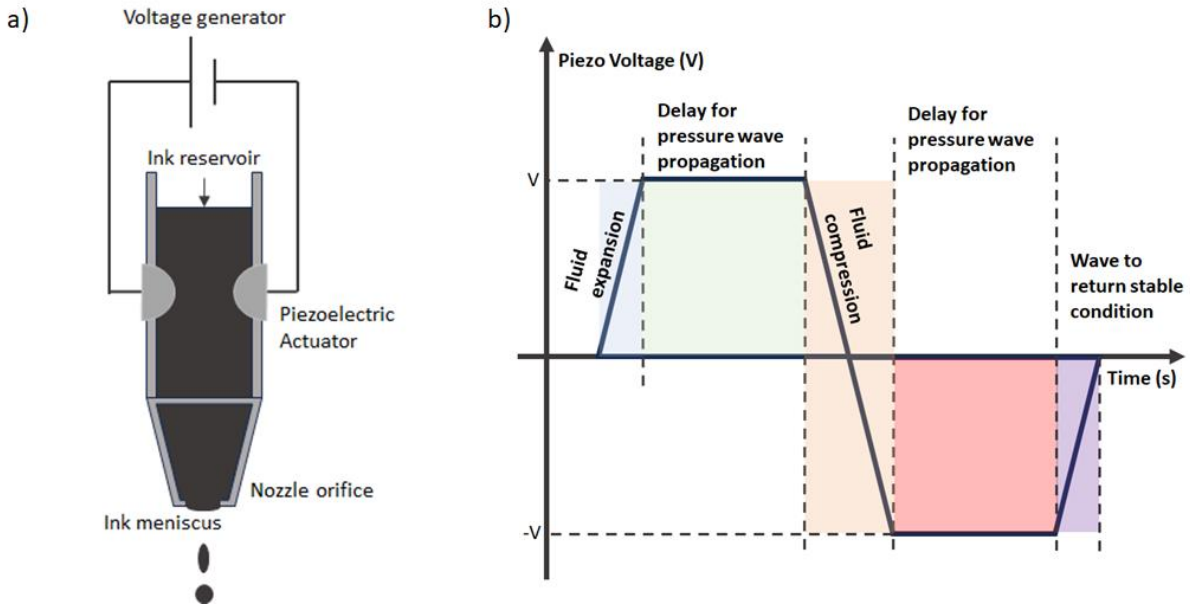

Figure 17 a) Piezoelectric Nozzle. b) Voltage waveform and its effect on the ink in the reservoir

An electrical signal is provided with a well-defined waveform, usually a trapezoidal bipolar wave, designed to match the physical properties of the ink (**Errore. L'origine riferimento non è stata trovata.**). The waveform signal moves the piezoelectric actuator, perturbing the ink pressure towards the nozzle orifice, causing the ink to be ejected. As the ink flows from the nozzle tip, an ink ligament is formed and, when the signal diminishes, it breaks, allowing surface tension to shape the resulting droplet into a spherical form. As this thesis in not focused on the numerical simulations, the complete discussion is deferred to the references [44], [45], [47]. With the exception of those utilized for experimental or research purposes, almost all Drop on Demand (DOD) print-heads incorporate multiple nozzles. Early commercial examples typically featured a few tens of nozzles, whereas modern print-heads consist of hundreds or even thousands of nozzles, often used in combination. Each nozzle contributes to one or a few lines (depending on the print configuration) of printed spots that collectively form the complete image. Unlike continuous jet systems, DOD print-heads lack drop selection or deflection systems, allowing the nozzles to be positioned in close proximity to the substrate surface. Since each nozzle only fires as needed, they remain inactive for a significant portion of the time. This inactivity can lead to changes in the ink at the open nozzle, such as evaporation, which can, over time, affect the performance of that nozzle when it is next activated. In the worst case scenario, the nozzle may fail to fire. Clearly, this is undesirable, and various strategies are employed to mitigate these effects. These strategies range from constraints in ink formulation

to mechanisms like spitting and purging into waste collectors during operation and capping when the system is shut down.

4.5 DoD inkjet printer description

This section provides an overview of the utilized inkjet printer, the Microfab Jetlab® 4xl. Figure 18 presents a general view of the machine and a schematic detailing its primary components.

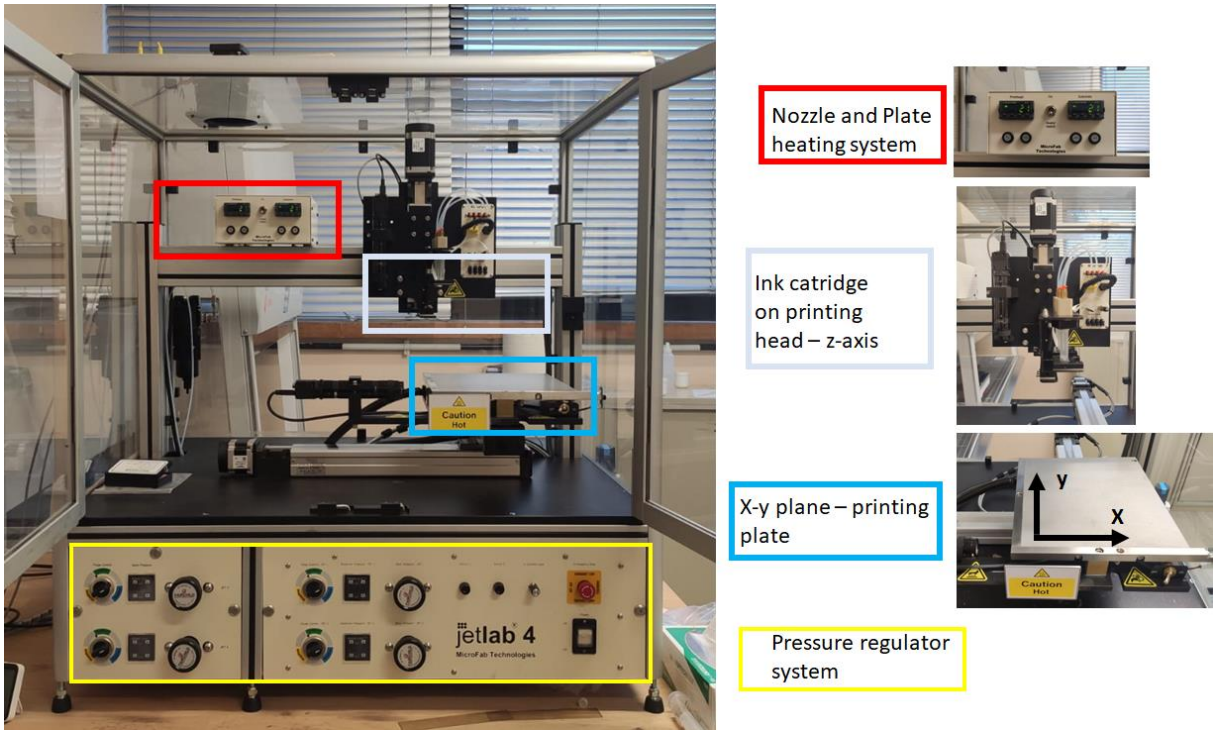

Figure 18 JetLab 4xl front view. Highlighted the pressure regulator system, x-y stage, or printing plate, the printing head with cartridges on it, and the heating system

The printing reference system is defined as follows: the x-y plane is determined by a motorized plate (PL-HV-4XL) of dimensions 210mm (along the x-direction) and 260mm (along the y-direction), which features a vacuum bed and a heating system capable of reaching temperatures of up to 120°C. The plate temperature control impacts the interaction between ink and substrate. For certain inks, and even for printable ones, elevating the plate temperature (typically ranging from 40°C to 60°C) accelerates solvent evaporation. This method enhances ink stability after deposition, preventing undesirable ink movement on the substrate. The z-axis corresponds to the vertical motion direction of the printhead (PH-46-SM4-AT-ST2-H) Figure 18. This printhead houses four printing channels and includes a jetting device heating system, which can reach temperatures up to 50°C. The printhead temperature control influences

the ink temperature, usually maintained at around 30°C, depending on the ink type, to reduce susceptibility to environmental conditions. Adjusting the nozzle temperature ensures consistent and repeatable printing sessions and, in some cases, can be utilized to modify ink viscosity, thereby aiding droplet formation. The three-axis motion can be simultaneous, enabling curvilinear printing, or restricted to the x-y axes, which is suitable for Print-on-the-Fly and Point-to-Point printing modes. In curvilinear printing, ink deposition can occur on convex surfaces or be employed for constructing 3-D microstructures. Print-on-the-Fly and Point-to-Point modes are used for planar printing. The Print-on-the-Fly mode accelerates the printing process as it involves simultaneous x-y motion with droplet ejection. In contrast, the Point-to-Point printing mode offers high precision droplet placement, albeit at the expense of a slower printing procedure. The Jetlab® 4xl placement accuracy falls within the following range: ±30 µm for positional accuracy and ±20 µm for positional repeatability. The printer is equipped with four printing channels, as depicted in

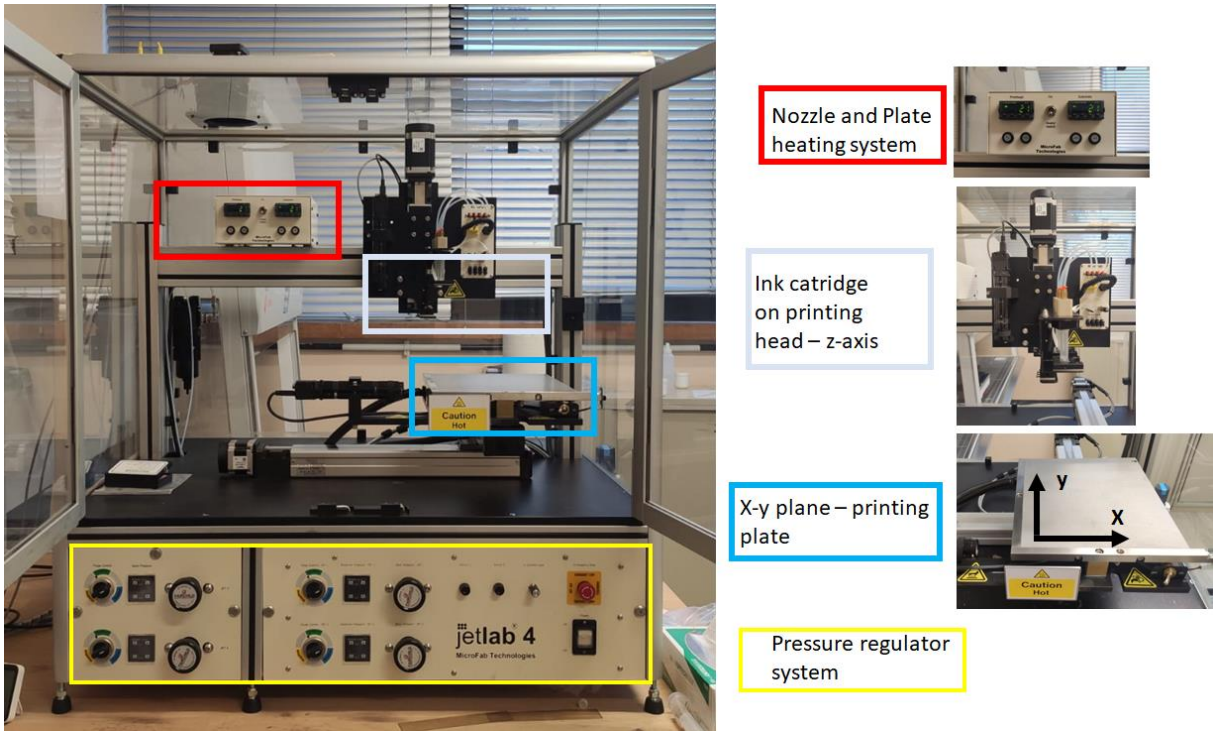

Figure 18, each with independently controlled pressure. Adjusting the pressure in the printing channel is crucial to compensate for gravity forces and achieve a flat meniscus, a prerequisite for proper droplet formation. The pressure controller for the jetting system is located on the bottom front panel of the machine, and Figure 19 illustrates the control panel for a single printing channel. By using the four-state knob, the printing channel can be switched between "Positive," "Negative," "Control," and “Idle” states, each serving specific purposes. In the "Positive" state (blue in Figure 19), the printing channel is subjected to maximum positive

pressure, primarily used for purging solvents from the nozzle during cleaning sessions. In the "Negative" state (yellow in Figure 19), the printing channel experiences maximum negative pressure, a valuable method for back-flushing solvents from the nozzle under specific circumstances. In the "Control" state (green in Figure 19), the channel's pressure is set by a manual pressure regulator and displayed on the control panel, as indicated in Figure 19. The “Control” state is employed during printing sessions. In the “Idle” state (grey in Figure 19), the backpressure controller is deactivated, allowing the fluid to remain at ambient pressure.

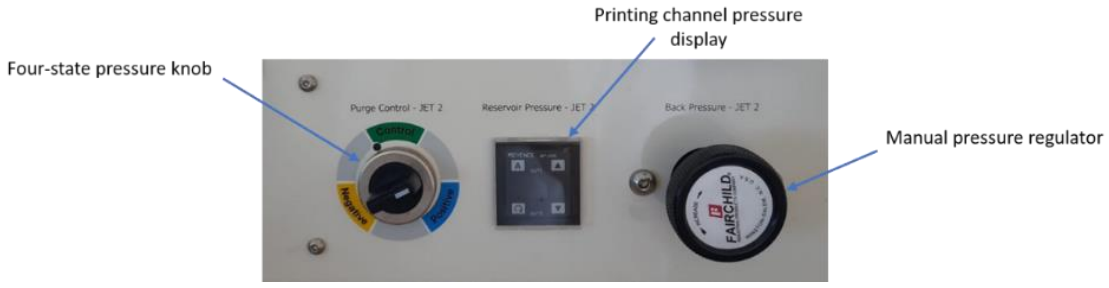

Figure 19 Pressure control, from the left: Stages of purge control, monitor indicating the pressure in mmHg, Manual pressure regulator to finely tune the pressure on the device.

The Jetlab® 4xl is equipped with two optical systems, one for drop observation and another for printing inspection, referred to as horizontal and vertical optics in Figure 20.

The drop observation camera plays a crucial role in verifying droplet formation when the nozzle jets at a specific position known as the Maintenance Position. In this state, ink is not deposited onto a substrate but instead collected in a waste sink. This step precedes printing and serves as a standard procedure for quality checking droplet formation. The stroboscopic light operates synchronously with the jetting frequency, capturing static drop images at regular intervals. A trackbar allows for the selection of a delay from time step zero, which corresponds to the moment when the voltage pulse is generated. This setup permits the observation of the entire droplet flight. Through this acquisition method, any instabilities in droplet formation are identified by non-static or vibrating droplet images, indicating that consecutive droplets possess different speeds and are located at varying positions after the same delay from voltage pulse generation.

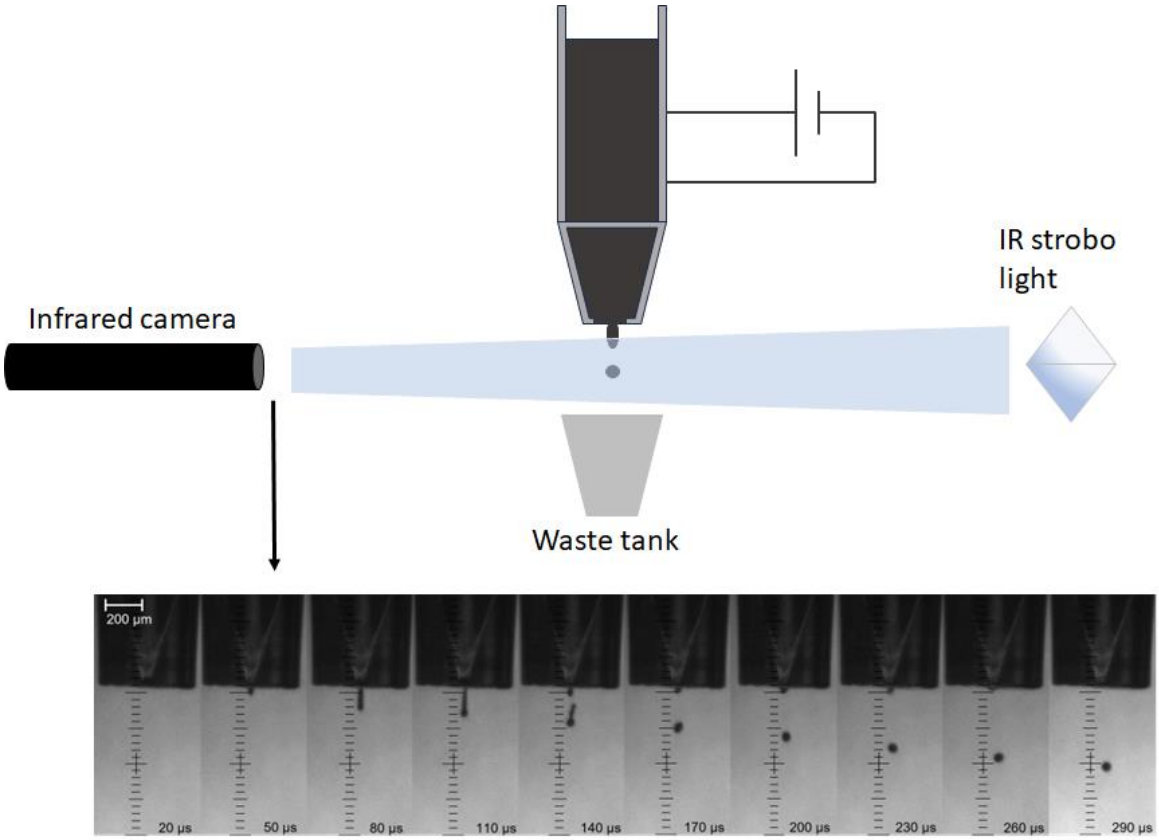

Figure 20 Drop view through IR camera system

Printing inspection facilitates the quality assessment of drop deposition and can be performed once the printing process has concluded. While it may be impossible to measure the contact angle of deposited ink using machine facilities, a top-view of the printed geometry remains a valuable method for quality assessment (Figure 21). Furthermore, this vertical optical system enables the determination of the printing starting point, consequently establishing the printing reference system on the printing plate. Figure 21 provides a detailed top-view of a conductive ink print on a polyimide film, acquired using the print inspection camera of Jetlab® 4xl.

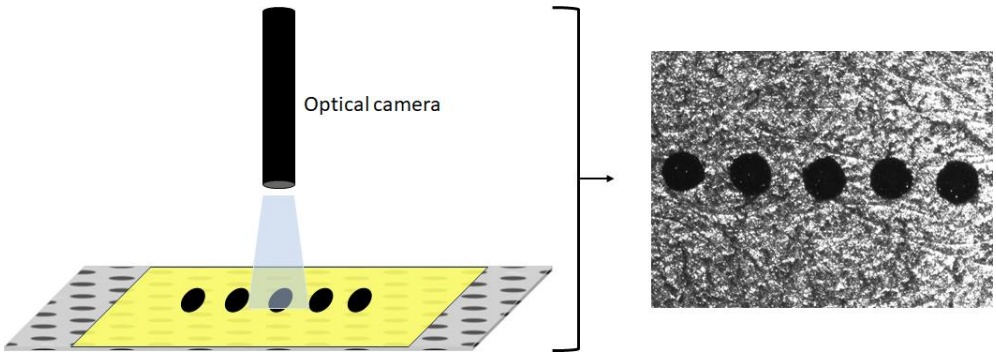

Figure 21 Camera for printing inspection viey, normal to the printing plate

Chapter 5. Inkjet printing of conductive materials: inks comparison

5.1 Introduction

One of the initial tasks undertaken in the doctoral research program focused on the inkjet printing technique of conductive materials[48]. This was done with the aim of creating precision-printed electrodes on thin film substrates with accuracies in the tens of microns. In literature and market, various types of conductive inks are presented, which include suspensions of nanoparticles, organometallic compounds in solution, and conductive polymers. Creating nanoparticle inks entails producing a suspension of nanoparticles in a liquid medium, be it water or an organic solvent like toluene, ethylene glycol, or cyclohexanone. The solvent choice needs to facilitate rapid evaporation upon application, while avoiding quick drying at the nozzle during short idle periods, preventing the formation of a viscous film that obstructs drop ejection. Nanoparticle inks find wide use due to the ability to produce nanoparticles in large quantities, disperse them at high concentrations, and achieve relatively robust electrical conductivities. As a general rule, the particle size should be less than 1/100th of the nozzle size, and particles should exhibit a narrow size distribution and uniform dispersion throughout the solution to ensure effective jetting. The substantial surface area-to-volume ratio of these particles allows sintering at lower temperatures compared to the bulk material. For instance, gold nanoparticles with diameters under 5nm are projected to undergo melting at temperatures between 300-500°C, significantly below the 1,063°C required for bulk gold to melt. Nevertheless, these inks are susceptible to the agglomeration of suspended particles, resulting in increased viscosity and the potential for clogging the nozzles of the print head. Taking advantages of their high electrical conductivity and air stability, these materials perform better than conducting organic polymers. The latter, including PEDOT, polypyrrole, and polyaniline, offer distinct advantages when employed in inkjet printing[49]. These polymers can be customized to exhibit sensitivity

to specific environmental or chemical factors, making them invaluable for sensing applications. Additionally, they find versatile applications in various fields where flexibility, stretchability and biological affinity are needed. Although nanoparticles have found extensive use in the production of silver and gold inks, their application is not limited solely to these materials. Silver and gold are favored for their exceptional chemical stability, low reactivity, and high electrical conductivity. Copper and nickel inks have also been manufactured, but their propensity to oxidize can impact the ink's longevity or necessitate the use of additional specialized coatings or printing in inert atmospheres. Promising innovative developments have been achieved in inkjet printing of electrodes capable of withstanding high levels of deformation, particularly in applications such as dielectric elastomer actuators (DEA) and within the wide topic of electro-active polymers. The need for electrodes that can follow the deformation of the structure on which they are printed, without losing their conductive properties during actuation, led to the creation of mixtures of silicone matrices with carbon-based materials properly integrated into the matrix. Among these materials, we find carbon powders, commonly referred to as Carbon Black Powder (CB)[31], or multiwalled carbon nanotubes (MWCNT)[50]. While these mixtures are easily deposited using macroscopic techniques such as blade casting or spin coating, inkjet printing necessitates careful consideration in terms of sintering. Given the small diameters of the nozzles, on the order of tens of microns, carbon particles and MWCNTs can easily form agglomerates, increasing the risk of nozzle clogging. Despite these challenges, notable examples of successful results have been presented, achieving deformations of up to 50%.

In the context of the research theme of this doctoral program, two conductive inks based on silver nanoparticles were chosen. Given that there was no specific requirement to accommodate significant deformations of the printed device and considering their high conductivity and ease of printing, commercially available inks formulated for inkjet printing technology were selected. The following two paragraphs describe the properties of these two inks and the results obtained in the printing process, as well as the procedure to evaluate the best printing parameters.

5.2 Materials and methods

To evaluate the printability of the inks described in the following section, we used the Jetlab 4x inkjet printer by Microfab, which is extensively detailed in 4.5 (please refer to that chapter for more details). It is essential to highlight some key details to follow the printing procedure.

The printer's reference system consists of an x-y plane established by the movement of the printing plate and a z-axis formed by the movement of the print head, perpendicular to the x-y plane. This reference system allows for defining the spacing of the deposited droplets in both printing directions, x and y, which is a fundamental parameter in the printing of lines and arrays. The printer also enables setting the nozzle and printing plate temperatures. These are set at 35°C and 50°C, respectively, to compensate for temperature variations in the machine's working environment, ensuring stable and consistent printing conditions over time. The nozzle height above the printing plate, and so the substrate, is set at 1.5 mm. The backpressure of the printing channel is set to -14 mmHg to ensure that the ink meniscus at the tip of the nozzle is flat, meaning the ink reaches the edge of the orifice. This configuration allows, once the piezoelectric actuator is activated, for a droplet to be ejected from the nozzle. A monopolar trapezoidal waveform is provided for both inks, and the parameters are listed in Table 1. The flight speed of the nozzle during printing is set to 30 mm/s.

Voltage Waveform	Anapro	Smart'ink		Rehology	Anapro	Smart'ink
Rise time (µs)	3	3		Desity (g/mm^3)	1.5	1
Pulse Duration (µs)	32	34		Surface Tension (dyn/cm)	36.5	29
Fall time (µs)	3	3		Dynamic Viscosity (cP)	13.5	13
Dwell Voltage (V)	36	40		Z number	3.88	2.93

Table 1 Differences in printing parameters and rheological properties of the two conductive ink

To begin a print, it's necessary to carry out some preliminary preparation work on the inks. Each ink undergoes an ultrasonic bath to eliminate any particle aggregates that could lead to printing failure and nozzle clogging. Subsequently, the ink is filtered using a 0.45µm PTFE filter inside a vial, which is used as a cartridge in the printer. The nozzle and all connecting tubes to the cartridge are washed with Isopropyl Alcohol (IPA), and once assembled on the printer, they are dried using oil-free, compressed air, filtered with 1µm filters.

The procedure established for testing the printability of an ink is described as follows:

- The printer is configured to form a stable droplet. This is achieved by setting the waveform parameters, adjusting the backpressure, setting the nozzle speed on flight, and controlling the nozzle and the printing plate temperature. The configured parameters are highlighted in Table 1, which includes the droplet shape acquired through the printer's camera system.

- A set of separate droplets is then printed to estimate the droplet diameter once deposited on the substrate. This is accomplished by visualizing the image captured with a camera oriented perpendicular to the printing plate. The machine's integrated software features a centering cross and the ability to move in 1 μm steps. These tools are used to calculate the droplet diameter, which is subsequently essential for constructing the printing arrays.
- Subsequently, a line is printed to set the correct spacing in the x-direction
- Then an array of droplets is printed as a filled rectangle. This procedure set the droplet spacing in the y-direction.

5.3 Results

1) *Smart'ink* from *Genes'ink* company

is a conductive Ag-based ink developed for the printed electronics market and is particularly well suited for applications requiring high conductivity and high resolution. It is perfectly adapted to design conductive traces on flexible substrates. Also, it is shaped for IoT application which required antennas (HF, UHF). In Table 1 the principal physical properties are listed and compared to the other ink I'll present in the next paragraph.

2) Anapro ink

has a high concentration of Ag particles with a uniform nano-size dispersed in a polar or non-polar solvent. It has excellent dispersion and maintains a viscosity suitable for the inkjet process. The ink printed via inkjet printing can be cured at low temperatures. It can be easily printed on various plastic materials, such as Polyimide, indium-tin oxide (ITO), PET etc. It takes advantage of its high jetting stability and excellent conductivity and adhesion to the substrate onto which is printed.

Through the procedure described above, optimal printing settings for the ink in question are obtained, such as droplet spacing in the x and y directions and nozzle speed during printing. The successful outcome of the printing is primarily determined visually. The edges of the array should be as straight as possible, without significant undulations. This is determined by the correct droplet spacing, as an excess of ink during deposition causes uncontrolled overflow. Conversely, excessive spacing does not allow coalescence of the drops to completely fill the shape. All the information concerning the waveform, printer parameters, and printing settings to achieve the best performance with this ink is listed in Table 1. Figures a, b, c, etc., depict the

printing results on a 25µm thick Polyimide (PI) substrate, commonly known as Kapton. Initially, several separate droplets were deposited, as shown in Figure 22. On average, the diameter of a droplet deposited on the substrate measured 182 µm for the *Smart'ink* and 220 µm for the *Anapro*. Those represents the minimum width of a deposited line, as it cannot go below the diameter of a single droplet, which serves as the basic unit for the printing process. Multiple lines were printed by adjusting the droplet spacing in the direction of the line, in this case, along the x-axis of the printing reference system. It is noticeable that the top line in *Smart'ink* image (Figure 22) exhibits a significantly evident wavy edge, whereas the bottom line features a very clear and smooth edge. In the first line, the spacing was set too large, causing the droplets to not uniformly merge, remaining distinctly separate.

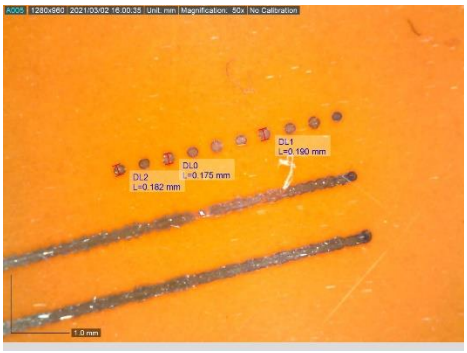

Figure 22 Example of drops and lines printed. Optical image taken with Dinoscope microscope.

Subsequently, an array was printed to set the spacing along the y-axis of the printing reference system, parallel to the x-axis. Similar considerations were taken into account by trying different spacings and finding the optimum balance between overly spaced and excessively close droplets. In Figure 23, you can observe an example of an array with well-defined edges, devoid of overflowing or void regions. Any printing defects primarily arise from imperfections in the printing substrate rather than errors in the printing parameter settings.

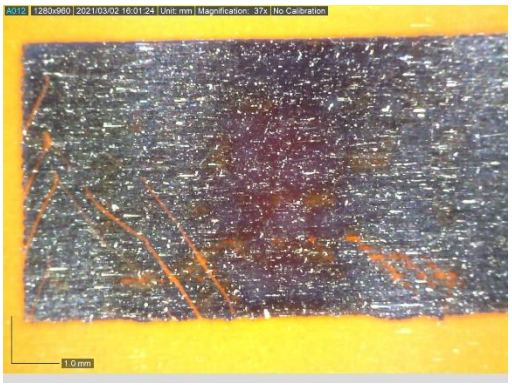

Figure 23 Example of array printed. Optical image captured with optical Dino microscope

This is how the final test involves printing a geometry that has become the standard for the electro-adhesive devices, which are the focus of this thesis: the interdigitated geometry. For a detailed description of the geometry, please refer to Chapter 3 or 5. It consists of a series of arrays placed at a distance of 300 µm, which requires precision in both the nozzle's placement on the substrate and the printing parameter settings. Since there are two comb-shaped electrodes interposed, any ink overflow within an array would compromise the entire printing result and the functionality of the electrodes. In Figure 24, you can observe a zoomed-in portion of a printed geometry and appreciate the definition of the lines and edges.

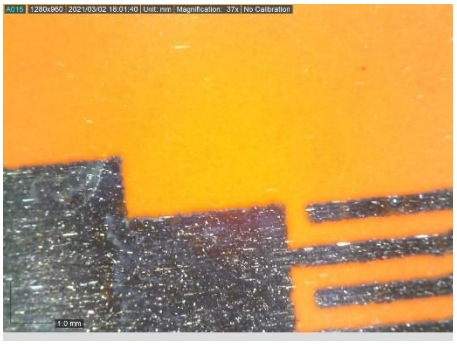

Figure 24 Example of arrays for the interdigital geometry

The ink is initially dried on the print bed at 50°C, and subsequently sintered in an oven at 150°C to fully melt the remaining silver particles, forming a uniform conductive layer.

Both inks have shown great potential for printing on Polyimide, delivering excellent results in terms of array filling and edge line quality. However, the *Smart'ink* has occasionally yielded better results, resulting in sharper lines and more precise dimensions. The significant difference lies in the print preparation, specifically in nozzle cleaning and maintenance, as well as the standby times allowed before nozzle clogging due to ink solidification. The *Smart'ink* requires a specific solvent provided by the ink manufacturer based on an oily substance that is challenging to remove and leaves residue on the nozzle even after multiple rinses with isopropyl alcohol (IPA). On the other hand, the *Anapro* ink allows for easier cleaning with just the use of IPA, and, optionally, the use of Micro90 soap dissolved in distilled water, a specialized product for cleaning electronic components. Additionally, the *Anapro* ink enables the printer to be on standby for hours without drying issues, while the *Smart'ink* has had more problems in this regard. This is why the ink ultimately used and accepted as the standard for producing electro-adhesive devices is *Anapro*. It consistently delivered reliable and repeatable results in all the works conducted in this manuscript.

Experimental results of this ink deposition of Anapro on PI 25 µm test are shown in Figure 25.

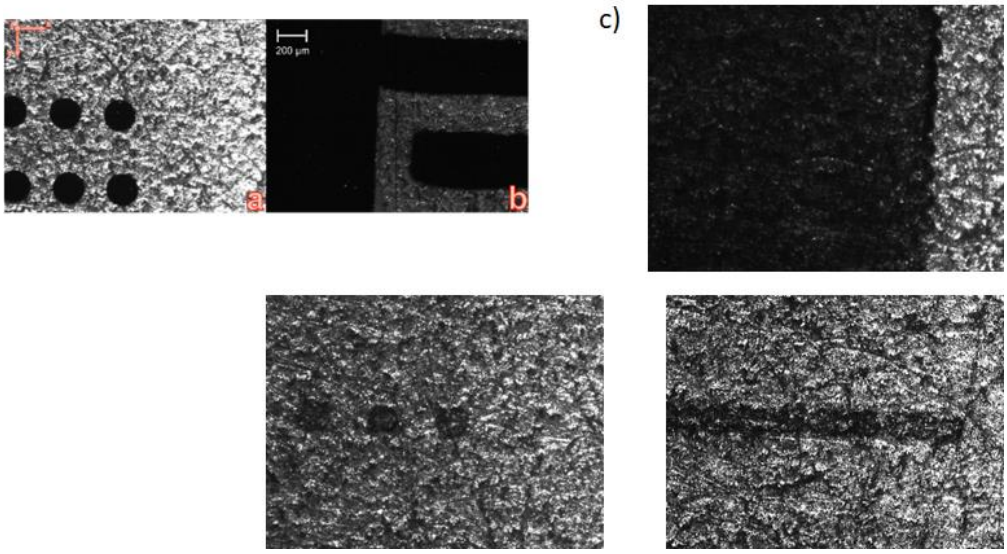

Figure 25 - Anapro DGP-40LT-15C on Caplinq Polyimide: a) distinct droplet spaced by 0.3 mm. b) part of an interdigitated geometry with droplet spaced by 0.17 mm along x and 0.2 mm. c) Droplets, line and array of Smart'ink

Chapter 6. Assessing the relationships between interdigital geometry quality and inkjet printing parameters

6.1 Introduction

In recent decades, the fusion of computer-aided design and 3D printing techniques has ushered in a significant transformation in manufacturing processes across various scientific domains, including biology, life sciences, and robotics. Specifically, inkjet printing has gained widespread recognition as a high-precision additive manufacturing method for fabricating devices like transducers [32] and sensors [49]. Inkjet printing technology encompasses two main subcategories: continuous and drop on demand (DoD). Continuous inkjet printing ensures a constant production of ink droplets, facilitating high-speed printing processes, particularly for industrial applications. In contrast, DoD inkjet printing ejects single droplets from the nozzle, resulting in smaller droplet sizes and enhanced placement accuracy [37]. While other techniques like screen printing, spin-coating, top-down etching, or blade casting are frequently employed due to their cost-effectiveness and capacity for covering large areas [51], they often require contact with the sample and the use of masks. DoD inkjet printing, being contact-free and maskless, operates in a digitally controlled mode, allowing for the design of micrometer-scale geometries. This quality makes it an ideal choice for applications involving flexible electronics, such as microelectromechanical systems [38], dielectric elastomer transducers[2], and electro-adhesive devices[31]. All these applications demand high-precision technology working at the micrometer scale while offering the flexibility to design geometric shapes freely.

This chapter introduces a methodology for establishing an optimal range of printing parameters to ensure accurate inkjet printing results, specifically using the JetLab 4x DoD inkjet printer described in 4.5 . Although printing result is influenced by various variables, such as ink properties and environmental conditions, which are not considered in this context, this systematic approach is a valuable tool for enhancing the reliability of printer settings, particularly for producing EADs in high-reliability demand fields. It has been already (4.4 highlighted the significant influence of material selection and the interaction between ink and substrate on the outcome of inkjet printing processes. The literature has delved into topics like ink droplet delivery from the nozzle to the substrate [52] and jet fluid dynamics[53], [54]. However, there is a noticeable gap in the existing literature regarding systematic approaches that explore the relationship between process parameters and resulting geometric output. Additionally, there is a lack of findings on the optimal set of parameters for the printing process, particularly in the context of using statistical methods such as Design of Experiments (DoE)[55]. It's essential to note that the outcomes of this procedure are specific to the ink-substrate combination used in this context. Nevertheless, the proposed methodology can be extended to accommodate other ink or substrate materials. The interdigital geometry, composed of two interlocked comb-shaped structures and known for enhancing performance, has found extensive use in creating electrodes for flexible and stretchable sensors, transducers, and electro-adhesive devices. In this study, the interdigital geometry is selected as a representative example, given its requirement for precise printed lines separated by a uniform gap. Consequently, this work presents a methodology for defining an appropriate range for key printing parameters, including the spacing between successive drops deposited on the substrate, the printing speed, and the nozzle temperature. The primary objective is to ensure the high accuracy of the printing process output. This goal is accomplished through a well-designed experimental campaign developed in accordance with the principles of Design of Experiments. The performance analysis of the printing process relies on geometric parameters extracted from images of the manufactured samples using a MATLAB algorithm. The relevant printing parameter set is identified through user experience, aiming to minimize the number of variables affecting the experiments while still considering the factors that predominantly influence the printing process, which have been defined as follows:

1. The spacing between successive drops deposited on the substrate, along both the x and y directions.
2. The printing speed, representing the travel speed of the printhead.

3. The nozzle temperature.

These parameters are varied to assess the relationship between parameter values and printing accuracy. The parameter value ranges were established through preliminary empirical approaches to reduce the number of experiments significantly. This preliminary empirical approach is essential to avoid testing entirely unfeasible parameter values, such as excessively wide spacings or excessively high printhead speeds. The droplet spacing directly influences the geometry's shape by affecting ink spreading. Extremely close droplets may lead to undesired ink accumulations, resulting in overages and uncontrolled irregular boundary formation. Conversely, droplets placed too far apart may prevent the formation of contiguous lines, resulting in dashed or dotted geometries. While a satisfactory printing result can be achieved through empirically defined spacing, finding the most suitable spacing configuration for a specific desired geometry is a more complex task that necessitates a systematic approach. The printing speed can induce droplet instabilities or deviations in droplet trajectory, particularly during changes in printhead motion. Excessively high speeds can lead to rapid printhead accelerations during the printing process, resulting in increased inertial forces, machine vibrations, and viscous friction caused by the surrounding air, all of which can significantly affect droplet flight. The nozzle temperature plays a critical role in modifying ink behavior, as it influences ink properties during and after ejection from the nozzle tip. In general, fluid temperature modulates its viscosity, and after several tests, it was observed that changes in nozzle temperature impact the printing outcomes. The chosen geometry, an interdigitated pattern of two comb shapes, is frequently employed in this thesis due to its common usage in electroadhesion applications, where it necessitates precise printed lines separated by a uniform gap. The printed patches are analyzed using an image processing algorithm developed within the MATLAB environment. This algorithm provides measurements of parameters of interest, facilitating a statistical study encompassing the entire dataset. The study's objectives are met through a well-structured experimental campaign developed in accordance with the principles of Design of Experiments (DoE).

6.2 Geometry design and manufacturing

The interdigital geometry is printed as a combination of several drop arrays using the MicroFab Jetlab 4xl printer, described in 4.5 , equipped with a 50 µm diameter piezoelectric nozzle.

A commercial conductive silver-nanoparticle ink (Smart 'Ink S-CS01130 from Genes 'Ink) is used to print due to the high ink stability for droplet formation, good reproducibility of the geometries and its low resistivity (around 15 µΩ/cm). The ink is prepared to be printed by filtering it with a 0.45 µm PTFE syringe filter and 5 minutes of ultrasonic bath to dissolve any particle aggregation. Once the geometry is printed, the ink is cured in an oven at 150°C for 40 minutes.

A polyimide (PI) film 25.4 µm thick is used as substrate. The substrate is industrially produced in rolls by Caplinq (PIT1N/210), and it has been preferred to a custom realization to guarantee the uniformity of the substrate avoiding interference with the ink distribution in the printed pattern. No treatment has been performed on the substrate prior to printing to prevent damages due to undesired erosions.

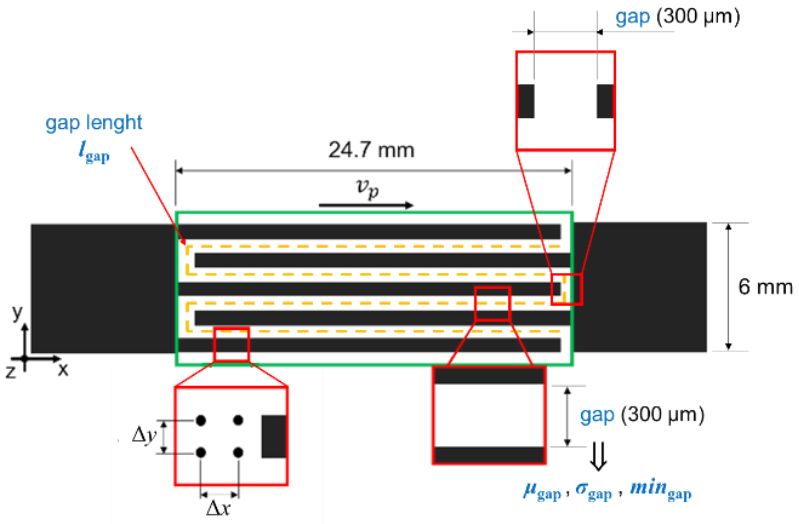

Figure 26 - Interdigital geometry with nominal dimensions and relevant parameters

The interdigital geometry is printed as a combination of several drop arrays, formed by droplet rows and columns. The printing direction corresponds to the main length of the array that is the x-direction (Figure 26).

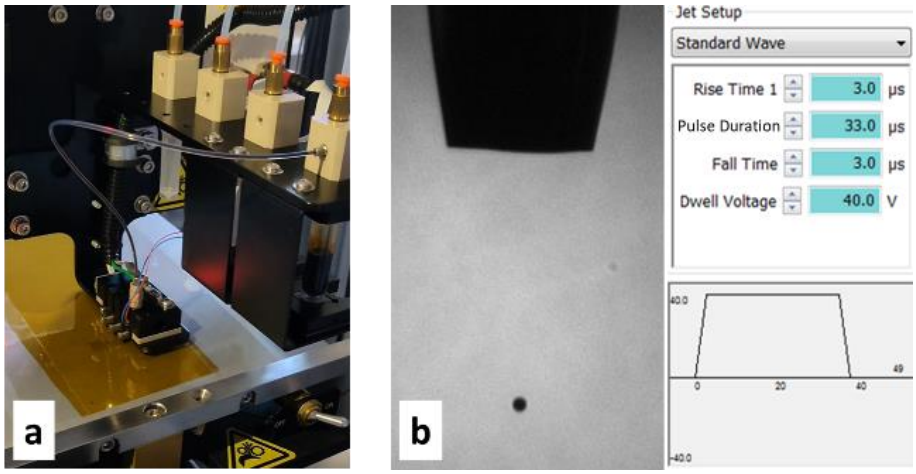

Figure 27 - a) Microfab Jetlab 4xl, b) control panel for droplet formation parameter settings

The printer configuration, which comprehends the voltage waveform and printing channel backpressure, is fine-tuned to ensure a consistent droplet flight and these settings remain unchanged throughout the entire experimental framework. As for the droplet formation parameters detailed in 4.4 a monopolar trapezoidal waveform is employed. This waveform features fixed rise and fall times of 3 µs, a dwell time of 43 µs, and a constant dwell voltage of 38 V, as visually depicted in Figure 27b. This figure also illustrates the resulting stable droplet formation. To maintain the stability of the ink meniscus at the nozzle tip, the reservoir pressure is set to -10 Pa.

6.3 Experimental design

The impact of these chosen parameters on process performance was thoroughly investigated within the framework of a well-structured experimental design (detailed in Table 2). The four key variables of interest encompass the printing speed along the x-axis, the subsequent drop spacing along the x-axis, the subsequent drop spacing along the y-axis, and the nozzle temperature. The printer software offers the flexibility to configure the voltage waveform that drives the oscillation of the piezo-crystal. A well defined drop ejected from the nozzle tip is visually confirmed in the left section of Figure 27b, captured using the infrared camera and the stroboscopic light system (4.5). The nozzle-to-plate distance was set at 1.5 mm based on

insights from prior experiments. Each variable factor was examined at two distinct levels, selected based on preliminary trials and considering machine positioning tolerance (typically ±30 µm in the x-y directions). This design resulted in 16 unique experimental conditions, with two replicates conducted for each condition. Notably, five replicates were carried out at each temperature level for the central point (v_p = 20 mm/s, Δx = 110 µm, and Δy = 140 µm). Consequently, the entire experimental design encompassed 42 individual runs, all executed in a fully randomized fashion.

Factor	**Symbol**	**Levels**	
		Low	**High**
x-axis spacing (µm)	Δx	80	140
y-axis spacing (µm)	Δy	110	170
Printing speed (mm/s)	v_p	10	30
Nozzle temperature (°C)	T_n	35	40

Table 2 - Experimental design summary

Table 3 lists the experiments parameter setup and the corresponding order of execution of tests. As can be noted, there is no correlation between consecutive experiments regarding the factors value variation. All tests were conducted at room temperature and during the same day.

Run Order	v_p	Δx	Δy	T_n		v_p	Δx	Δy	T_n		v_p	Δx	Δy	T_n
1	10	80	170	35	*16*	20	110	140	35	*31*	20	110	140	40
2	30	80	170	35	*17*	30	140	110	40	*32*	30	80	110	40
3	10	80	170	40	*18*	30	140	170	35	*33*	10	80	170	40
4	30	140	170	40	*19*	10	80	110	40	*34*	10	80	170	35
5	10	80	110	35	*20*	20	110	140	40	*35*	20	110	140	40
6	30	140	170	40	*21*	10	140	170	40	*36*	30	140	110	35
7	10	140	110	40	*22*	20	110	140	35	*37*	10	140	110	35
8	20	110	140	35	*23*	10	140	170	40	*38*	30	140	110	35
9	20	110	140	40	*24*	10	140	110	35	*39*	30	140	110	40
10	10	140	170	35	*25*	30	80	110	35	*40*	10	80	110	40
11	30	140	170	35	*26*	30	80	170	35	*41*	10	80	110	35
12	20	110	140	35	*27*	30	80	110	40	*42*	10	140	110	40
13	30	80	170	40	*28*	30	80	110	35					
14	10	140	170	35	*29*	20	110	140	35					
15	30	80	170	40	*30*	20	110	140	40					

Table 3 - Complete experimental campaign conducted following the Run Order

The results of this investigation are aimed at delivering statistical metrics that characterize the uniformity and excellence of the geometric outcomes. To comprehensively assess the outcomes of this factorial experiment, an Analysis of Variance (ANOVA) was conducted. The subsequent section elaborates on the chosen model, outlines the response calculation methods, and details the data acquisition and post-processing procedures.

6.4 Measurements and analysis

An optical microscope, specifically the Zeiss Stereo Discovery V20, was utilized to capture and assess the printed samples. Subsequently, a MATLAB code was executed to extract pertinent geometric parameters via image processing algorithms. The geometric parameters under evaluation (as illustrated in Figure 26) are defined as follows:

- Mean gap value (μ_{gap}): This parameter signifies the average width of the gap.

- Gap width standard deviation ($\sigma_{gap)}$: This parameter reflects the consistency of gap widths within the shapes.

- Minimum gap value (min_{gap}): This parameter can identify irregularities in the contour lines, such as excess ink deposits or interconnections between the comb-shapes.

- Gap length (l_{gap}): This parameter can reveal any discontinuities within the comb-shapes.

Within the MATLAB code, conventional image processing functions are applied to extract features from each printed sample, involving the binarization and labeling of identified blobs. The reference geometry consists of only two distinct blobs, corresponding to the two comb-shapes separated by a 300 µm gap along their entire length. Consequently, images containing more than two blobs indicate isolated or disconnected shapes, which are subsequently removed from the analyzed image.

The code computes the Euclidean distance between the two blobs for each pixel along the blob's contour. The mean value, standard deviation, and minimum value of the entire set of measured distances (μ_{gap}, σ_{gap}, and min_{gap}, respectively) are calculated, excluding distances that exceed a defined threshold (set at 500 µm). Gap length (l_{gap}) corresponds to the number of pixels for which a gap distance is calculated, which is then converted to millimeters. It's worth noting that, due to the distance threshold, any finger disconnections from the side rectangles or interruptions in random spots do not impact the calculation of μ_{gap} and σ_{gap} but do affect the calculation of l_{gap}.

Figure 28 - Example image of a sample acquired with Zeiss Stereo Discovery V20 optical microscope

6.5 Results and discussions

Appropriate models were examined to investigate the influence of the factors outlined in Table 1 on both the mean gap value (μ_{gap}) and the gap width standard deviation (σ_{gap}).

The ANOVA results are succinctly presented in Table 4, highlighting the statistically significant factors. For a more detailed representation of the outcomes concerning μgap and σ_{gap} for each factor, please refer to the graphical depictions in Figure 30, Figure 29, Figure 31.

Factors		**P-value**	
		$\boldsymbol{\mu_{gap}}$	$\boldsymbol{\sigma_{gap}}$
Main factors	Δx	**0.000**	**0.001**
	Δy	**0.000**	**0.000**
	v_p	0.166	0.243
	T_n	**0.030**	0.199
Interactions	$\Delta x*\Delta y$	**0.000**	**0.043**
	$\Delta x*v_p$	0.088	0.405
	$\Delta x*T_n$	**0.043**	**0.003**
	$\Delta y*v_p$	0.769	**0.021**
	$\Delta y*T_n$	0.523	0.353
	v_p*T_n	0.721	0.201

Table 4 - ANOVA p-values (bold = significant factor, confidence level α = 5%) for the analysis on the mean value and standard deviation of the gap

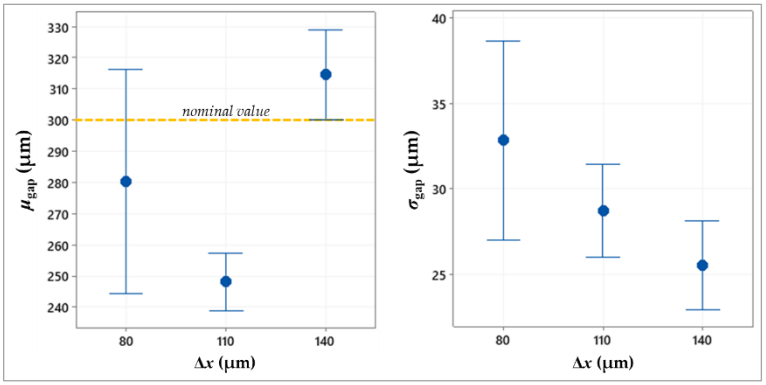

Figure 29 - Interval plot of the mean value and standard deviation of the gap against drop spacing along the x-axis

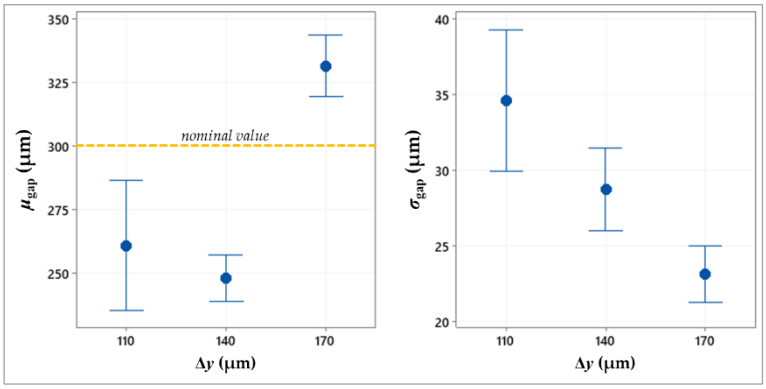

Figure 30- Interval plot of the mean value and standard deviation of the gap against drop spacing along the y-axis

In Figure 31, you can observe how the printing speed impacts both the mean value and the variance of the gap. When the printing speed is set at 10 and 30 mm/s, μ_{gap} closely matches the reference value. However, at 20 mm/s, the mean gap measures around 250 µm. Meanwhile, the gap variance remains relatively stable at approximately 29 µm across all speed values, with a noticeable reduction in oscillation at 20 mm/s.

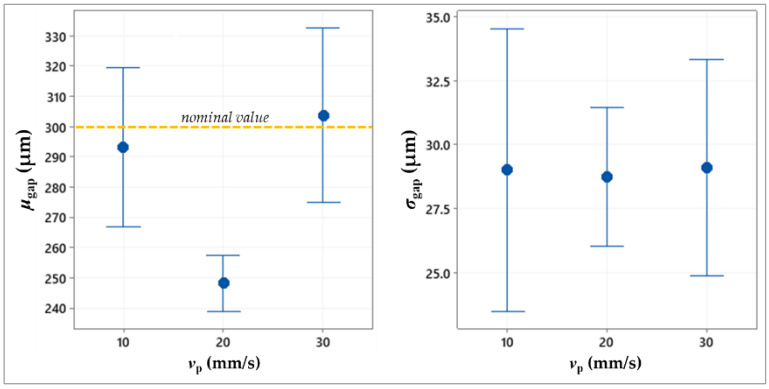

Figure 31 - Interval plot of the mean value and standard deviation of the gap against the printing speed

The nozzle temperature was found to have an impact on the mean gap size, with a decrease in gap size as the temperature rises (as shown in Figure 32). This effect is likely due to the influence of ink viscosity on temperature, resulting in increased ink spreading at higher temperatures.

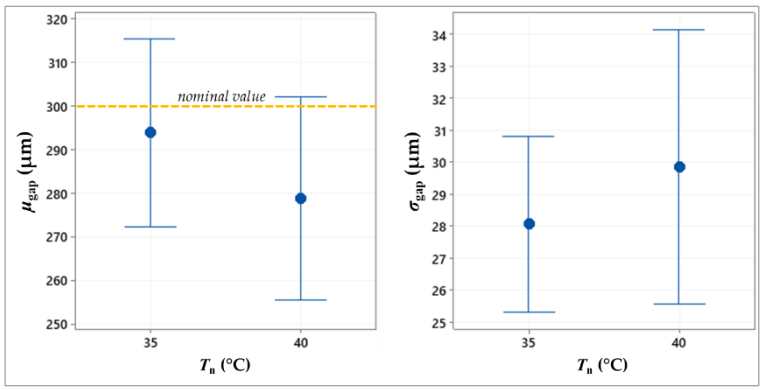

Figure 32 - Interval plot of the mean value and standard deviation of the gap against the nozzle temperature

Based on the summarized ANOVA results in Table 4, both responses are influenced by the spacing between subsequent drops along the x-axis and y-axis, denoted as Δx and Δy, respectively. When both of these factors increase, the mean gap size tends to have higher values that are closer to the nominal value (300 µm). Additionally, the standard deviation of the gap decreases. In either direction, increasing the spacing between subsequent drops reduces drop overlap and, consequently, limits the spreading of excess ink. This results in thinner and more consistent lines, contributing to the desired gap size and shape (σ_{gap} = 25.5 ± 4.9 µm at Δx = 140 µm and σ_{gap} = 23.2 ± 3.4 µm at Δy = 170 µm). Conversely, smaller spacing leads to unwanted ink exceedances, causing irregular boundaries and resulting in a decrease in the mean gap value and an increase in gap standard deviation. The ANOVA

results indicate that the printing speed (v_p) does not have a significant impact on either of the responses.

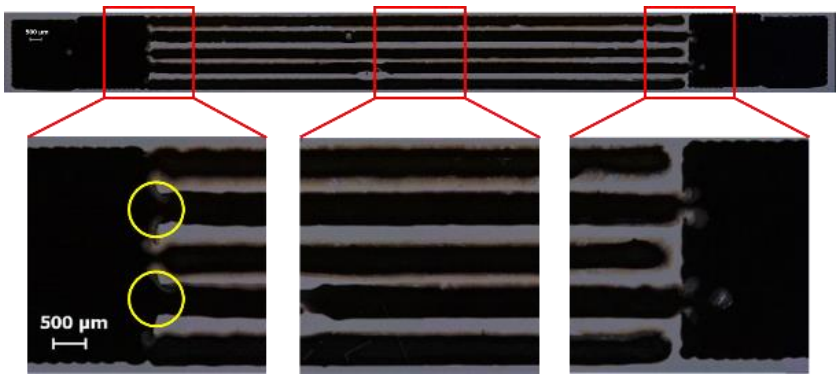

Figure 33 - Example of printed sample with interconnected arrays (Δx = 80 µm, Δy = 110 µm, vp = 10 mm/s, Tn = 40°C)

The minimum gap value (min_{gap}) and gap length (l_{gap}) were valuable for detecting undesirable conditions that deviated from the intended geometry. In Figure 34, the experimental results for the minimum gap value are presented. It is worth noting that a significant number of experimental conditions with Δx = 80 µm resulted in a min_{gap} value of zero (indicated by red diamonds). This implies that the comb-shapes are interconnected, as illustrated by the yellow circles in Figure 33, which distorts the intended geometry. Consequently, process parameter combinations involving a drop spacing of 80 µm along the x-axis are likely to be unsuitable.

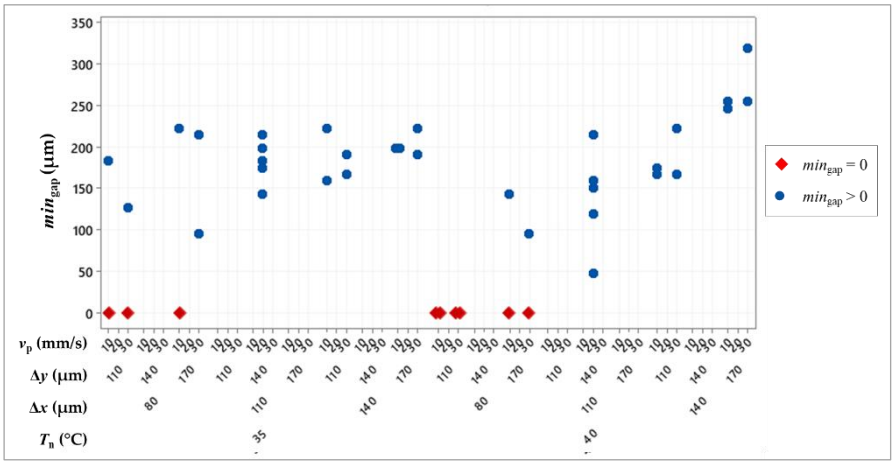

Figure 34 - Individual value plot of the minimum value of the gap

Figure 35 displays the measured gap length (l_{gap}) values for the samples without interconnections. A significantly lower gap length than the nominal value of 100 mm (as indicated by the red diamonds)

implies the presence of disconnections at the beginning of a finger, as illustrated in Figure 36a. Conversely, a slightly lower gap length than the nominal value (represented by the green squares inFigure 35) indicates a disconnection at some intermediate point along a finger, as shown in Figure 36b.

The experimental data do not reveal clear relationships between the process parameters and these disconnections. These issues are likely to be caused by random factors, such as dust or anomalous interactions between ink and the substrate, potentially due to substrate defects or ink aggregates.

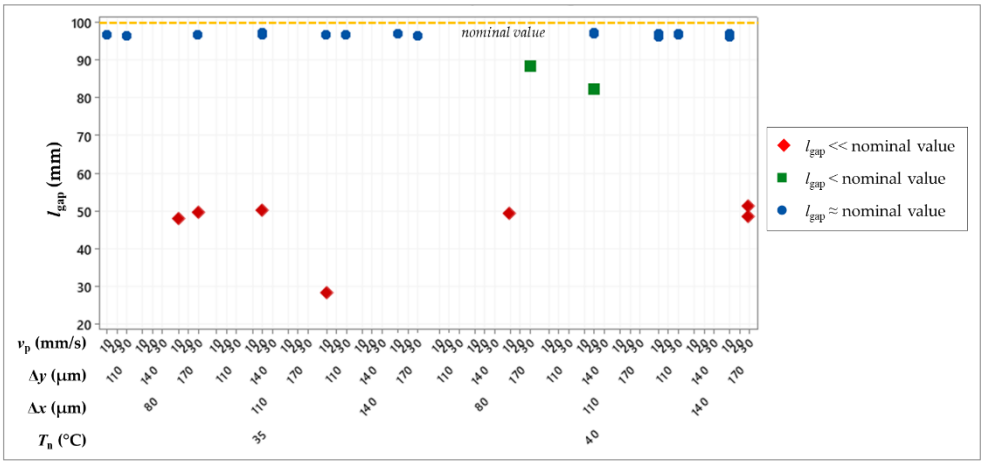

Figure 35 - Individual value plot of gap length

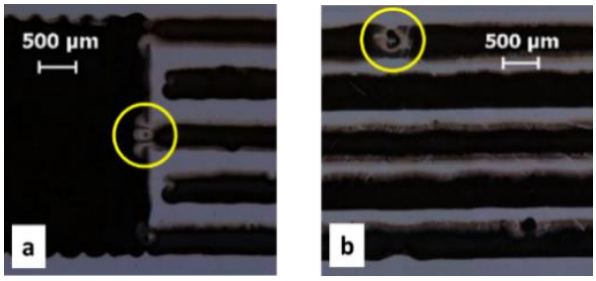

Figure 36 - a) Example of disconnection at the array beginning (Δx = 140 mm, Δy = 170 mm, vp = 30 mm/s, Tn = 35°C); b) Example of intermediate disconnection (Δx = 110 mm, Δy = 140 mm, vp = 20 mm/s, Tn = 40°C)

As a conclusion, this study explored the application of DoD inkjet printing technology for producing a micrometer-scaled representative geometry, namely the interdigital geometry comprising two interlocked comb-shapes. An appropriate experimental design was developed to investigate the impact of drop spacing, printing speed, and nozzle temperature on the printing process outcomes. The

experimental findings demonstrated that both the drop spacing along the x-axis and y-axis affected the width and regularity of the gap between the comb-shapes. Notably, the spacing along the printing direction (x-axis) played a critical role in preventing interconnections between the comb-shapes. Furthermore, the results indicated that the nozzle temperature influenced the mean gap value, while the printing speed did not have a significant impact on the analyzed responses. Based on these findings, the parameter combination of $\Delta x = 140$ μm, $\Delta y = 170$ μm, and $T_n = 35$°C is recommended for achieving accurate printing outcomes, producing geometries without interconnections or disconnections and with a gap size close to the target. The choice of printing speed within the investigated range is flexible, but using $v_p = 30$ mm/s can enhance process productivity. The experimental results also revealed that the process outcomes were influenced by issues related to substrate damage or the presence of dust fibers. Therefore, conducting printing in a controlled environment could mitigate these issues and enhance the quality of the manufactured geometries. This work has established a reproducible methodology for examining the relationships between geometric parameters and printing variables, which can be extended to other ink-substrate combinations. The developed analytical tools could also be employed in a quality assessment procedure for batch-produced inkjet-printed shapes, including the evaluation of additional quality indices such as the presence of internal holes (empty spots in the printed shapes, as shown in Figure 37).

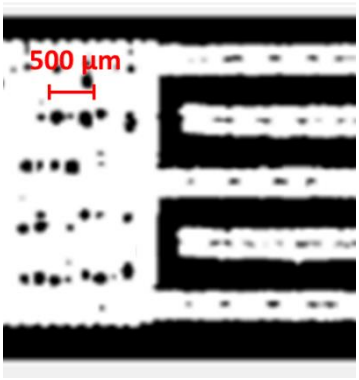

Figure 37 Binarized image of a sample including internal holes, which are the black spots in the white comb-shapes ($\Delta x = 140$ mm, $\Delta y = 170$ mm, $vp = 10$ mm/s, $Tn = 35$°C

Chapter 7. EAD manufacturing

In this chapter, we will describe the manufacturing process of the electro-adhesive devices (EADs) produced in our laboratory, which are the focus of this thesis and have become a standard for comparison with various manufacturing methods and materials. Building upon the work of Berdozzi [23] this technique has been developed and standardized to ensure excellent repeatability in product quality, high reliability in results, and consistent production timelines.

7.1 EAD design

The chosen design is a uni-layer configuration where the electrodes are printed using inkjet printing on a 25 μm thick Polyimide substrate. The electrode geometry is interdigitated, consisting of two comb shapes interposed with a constant gap in between (6.2). The electroadhesive area is defined by the comb teeth, which represents the region with the highest electric field intensity when powered. The parameters defining this geometry are shown in Figure 38 and include:

1) Electrode Width (w): This parameter determines the amount of charge that can be accumulated on each tooth of the comb.
2) Electrode Gap (g): It defines the capacitance of the capacitor, thus influencing the energy storage capacity.
3) Thickness of the dielectric substrate: This, along with the thickness of the insulating layer (Tml and tdiel), impacts the polarizability of the device and the force acting on the object to which it adheres.
4) Electroactive Area (LxW): This defines the area covered by the interdigitated electrodes, representing the region with the most intense electric field, polarization, and electro-adhesive gripping potential.

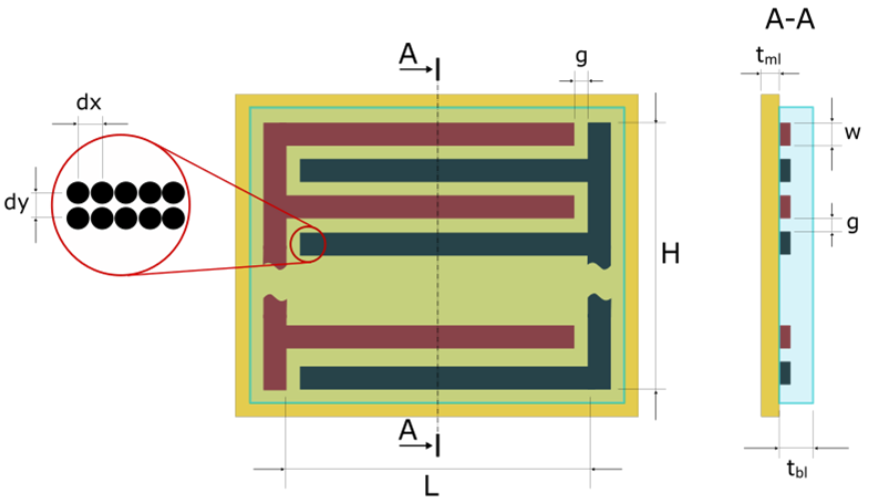

Figure 38 Interdigital geometry parameters

Two conductive paths are then provided for powering the device and for electrical connection to the power supply.

7.2 EAD manufacturing

The MicroFab Jetlab® 4xl drop-on-demand inkjet printer, equipped with a piezoelectric nozzle of 50 µm diameter (MJ-AT-01), as described in 4.5 is employed for creating the electrode patterns. A commercial silver nanoparticle ink, DGP 40LT-15C by Anapro is selected for electrode fabrication. This ink is specifically designed for direct inkjet printing without the need for additional solvents. It demonstrates excellent compatibility with plastic film substrates, low resistivity (in the range of 11-12 µΩ·cm), and moderate curing temperatures (in the range of 120-150 °C). The ink is jetted using a monopolar trapezoidal voltage waveform with rise and fall times of 3 µs, a dwell time of 33 µs, and a well voltage of 38 V.

To prepare for printing, the ink undergoes an ultrasonic bath to remove any potential aggregates. Once loaded into the machine and introduced into the printing channel up to the nozzle tip, a negative pressure of 14 mmHg is applied to keep the ink at the orifice tip, forming a flat meniscus. The nozzle is maintained at a temperature of 35°C, and the system is allowed to rest for 5 minutes to achieve ink stability. Through the camera system, a stable droplet is created, indicating that the ink is ready for printing. The substrate, a 25 µm Polyimide (PI) by Caplinq, is cleaned with isopropyl alcohol (IPA) and a lint-free cloth, cut, and placed on the printing platen. It's essential to avoid harsh treatments on the substrate or the use of compressed air since it is easily damaged and can become electrostatically charged, which would adversely affect the printing quality. The printing plate is kept at 50°C and all the solvent residuals after cleaning evaporate fast. The electrode printing is executed using a machine language code stored in a .txt file. This code defines the printing sequence for all the arrays that make

up our device. In the case of printing multiple units, it has been empirically observed that printing the first half of each device, allowing the ink to dry on the printing platen, and then printing the second half results in better-defined array lines and reduces printing failures or interconnections between the teeth of the combs. After printing the electrodes, the PI sheet is placed in an oven at 140°C for one hour to complete the sintering process. This allows the silver nanoparticles to melt, creating the desired electrode conductivity. In the end, the insulating layer, which serves as the second dielectric substrate in the EAD structure and can be referred to as the backing layer, is deposited. The deposition of this layer is crucial for the success of the device as a whole and is a delicate process that must be carried out as cleanly as possible. This is because any impurity, imperfection, or trapped air bubble in this layer can lead to the premature failure of the device. The deposition process is divided into four steps once the mixture is prepared. A blend of Silpuran® 6000/05 components (part A and part B) is prepared by adding a solvent (IPA) to reduce the compound's viscosity and help the mixing process. The mixture follows a weight ratio of 28% (part A and part B) and 44% of solvent. Specifically, the blend is homogenized using a planetary-centrifugal mixer (Thinky ARE-250) for 2 minutes at 2000 rpm and then subjected to degassing for an additional 2 minutes at 2000 rpm. The degassing step is crucial to expel undesired air bubbles. This procedure is repeated twice to obtain a homogeneous and viscous mixture.

The Polyimide (PI) sheet with printed and cured electrodes undergoes a plasma treatment to clean the surface and enhance PI-PDMS adhesion. This is because exposure to oxygen plasma (Diener ATTO) introduces polar functional groups to the substrate, altering surface chemistry, increasing the potential for chemical and physical interactions between molecules on the two bonding surfaces, and raising the surface energy of the polymers. The machine is set at 50% power (60W), with oxygen pressure at 0.8 bar and a 1-minute exposure time. These settings provide excellent surface activation and imperfection cleaning without compromising electrode quality. Higher power, lower pressure, or longer exposure times could erode the electrodes, resulting in insufficient conductivity and significantly impacting device performance.

After exposing the Polyimide (PI) sheet with printed electrodes to oxygen plasma, a silicone primer (DOWSIL™ 1200 OS) is manually applied using a sponge-tipped applicator. Applying a primer creates bridges of silicate-containing monomers to facilitate the connection between the PI chains on the surface and the subsequently deposited PDMS. During silicone curing, these groups react with the polymeric chains of heat-cured silicones, enhancing bonding to various materials, including metals, ceramics, glass, wood, masonry, and structural plastics. Following application, there is a 10-minute waiting period for the primer to dry and be ready for the PDMS deposition. This process is conducted within a laminar flow hood with 50% humidity and a temperature of 26°C.

The air-bubble-free mixture is being blade-cast using an automatic doctor-blade film applicator (TQC Sheen AB3655) equipped with a micrometer-height adjustable blade (VF1823), set to 400 µm, and moving at 1 mm/s. The whole procedure is being performed in a laminar flow hood with 50% humidity and a chamber temperature of 26°C. Samples are resting for two hours after the casting, preventing air bubble formation caused by fast solvent evaporation when specimens are placed in the oven immediately after casting. After two hours of resting, the PI film, with insulated electrodes, is placed in the oven at 120 °C for one hour for curing. The resulting layer exhibits a volume reduction of around 75%, featuring a thickness of 100 µm. Samples are then cut as single units with a blade cutter.

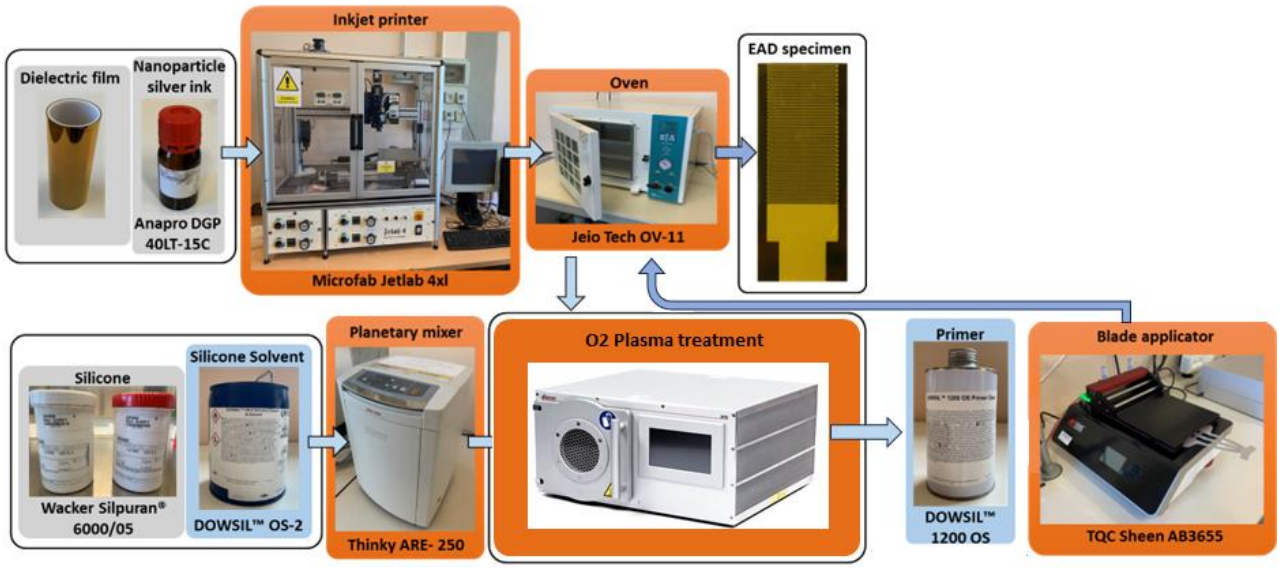

Figure 39 EAD manufacturing process steps

7.3 EAD test

The testing methodology for ESS measurement and breakdown voltage assessment is later described. The performance evaluation is referred to what has been described in 2.2 .

The test bench used in this work consists of a fixed stage, where the specimen is blocked and powered, and a linear guide, driven by a DC motor, hosting the load cell and the grasped test film. The real test bench is depicted in Figure 40.

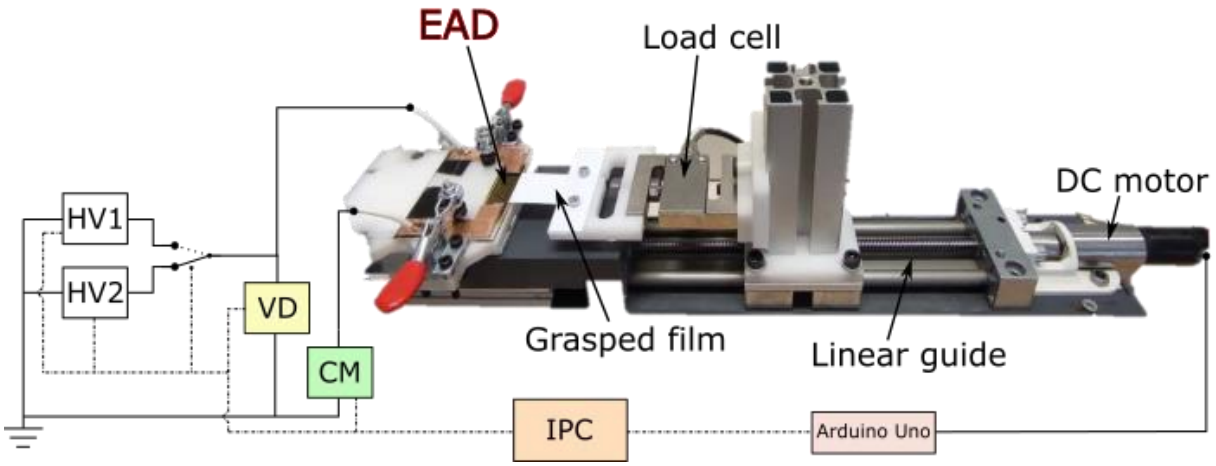

Figure 40 – Test bench for shear force evaluation and circuit schematic

In the set-up, the EAD sample is sandwiched between two PMMA plates used as sample holders, leaving the adhering surface free and assuring a correct position of the specimen with respect to the moving part of the bench. Furthermore, the top holder plate covering the EAD is equipped with copper strips for the electrical connection of the specimen electrodes. The testing substrate is aligned with the EAD specimen surface and load cell (NS-WL1-10 kg), whose height is adjusted by a vertical rail. An IGUS linear guide controlled by a DC motor (FAULHABER Series 2342 CR) forces the paper sheet to move on the plane of the EAD adhering surface. The testing set-up replicates the ISO 8295 standard requirements to determine the friction coefficient of the main dielectric layer over the PET substrate. Commanding and measurements signals are managed by Beckhoff IPC equipped with I/O modules (EL3356, for interfacing loadcell; EL3104, for analog inputs; EL4732, for analog outputs, EL2004 for digital outputs) at a sampling frequency of 2kHz. Beckhoff IPC also pilots an Arduino Uno which drives the DC motor. Two high voltage (HV) power supplies are deployed and toggled by a controlled relay:

- HV1: Ultravolt 10HVA24 is used for ESS tests due to its high precision and fast dynamic response output voltage, enabling bipolar AC and DC HV signal generation with a maximum amplitude of ±10 kV.

- HV2: Ultravolt 40A12-P4-E is used for breakdown tests instead, capable of unipolar 40 kV DC HV signal generation.

Both power supplies provide monitoring signals for voltage and currents at the output side. However, external circuitry for current and voltage measurements at the specimen side are deployed to detect directly voltage applied to the EAD and the current flowing in and out the specimen. A voltage divider (VD), described in Figure 41, is connected in parallel to the EAD, providing a buffered voltage monitoring signal isolated from the high voltage side.

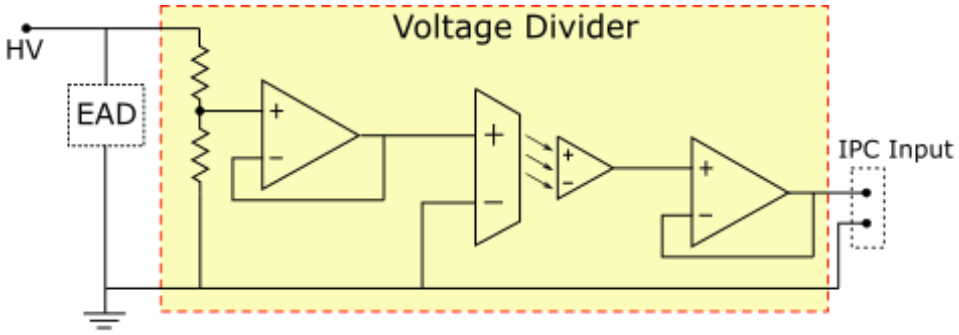

Figure 41 - Electrical scheme of the voltage divider interfacing with the IPC input module EL3104

In series with the EAD is connected a current monitor (CM). This circuitry is based on an inverting amplifier, whose output signal was also buffered, as shown in Figure 42.

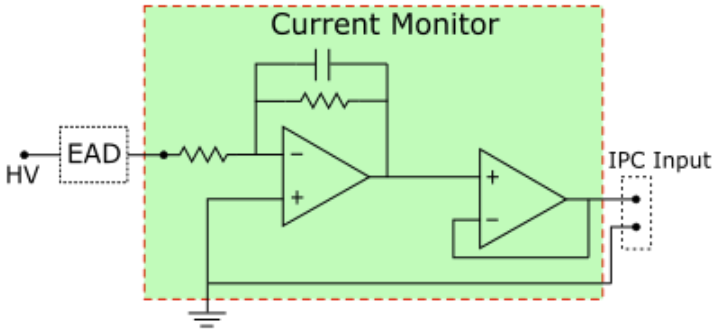

Figure 42 - Electrical scheme of the current monitor interfacing with the IPC input module EL3104

Signal buffering aims to increase the input impedance of the measuring unit, preventing current flow inside the control unit. The mechanical part of the experimental setup interfaces with the electrical circuitry as shown in the Figure 40. The EAD is positioned and blocked on the fixed stage while the grasped test film is connected to the force sensor mounted on the motorized linear guide. The specimen is placed in contact with the testing substrate under a homogeneous pressure of 600 Pa generated by a reference load, as suggested by [24]. A high voltage signal is applied to the EAD from the power supply and, after two seconds, the grasped film is pulled away from the motor while recording the tangential force. This procedure is repeated four times for each voltage step amplitude, inverting the polarity each time, providing a consistent data set for an ESS results statistical analysis and ensuring depolarization effects that lead to an electric field saturation with consequent force reduction. The ESS value is calculated as the measured peak take-off force divided by the tested specimen electroactive area. The latter is obtained as the multiplication between L and H, as indicated in Chapter 7. When performing ESS test, a controller constantly checks whenever the current exceeds the 80% of the maximum measurable current of 100 µA. If this happens, the experiment is stopped,

and the specimen is considered as electrically broken. This control layer allows to determine the safe EAD operation, without considering ESS data after electrical discharges that burns the electrode strips without permanently shortcutting the device.

Breakdown voltage assessment follows the standard ASTM D149 [27], which specifies the test methodology for the dielectric strength of solid electrical insulating materials at commercial power frequencies. Specimens breakdown must occur within 10 - 20 seconds after the test begin while subjected to a ramp voltage signal, as suggested by the so-called Short-time test method. EAD specimens, placed on the fixed stage of the test bench, were powered with a ramp voltage signal until electrical breakdown occurred. The current monitor continuously measures the absorbed current. When it exceeds 80% of the maximum measurable current of 100 μA, the test is stopped. The breakdown voltage corresponds to the applied voltage at the time the test was interrupted.

Chapter 8. Increasing the performance of Electro-adhesive devices via inkjet printing

8.1 Introduction

In general, the EA force depends on a multitude of physical variables[8],[56] comprehending the electrical and mechanical properties of both the device and the adhered object. The dielectric constants, dielectric strength, thicknesses, roughness, and resiliency of the materials composing the EAD are crucial properties affecting its performance, which also directly depends on the device layout and the fabrication process adopted. Different EADs innovative manufacturing procedures (e.g. spin coating[33], inkjet printing,[57], blade casting[58], screen printing[59]) are presented in recent literature allowing a rapid and effective production of flexible and stretchable devices. The material choice, the geometry of the electrodes, together with the total complexity and the time requirement of the manufacturing process are main aspects to be investigated in order to compare different results. The most relevant achievements in EADs performance regard the electroadhesive shear stress exerted during the gripping action related to the voltage applied and to the layout of the device. Ruffatto et al.[33] reached 62 kPa while adhering glass at 5kV with a rigid EAD having circle-shaped copper electrode made by chemical etching, featuring a gap distance of 600 µm, and spin-coated with silicone. Shea et al.[60] obtained 35kPa at 5kV, grasping a paper foil, with a completely silicone based flexible and stretchable EAD produced by silicone membranes blade casting and bonded with oxygen plasma exposure. The device featured an electrode gap of 500 µm and a dielectric layer thickness of only 50 µm. Berdozzi et Al.[23] also proposed a flexible EAD having inkjet-printed electrodes embedded in a thin structure made of Polyimide and blade-casted silicone layer. The produced EAD featured a 300 µm gap between the electrodes and the adhesive pressure reached 56 kPa at 7 kV while gripping a PET film. A complete summary of the main results in literature is also presented, comparing different materials and production methods.

Over all other manufacturing techniques, Inkjet printing exhibits the highest versatility in the geometry design and prototyping procedure[32]. In particular, Drop on Demand (DoD) inkjet printing offers a digitally controlled precision in depositing drops of conductive or dielectric ink forming line paths or layers[10]. Compared to the other manufacturing processes mentioned above, DoD avoids the contact with the substrate onto which the inks are dispensed, as the chemical etching does by

employing masks, and it increases the line resolution and smoothness respect to industrial production printing processes (e.g. screen printing). Only a few studies report notable grasping performances of EADs manufactured via inkjet printing[23], [48].

This work proposes a novel manufacturing procedure to produce an EAD fully printed via DoD inkjet printing technique. In this case of study, the electrodes isolation layer is inkjet-printed by using a dielectric ink with high dielectric constant and then it is characterized as gripping layer. This process allowed to finely tune the geometry and thicknesses of the device making it conformable and suitable for specific applications. The proposed methodology and materials employed allowed to obtain three times the performances found in literature regarding different production processes. Manufactured samples have been characterized through an experimental campaign investigating two main factors: the electro-adhesive shear stress (ESS), since shear forces are much higher than normal and peeling EA forces[14], and the breakdown voltage (BD). An analysis of production times and sample size scalability will provide additional insights regarding practical applications of this class of devices.

8.2 Experimental design

In this section a technical description of the manufacturing procedure to produce the Electro-adhesive device (EAD), object of this work, is presented. First, the geometry of the electrodes and the layout of the entire EAD are described (6.2), as well as the detailed fabrication process 7.2 . A particular focus on the deposition of the dielectric ink layers outlines the advantages in employing it as gripping layer. Then, the test setup and procedure subsections (7.3 explain the overall methodology to assess the performance evaluation in terms of the Electro-adhesive Shear Stress exerted on a target substrate and the power voltage value at which the breakdown of the dielectric medium occurs.

8.2.1 EAD design

The Electro-adhesive device presents two conductive electrodes featuring an interdigital, or comb-shaped, geometry. Figure 43 shows a schematic of the interdigital EAD layout[23], indicating the design parameters. Each comb-shaped electrode ‘finger’ has a defined width (*w*) and is separated from the others by the electrode gap (*g*). The EAD length and width are indicated with L and W, defining the total EAD electro-adhesive active area, calculated as A=L x W. Then, the EAD presents two conductive rectangles on the device sides, used for the electrical connection with the power supply, as shown in Figure 43. The electrodes are interposed between two dielectric layers having distinct functionalities. One acts as deposition substrate for the electrodes, while the other aims to insulate the device covering the electrodes. The thicknesses of the electrode deposition substrate and

the insulating layer are indicated respectively with t_{sub} and t_{ins}, while the electrode thickness is negligible.

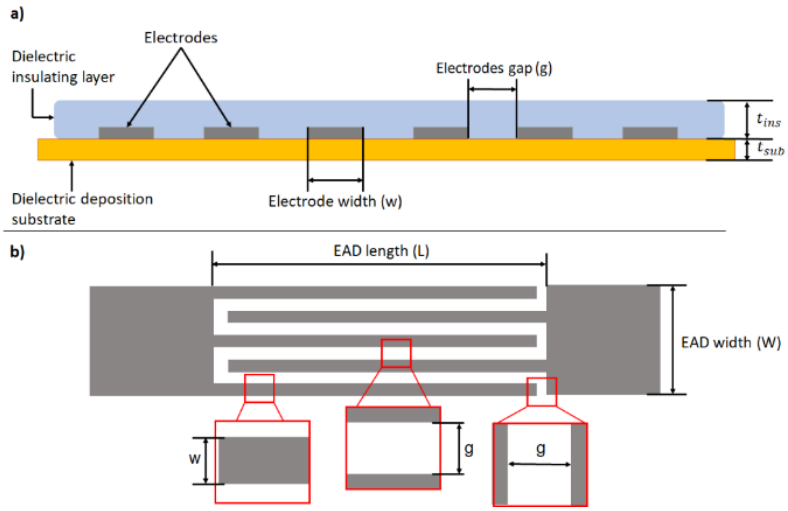

Figure 43 a) Sample layers structure: the dielectric insulating layer (light blue region) and the electrodes (grey rectangles) are deposited on a Polyimide deposition substrate. The thicknesses of the insulating and deposition layer are denoted with t_{ins} and t_{sub} b) Interdigital geometry scheme: the EAD length (L) and width (W) define the electro-active area of the device. The comb-fingers width (w) and the electrodes gap (g) are highlighted. The main rectangle at the left and right of the active area are conductive regions to better power the device.

8.2.2 EAD fabrication

A Polyimide (PI) foil (Caplinq LINQTAPE PIT1N/210), with a thickness of 25.4 µm, is used as the deposition layer for the electrodes. This PI film features a dielectric constant of 3.5, a dielectric strength of 245 MV/m, and a volume resistivity of 1 MΩ·cm, highlighting good insulating properties. Besides, a tensile strength of 165 MPa provides high mechanical resistance to traction, while a continuous use temperature of 260°C allows adopting thermal treatments without altering film mechanical properties.

The electrodes and the *insulating layer* are printed with Drop on Demand (DoD) inkjet printing technique, using a JetLab 4xl provided by Microfab and equipped with a piezoelectric nozzle. A monopolar trapezoidal voltage waveform is set to actuate the jetting device. The conventional parameters defining the waveform are the voltage amplitude, the rise time defined as the time in which the pulse reaches the amplitude value, the dwell time that is the duration of the impulse, and the fall time representing the time required to drop the voltage to zero value (Figure 44b). The motion of the printing plate defines the x-y reference system (Figure 44c). By convention, the x and y axis correspond respectively with the printing direction and the orthogonal one. Finally, the printhead's vertical motion defines the position on the z-axis, which is fixed for the entire printing process at 1.5 mm from the printing plate (Figure 44c). To ensure a stable ink phase inside the printing channel

during the whole process, the nozzle temperature is set to 35 °C. To accelerate solvents evaporation, thus increasing ink stability after its deposition, the printing plate temperature is set to 50 °C.

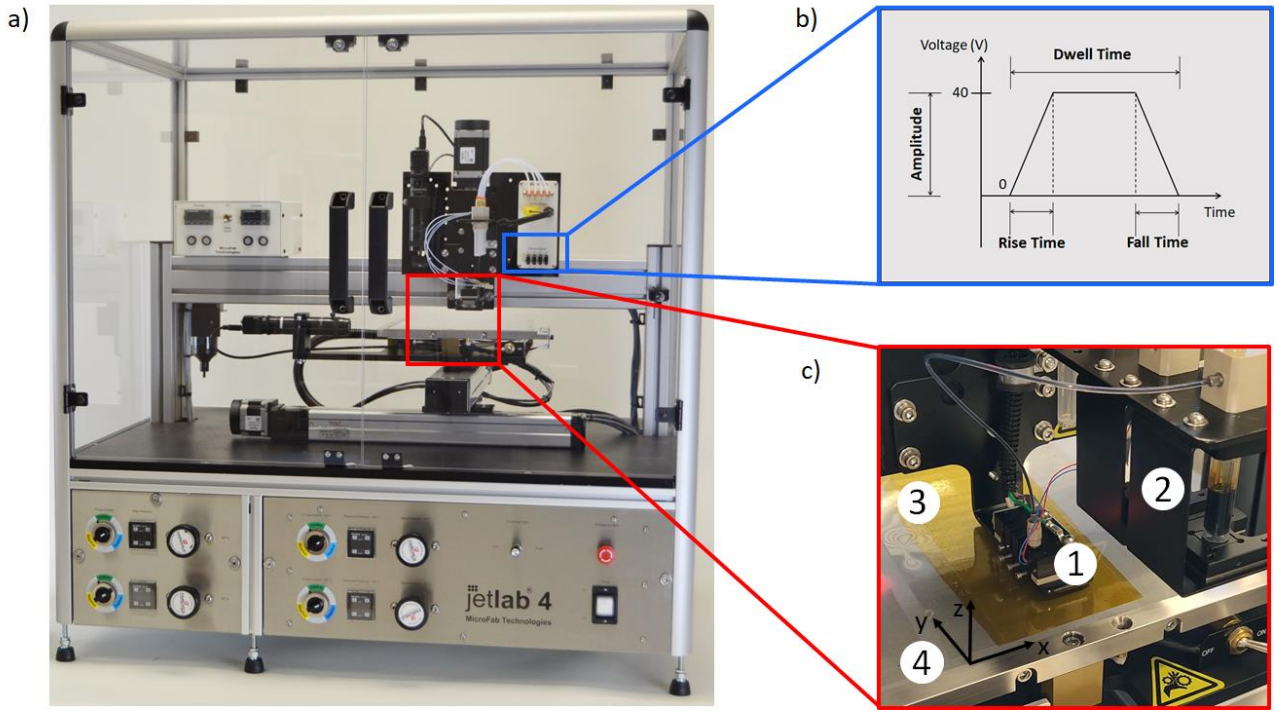

Figure 44 a) JetLab DoD inkjet printer system. b) Voltage monopolar waveform applied to the piezoelectric nozzle c) The printing plate defines the x-y plane (4), the motion of the printing head (1) defines the z-axis. (2) represents the ink cartridge. (3) is the PI printing substrate.

Silver nanoparticle-based ink by Anapro is used to deposit the electrodes. This ink has a specific resistivity of 12 μΩ·cm, a viscosity ranging from 10 to 17 cps, and surface tension from 35 to 38 mN/m. Prior to printing, the conductive ink undergoes a sonic bath (Elmasonic P by Elma) for 10 minutes at a frequency of 37 kHz at full power, to avoid particle aggregation. Then, it is filtered with a 0.45 μm PTFE filter when purged into the ink cartridge (Figure 44c). A 50 μm diameter piezoelectric glass nozzle has been used as the jetting device. The printing channel backpressure is kept at -14 Pa, compensating for gravity, obtaining flat ink meniscus at the jetting device tip. The voltage waveform was tuned by using parameters listed in Table 5 for stable droplet generation. Finally, the ink was printed onto the *PI foil*, with a printing speed of 10 mm/s, forming the target interdigitated geometry. The space between subsequent drops is set at 0.17 mm along the x-axis and 0.20 mm along the y-axis, ensuring homogeneous areas infill and straight borders. Printed electrodes are left onto the printing plate until complete dry-out, then cured in oven at 140°C for 45 minutes for silver particles sintering.

	Anapro Ag ink	Xerox dielectric ink
Voltage Amplitude	37 V	40 V
Rise Time	3 µs	3 µs
Fall Time	3 µs	3 µs
Dwell Time	33 µs	32 µs

Table 5. Waveform parameters settings for conductive Anapro Ag nanoparticle-based ink and Xerox xdi-dcs dielectric ink

A dielectric ink, the xdi-dcs by Xerox, is used to deposit the insulating layer. It has a viscosity of 8-9 cps, surface tension of 24 – 25 mN/m, a dielectric constant of 4.6 at 1kHz, and dielectric strength of around 100 MV/m. An 80 µm diameter piezoelectric glass nozzle has been used as jetting device. Printing channel backpressure is set at -4 Pa during the printing process to obtain a flat meniscus at the nozzle tip. Stable ink droplets are achieved by using waveform parameters listed in Table 5. By setting the drop spacing along the x-axis at 0.11 mm and 0.17 mm along the y-axis, with a printing speed of 10 mm/s, the dielectric ink is deposited as an infilled rectangle covering the whole electro-active area of the EAD and exceeding at the borders of 1.5 mm (Figure 45c).

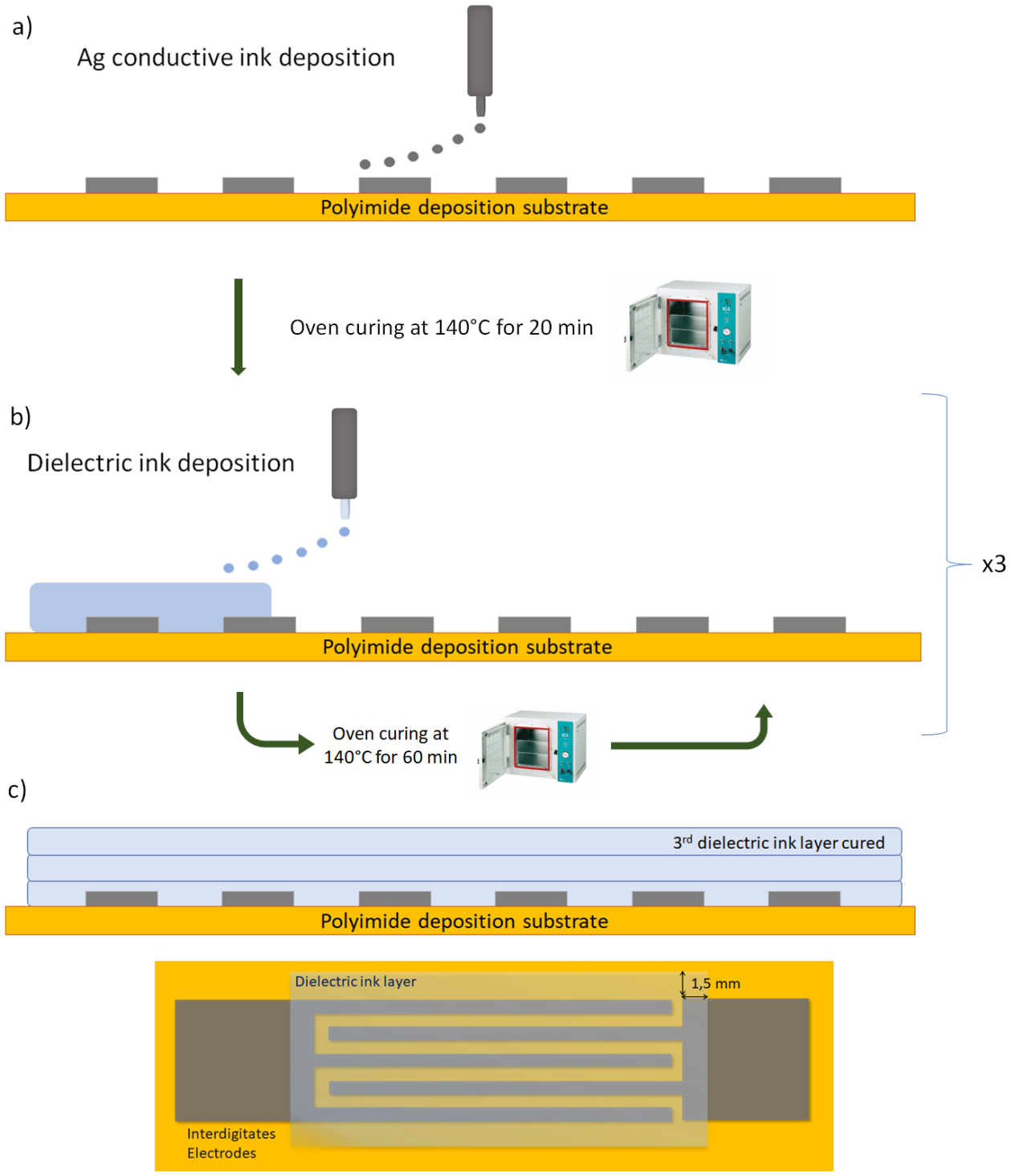

Figure 45 Dielectric ink deposition procedure: a) The electrodes are deposited and cured in oven. B) Then the first dielectric layer is printed out. c) The first dielectric layer is deposited and cured. Two more layers are deposited in the same way. c) EAD layer structure section and view from above. The ended sample is cured in oven for one hour.

Preliminary tests have been conducted to establish the minimum number of dielectric ink layers necessary to obtain a repeatable EAD outcome. So, three layers of dielectric ink are printed to ensure complete coverage of the area and repeatability of the device performance. After each layer is printed, the ink is cured in oven at 140 °C for 20 minutes (Figure 45b). At final step, the completed device is

cured in oven for one hour at 140 °C. The resulting thickness of the dielectric layer after the curing process (e.g. after evaporation of the solvent) is (10±1) µm, measured with a digital micrometer (Figure 45). The thickness of the dielectric layer is so tunable by adding layers from 10 µm, that can be considered as the lower thickness limit.

8.2.3 Testing Setup

The deployed test bench corresponds to what is proposed by Caselli et Al.[61] reported in Figure 46. The EAD is placed for the entire testing procedure on the fixed stage between two PMMA plates, shaped with a laser-cutter to leave only the active area of the EAD uncovered. The EAD is connected to a high voltage amplifier (ULTRAVOLT 20HVA24-BPL) through copper stripes interposed between the two PMMA plates. A linear guide, provided by IGUS, controlled by a DC motor (FAULHABER Series 2342 CR), represents the moving part of the test bench. A 10 kg load cell (NS-WL1-10 kg) is mounted on the slider, which also disposes of a vertical rail allowing height adjustment. A test substrate made of polyethylene terephthalate (PET), 125 µm thick, is connected on the other side of the force sensor. The testing substrate height can be adjusted to ensure the correct alignment with the EAD surface plane for proper shear force measurement. The testbench components are monitored and controlled by a CX5140-0125 Beckhoff IPC. Input/output modules control all the hardware parts: the current and voltage both provided and monitored by the power supply (CMPS, VM), the voltage and current values at the EAD (VD, CM) and the force measurements during operations with the loadcell (LC), and the motor position (DC motor). When performing a test, a relays system enables or interrupts the signal provided by the power supply and all the electronics. Figure 46b depicts the electrical connections between all the testbench hardware.

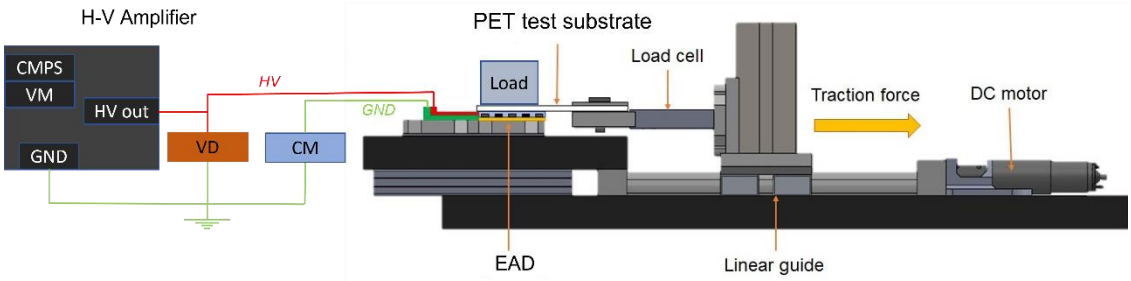

Figure 46 Testbench for ESS assessment and Breakdown results CAD schematic draw. Both Voltage and Current are monitored as signals directly from the power supply and directly from the device, with a current monitor (CM) in series to the device, and a voltage monitor (VD) parallel to the device.

8.2.4 Electroadhesive Shear Stress test

While running the test for ESS assessment, the PET substrate is positioned onto the EAD active area. As The EAD prehensive performance mostly depends on the effective contact area between the device and the object[29], a homogeneous pressure of 600 Pa is applied by placing a weight over the whole area. A DC high voltage is then applied to the EAD, and after two seconds the linear guide is moved to pull the testing substrate away from the EAD. The peak force acquired from the loadcell, corresponding to the breakaway force, is later divided by the EAD area to obtain the ESS value. With the described layout and testing procedure, the setup wants to replicate the ISO 8295 standard[24] for testing the shear forces, or frictions, between plastic thin films.

8.2.5 Breakdown testing

For EAD breakdown assessment, samples are powered with a voltage ramp having a 1kV/s slope, under continuous current and voltage monitoring. The EAD area is left uncovered during the procedure. A progressive stress test is so performed to match the standard ASTM D149[27]. When a DC current higher than 70 µA, corresponding to the 70% of the power supply maximum current, starts to flow through the EAD due to breakdown occurrence, the control unit deactivates the relays after the detection, interrupting the experiment. The voltage measurement corresponding to the test interruption is assumed to be the breakdown voltage. The breakdown assessment is also confirmed by observing the erosion of the electrodes and the damage of the dielectric layer via an optical image acquisition. As the breakdown occurrence can be considered a stochastic event, the best model suggested in literature to describe the failure probability is the Weibull distribution (WBL), successfully applied to describe the time of failure of capacitor, electric insulator and many other system. It is worthwhile to mention the two parameters, α and β, characterizing the WBL distribution. These parameters define the failure probability, the probability density function and the survival probability as, respectively,

$$F_{WBL}(u) = 1 - exp\left[-\left(\frac{u-u_0}{\alpha}\right)^{\beta}\right] \qquad (1)$$

$$f_{WBL}(u) = \left(\frac{\beta}{\alpha}\right)\left(\frac{u-u_0}{\alpha}\right)^{\beta-1} exp\left[-\left(\frac{u-u_0}{\alpha}\right)^{\beta}\right] \qquad (2)$$

$$R_{WBL}(u) = exp\left[-\left(\frac{u-u_0}{\alpha}\right)^{\beta}\right] \qquad (3)$$

where the position parameter α represent the percentile corresponding to the aleatory value with occurrence probability of 63.21% and the shape parameter β has a great importance in failure analysis,

since it is connected with the failure rate behavior of system. The rate of failure is obtained by the known *Hazard* function defined as

$$h_{WBL}(u) = \frac{f_{WBL}}{R_{WBL}} = \left(\frac{\beta}{\alpha}\right)\left(\frac{u-u_0}{\alpha}\right)^{\beta-1} \qquad (4)$$

Corresponding to the ratio between the probability of the device instantaneous failure at a generic time and its survival probability of reaching that specific time. Being correlated to β, it provides information about the behaviour of the failure event. In particular, if β≥3, the *Hazard* function increases exponentially, indicating an abrupt event. This would indicate the right voltage to be chosen as sample dielectric strength.

8.3 Results and Discussion

8.3.1 Electroadhesive shear stress results

Despite findings in the literature regarding the ESS performance of EADs having a PI layer as adhering surface[62],[23], there are no references about using inkjet-printed dielectric layer as gripping layer. Preliminary ESS tests are conducted on five EADs manufactured as outlined in Figure 39. Such preparatory experimental characterization will provide guidelines for adhesive performance assessment. Moreover, this procedure allows to define the operating voltage range of the EADs. Referring to the specimen layout and design parameters described in Figure 43, the devices have been manufactured featuring the following geometrical dimensions: g=300 µm, w=400 µm, t_{sub} =25.4 µm, t_{ins} =10 µm, W=6 mm, L=24 mm and, therefore, an active area A=144 mm^2. Figure 47 shows one explanatory EAD: the darker region, highlighted by the black rectangle, is the inkjet-printed dielectric layer, while in the background, the yellowish PI substrate can be seen. Following the testing procedure described in 7.3 , a high voltage DC step signal is applied to the EAD during ESS testing. In each test, the voltage is increased from 1kV till specimen breakdown. The obtained results are presented in Figure 48. Data in the plot are the mean values over all the five tested samples, for which each test was replicated three times. The error bars are calculated as the standard deviation.

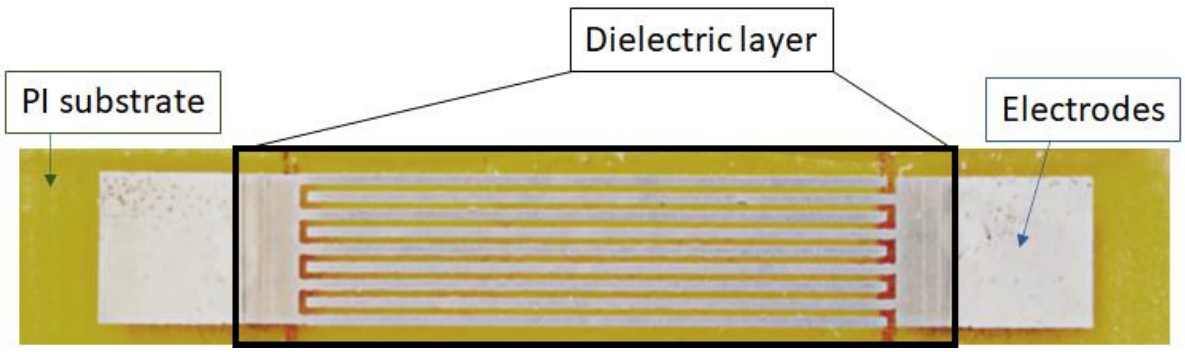

Figure 47 Optical image of an EAD produced by DoD inkjet printing

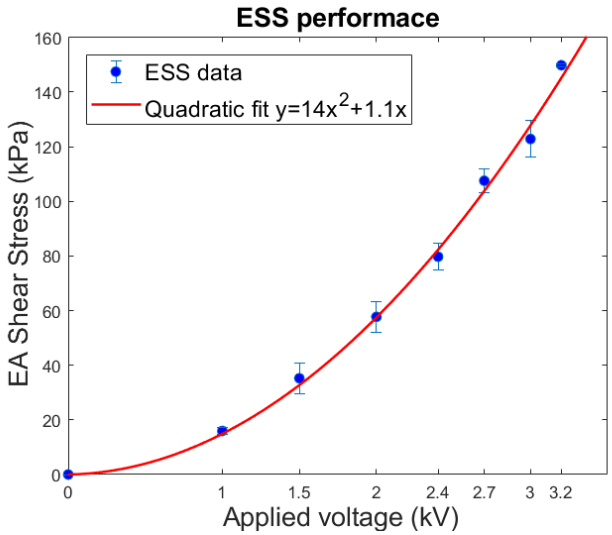

Figure 48 Preliminary ESS test to find the highest sustainable voltage value, which is found to be 3.2kV. An experiment at 0kV has been performed to evaluate the friction coefficient of the dielectric ink. The red line suggests the quadratic behaviour only for illustrative purposes.

As can be noticed, the ESS-voltage relation fits a quadratic trend within the 3.2 kV of applied voltage. Such characteristic curve, described by the illustrative red line in Figure 48, confirms what is suggested by recurring analytical models based on the Maxwell stress tensor[11], where the relation between electro-adhesive pressure, or force, and the electric field, or the applied potential, is supposed to be quadratic. For voltage values above 3.2 kV, samples exhibited the mechanical peeling of the dielectric layer from the PI substrate, with consequent electrical breakdown. As a deduction, the adhesion force between the dielectric ink and the PI layer is lower than the adhesive pressure generated by the electrostatic stress at those electric field intensities. However, as the ESS results above 100 kPa at 2.7 kV, the obtained pressure values still represent promising results concerning the EAD adhesive performance.

A more detailed experimental campaign to evaluate the ESS performances of the designed EAD concerned the manufacture and test of twenty samples. Produced EADs feature the same geometrical properties proposed before (g=300 µm, w=400 µm, t_{sub} =25.4 µm, t_{ins} =10 µm, W=6 mm, L=24 mm, A=144 mm^2). Based on what evinced from the preliminary ESS assessment, the applied voltage was limited to 3kV during ESS testing for a conservative and safe-operational procedure.

Potentially, both the dielectric faces of the EAD could be used as gripping layer. To better understand the real benefit of employing the dielectric ink layer instead of the PI substrate in ESS assessment, fifteen samples were tested employing the former as adhering surface, while the remaining five samples using the latter. The voltage is set at 1,2 and 3 kV. For each samples the traction test is repeated three times at each voltage value and the mean is considered, to ensure the

repeatability of the measure. The ESS values reported in Figure 49 are obtained by taking the mean value over all the specimens tested. Error bars represent the standard deviation. The mechanical friction between the EAD and the testing substrate was also evaluated performing a traction test at 0 Volts. At first glance, the ESS resulted much higher while grasping the PET film from the inkjet-printed dielectric ink. Indeed, the PI adhering surface provided pressure values of 46kPa at 3 kV, while the dielectric ink brought a performance enhancement of almost a factor of four. In particular, ESS values resulted equal to 159kPa at 3 kV. An appreciable contribution of the electro adhesive force can be noted by comparing 1kV ESS results with the pure friction force measured at 0 Volts, which resulted in only 0.6kPa. Every tested sample survived the testing procedure, suggesting that 3kV is within a safe operational voltage range.

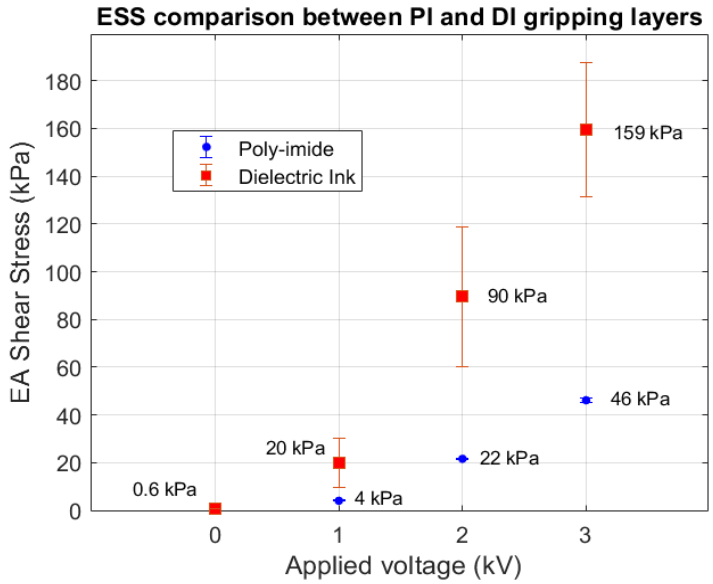

Figure 49 Electro-adhesive shear stress at breakaway. Blue dots represent the test of the PI layer and the red square the dielectric ink, both used as gripping layers. The mean over all the samples is reported for each voltage value, and errors are evaluated as the standard deviation.

8.3.2 **Breakdown Results**

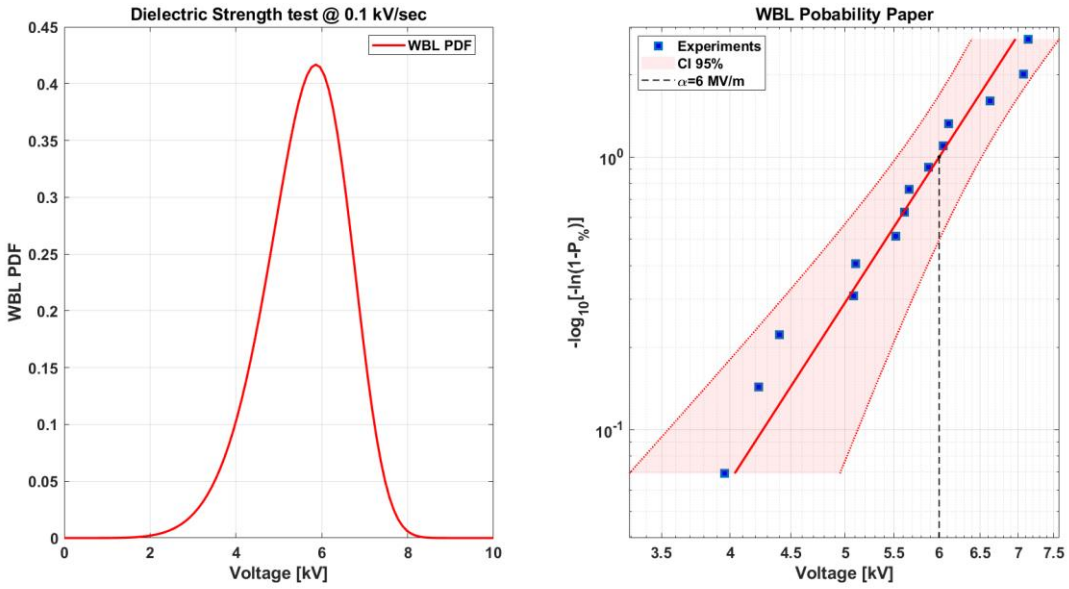

Figure 50 Weibull probability density function (WBL PDF) on the left, and probability paper on the right side representing experimental breakdown failure results of 14 samples.

With the fabrication process described before, fourteen EADs have been produced and tested following the usual procedure for breakdown voltage assessment. The devices are designed with the same geometrical dimension.

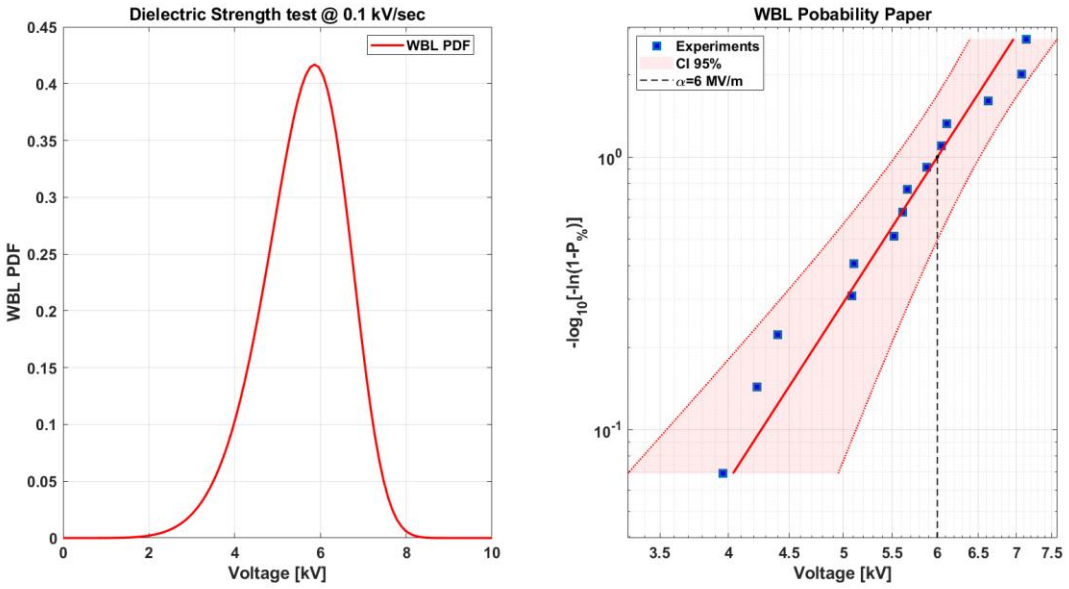

shows the Weibull distribution representing the probability of breakdown occurrence. The analysis has been done in Matlab© by performing the built-in functions *wblfit*, *wbllike* and *wblpdf*. The breakdown value found by the α parameter is 6kV. The β parameter resulted 6.7, indicating a sudden rupture event. All data lay within a 95% confidence limit, demonstrating a narrow data dispersion

and validating the repeatability of the manufacturing process. This could suggest that the EAD rupture experienced in section **Errore. L'origine riferimento non è stata trovata.**was not caused by an e lectrical discharge but a mechanical damage of the dielectric ink layer, during the traction test, compromising the structure integrity (e.g. a peeling effect). As the breakdown event occurred, every sample exhibited electrical discharge burning the electrodes and removing the dielectric layer, as shown in Figure 51.

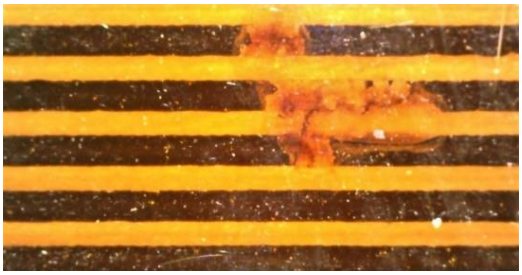

Figure 51 Optical image of the electrical breakdown occurred within two comb-fingers. The dielectric layer has been removed by the energy released.

8.3.3 EAD performance and time of production

As the last step in the proposed experimental characterization process, an analysis of the ESS performance and production time consumption was conducted by comparing EADs having different areas to investigate the scalability of the manufacturing procedure. Figure 52 presents optical images of the three proposed device sizes. Employing the manufacturing procedure proposed, two samples having an adhesive area of 480mm^2 (20mmx24mm) and 960 mm^2 (40mmx24mm) have been produced. The other design parameters are maintained at the same values as described before. As regards the ESS performance, results discussed in 8.3.1 are compared with ESS performance obtained

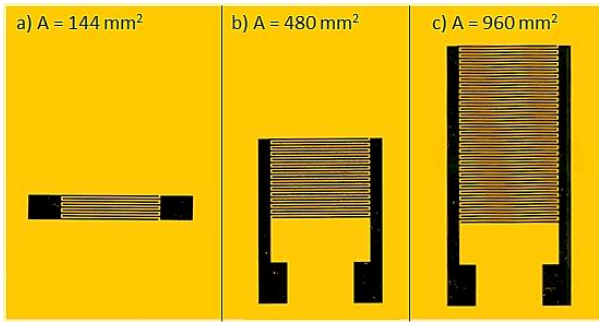

Figure 52 EADs with three different areas (L x W) for scalability evaluation. a) area of 6x24 = 144 mm2, b) area of 20x24 = 480 mm2, c) area of 40x24 = 960 mm2

by the EADs having an active adhesive area of 480mm^2 and 960 mm^2. All the samples underwent the same testing procedure described in 8.2.4 . The driving voltage was a DC step having an amplitude of 1kV, 2kV, and 3kV, for consistency with what was reported in 8.3.3 . Traction tests have been

repeated three times at each voltage value and the mean among tests was calculated. Figure 53 reports the obtained results. EAD having A=480 mm^2 provided 15 kPa at 1 kV, 82 kPa at 2 kV, and 131 kPa at 3 kV. ESS of the sample having A=960 mm^2 resulted equal to 23 kPa at 1 kV, 84 kPa at 2 kV, and 149 kPa at 3 kV, meaning an average tangential force of 143 N. Comparing the ESS values of the three EAD categories, it can be noticed that they differ for pressure values contained in the error bars of ESS generated by EADs having 144mm^2.

Moreover, consideration regarding the production time of a single or multiple devices can be done. The production time consumptions are summarized in **Errore. L'origine riferimento non è stata t rovata.**. The total time for one unit is defined as the time spent to deposit and sintering the electrodes added to the time spent to deposit each of the three dielectric ink layers and the curing process. The time for the additional unit comprehend only the deposition of the electrodes and the dielectric layers, as the same steps in the printing process for different samples are performed subsequently. These parameters are useful to understand what's the more convenient choice between producing *"small"* or *"big"* devices for a target application. From the time required to produce one single unit, it is possible to calculate the total time spent in producing a certain number of EADs necessary to achieve a desired adhesive shear force. For instance, a holding force of 130 N at 3kV can be achieved by:

- One sample having A=960 mm^2, produced in 395 minutes,
- Two EADs having A=480 mm^2, manufactured in 445 minutes,
- Six EADs having A=144 mm^2, which still require 445 minutes.

Such a feature eventually allows to target a specific electro-adhesive force by one single *"big"* EAD or by multiple *"smaller"* devices. It has to be considered that issues have been encountered during the printing of wide areas with the dielectric ink. A long-lasting and uninterrupted printing session increases the manufacturing failure rate, which is mainly caused by contaminations (dust and fibers). Previous experiments showed that half of the sample produced with A=960 mm^2 succeeded, while almost every sample produced with A=144mm^2 ended in a fine manufacture.

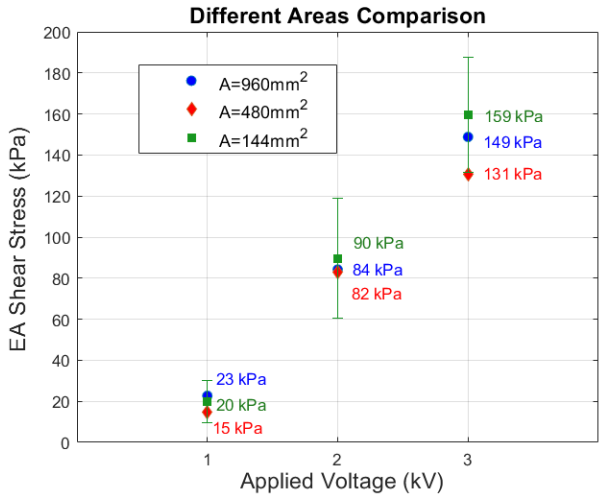

Figure 53 ESS results regarding samples of three different areas: 144 mm² (green squares), 480 mm² (red rhombuses), 960 mm² (blue dots).

EAD Area (mm²)	Production time (mins.)	
	Total time for one unit	Additional unit
144	**195**	**50**
480	**295**	**150**
960	**395**	**250**

Table 6 Production time of the EAD with the three different areas. The production time represents the total time for one sample and the time to be added for any other unit to be manufactured.

8.3.4 Discussion and further improvements

The sample produced by DoD inkjet printing technique revealed a great potential in electro-adhesive shear stress performances. During ESS tests, the adhering layer of an EAD is subjected to high mechanical stress leading to the maximum holding tangential force sustainable before the brake of the structure occurs. Indeed, EADs experienced a mechanical rupture which caused the electrical breakdown due to the removal of the inkjet-printed insulating layer. Adhesion improvement between the PI layer and the dielectric ink through surface treatments, like surface plasma exposure prior to layer deposition, is scheduled as future work. However, there are no guarantees that increasing interface adhesion will be enough to increase the mechanical resistance of the device. Further study on the mechanical properties of the dielectric ink should be done to understand the applicability limits.

As the manufacturing environment impacts on the quality of the printing results, proceeding in a controlled environment (e.g. clean room) with proper facilities might increase productivity as well as device performance. Considering the scalability of the results, to create a complex EAD could be made easier by considering to link modules composed by smaller devices. This would prevent the brake of a single, large area device due to small defects.

This chapter proposed a class of Electro-adhesive devices (EADs) fully printed with Drop on Demand inkjet printing technology. Printing the electrodes and the insulation layer onto an industrially produced Polyimide foil and using the dielectric ink insulation layer as grasping surface, the devices reached 159 kPa of electro adhesive shear stress (ESS) powered at 3 kV, which resulted the highest ESS value in the literature. The experimental campaign demonstrated a quadratic trend of the ESS-Voltage characteristic curve confirming the recurring analytical models describing the electro-adhesion phenomenon. The main advantage of deploying DoD inkjet is the possibility of manufacturing tunable thickness, with an inferior limit of 10 µm, and ad-hoc-designed shapes by choosing inks with good electrical characteristics, allowing the production of lightweight and flexible EADs able to exert adhesive tangential forces of around 23 N, at 3 kV of applied voltage, with an adhesive area of only 144 mm^2.

An experimental campaign for breakdown voltage assessment defined an average breakdown voltage of 5.8kV. However, EAD rupture took place at 3.2kV during traction tests. This result indicates that mechanical solicitations with abrupt or violent dynamics, like breakaway forces, corrupt the inkjet-printed dielectric layer. Therefore, applications where EADs must block an object, thus not admitting any sliding in the contact surface, are more indicated for such actuators.

As the scalability of the adhesive performance and the manufacturing process has been confirmed, to target a specific adhesive forces is possible by different strategies: distributing multiple EAD units could prevent the total failure of the device, or concentrating the force in a unique wider device. Such a feature, together with the high flexibility of the manufacturing process, which includes geometry design and deployed materials, along with moderate powering signal amplitude requirements, make this class of actuators easy-to-integrate into hosting structures. The proposed EAD, therefore, represent a high force-size ratio and highly-integrable promising solution for object manipulation in the industry and robotic field.

Chapter 9. Empiric study of electrodes geometry design and its impact on EA performances

9.1 Introduction

The effect of electrode geometry on the electroadhesive grip efficiency on a target substrate is challenging to understand. In the literature, many results from predictive theoretical models have been presented, but they often appear to be specific to the particular case under consideration and challenging to apply to other scenarios. This led to the conduction of a study, as part of an external project, to identify the electrode geometry and the best material for composing an EAD to achieve optimal performance in terms of electrostatic shear adhesion on a poly-laminated cardboard. The study involves producing samples of the same material, in this case, PI, to compare with our laboratory's standard as presented in previous works, by varying the gap and electrode width. Once the best geometry was identified, samples of five different materials were produced to determine which material yielded the best results.

9.2 Geometry study

As the first phase of work, samples were produced using the same manufacturing process described in detail in 7.3 EADs were created with the same electroactive area LxW=15 x 24 mm^2, but by varying two key parameters, the electrode width (w) and the gap value (g). Polyimide (PI) was employed as the gripping substrate onto which the electrodes were deposited, as described in Chapter 7. A layer of PDMS was deposited as an insulator for the electrodes, through blade casting after plasma surface treatment and silicone primer application. The setup used to test the electrostatic shear adhesion, or more precisely, the Electrostatic Shear Stress (ESS), is described in 2.2 and it consists of a fixed stage on which the sample is mounted, clamped between two PMMA plates and powered. The test substrate, a poly-laminated cardboard made of Polyethylene Terephthalate (PET) and aluminum, is

attached to a load cell mounted on a support capable of movement via a DC motor on a linear guide. By powering the EAD and pulling the test substrate, the peak force of initial detachment is recorded. By dividing this force by the electroactive area, the ESS value at that voltage is obtained.

The samples produced in this initial phase can be categorized into two groups: constant electrode width (w) or constant gap (g). In the first category, the gap was set at 300, 450, and 600 µm, while the width was fixed at w=400 based on preliminary experiments. In the second category, the gap was fixed at 400 µm, and the width was varied between 1200, 2400, and 7300 µm. The final value was determined by setting two electrodes within the electroactive area.

9.2.1 Gap Influence

The samples were then tested by applying an initial pre-load of 1.8 kPa to ensure good adhesion between the surfaces of the two objects, given that the test material was not very flexible. Four samples were measured for each geometry. Six different voltage values were applied, both DC and square wave, bipolar AC, and the results are presented as ESS as a function of voltage. A test at 0 kV indicates the effect of only mechanical friction.

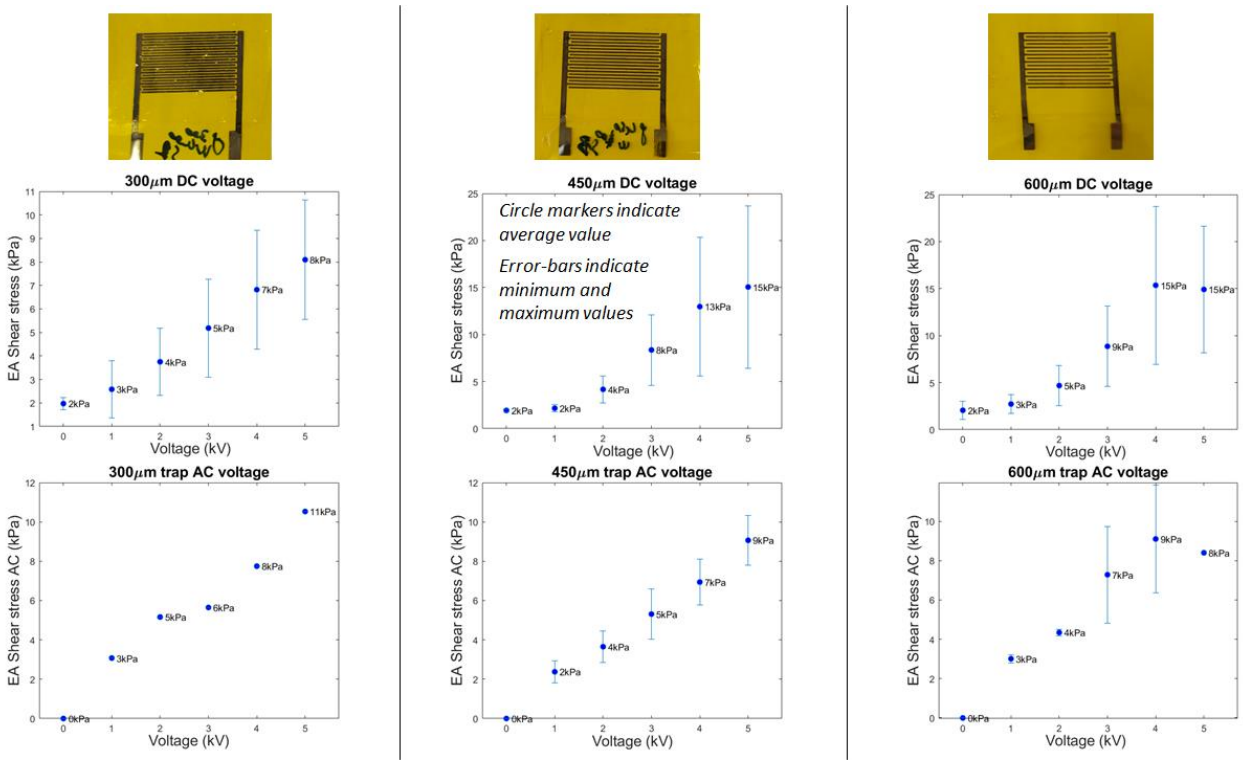

Figure 54 Different gap - EAD of PI - DC and AC ESS evaluation

The results indicate that smaller gaps result in weaker forces due to the high-intensity electric field lines being unable to penetrate the grasped object. On the other hand, increasing the gap excessively doesn't provide significant benefits, as it reduces the intensity of all electric field lines. In terms of

electrical activation, DC activation performs slightly better than AC activation at a 2.5 Hz frequency. However, there is a notable variation in performance across specimens with nominally identical geometry tested under the same conditions for both DC and AC activation. This variability may be attributed to manufacturing factors such as film thickness tolerances, surface properties, and positioning errors in the ink-jet printing process. Based on these results, a gap size of 400 µm has been identified as a promising compromise for future investigations.

9.2.2 Electrodes width influence

We also conducted a second investigation focusing on how electrode width (w) impacts grasping performance. These included configurations like g = 400 µm, w = 400 , 1200, 2400 and 7300 µm. . Four samples were measured for each geometry. Six different voltage values were applied, both DC and square wave, bipolar AC, and the results are presented as ESS as a function of voltage. A test at 0 kV indicates the effect of only mechanical friction.

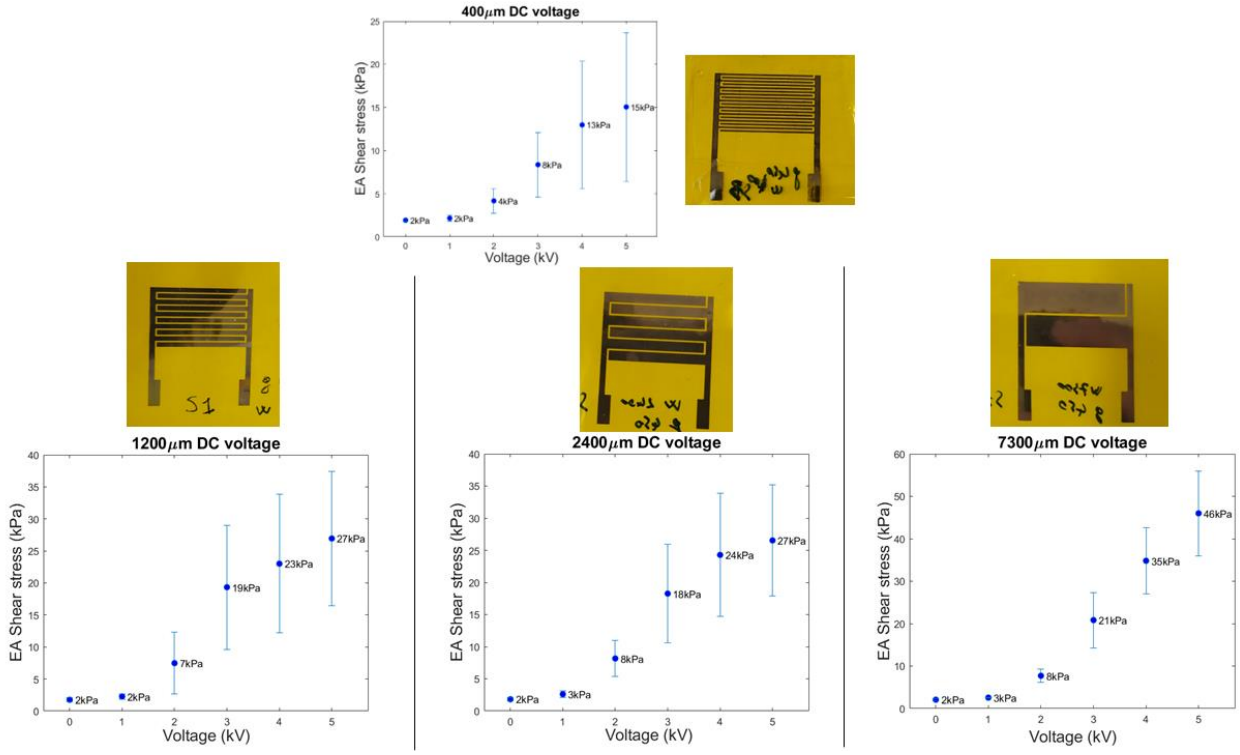

Figure 55 Different Width - DC voltage ESS evaluation

The results, reveal that increasing the width leads to higher grasping forces. However, what's interesting is the significant variability in performance we observed among specimens with nominally identical geometry tested under the same conditions. We suspect that manufacturing-related factors like film thickness tolerances, surface properties, and ink-jet printing machine positioning errors might be contributing to this variability. As a result of these findings, we have decided to proceed with a width of g = 7300 µm for our subsequent investigations.

9.2.3 **Material influence**

Having established an optimal electrode geometry (g = 400 µm, w = 7300 µm), our next investigation centered on examining the influence of EAD material, specifically the layer in contact with the testing material, on grasping performance. We considered specimens composed of five different materials, all sharing the same electrode geometry (g = 400 µm, w = 7300 µm). These materials included PI (Polyimide) with a film thickness of 25 µm (4 identical specimens), PEEK (Polyether ether ketone) with a film thickness of 23 µm (4 identical specimens), PET (Polyethylene terephthalate) with a film thickness of 25 µm (4 identical specimens), PEN (Polyethylene naphthalate) with a film thickness of 8 µm (4 identical specimens), and PET (Polyethylene terephthalate) with a film thickness of 4.5 µm (4 identical specimens). All 20 specimens underwent testing, which involved applying a 1.8 kPa pre-load and subjecting them to six different levels of DC voltage.

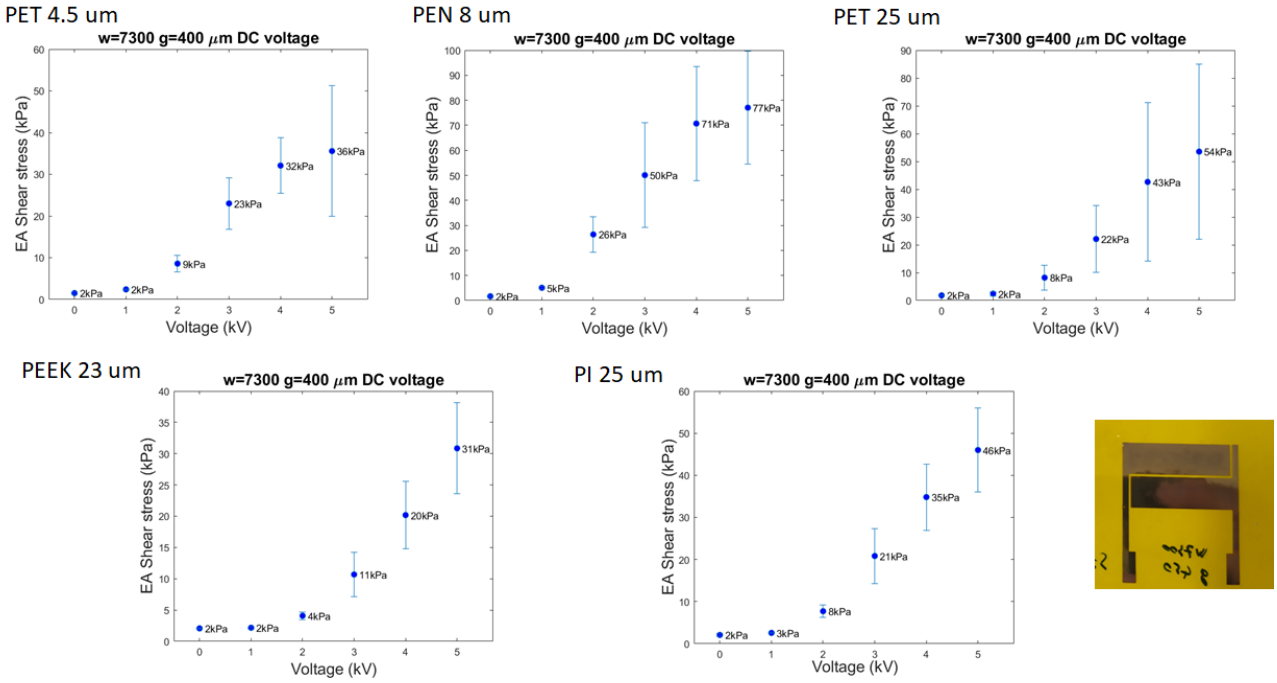

Figure 56 Different materials under test, 2 electrodes configuration - ESS evaluation with DC voltage

Irrespective of the material used, it is possible to achieve a minimum adhesive shear stress higher than 20 kPa. Furthermore, some materials allowed for an average adhesive shear stress of around 70 kPa, with the maximum value reaching up to 100 kPa.

9.2.4 Directional Influence

The tests conducted thus far have primarily focused on the shear action applied in the direction normal to the electrode lines (as indicated by the red arrow in the figure).

To investigate the influence of directionality, we subjected one EAD specimen (PEN with a film thickness of 8 µm, featuring g = 400 µm and w = 7300 µm electrodes) to testing. These tests involved varying levels of DC voltage and a 1.8 kPa pre-load, but with the shear action applied in the direction parallel to the electrode lines.

The adhesive shear stresses obtained from this configuration were then compared to those already obtained for the same specimen when subjected to a load applied in the normal direction. The results, indicate that the direction of the applied load has a limited influence on the EAD's grasping performance.

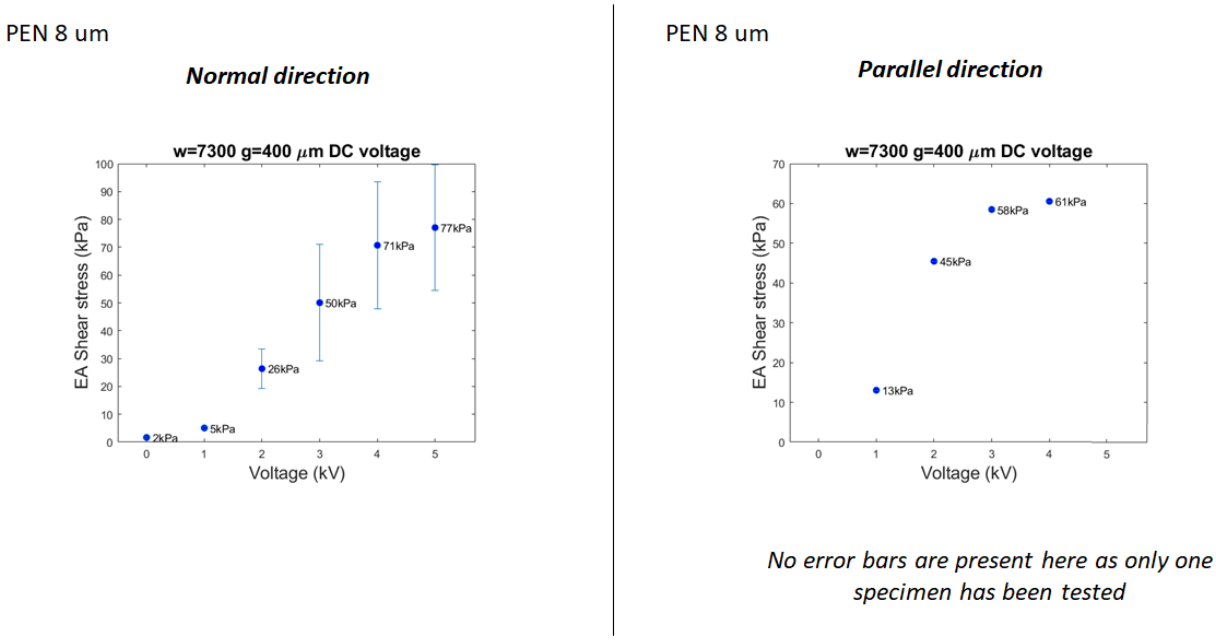

Figure 57 Comparison between the pulling direction of the testing substrate with respect to the longest gap line

The tests conducted thus far involved EAD electrical activation being applied after the contact between the testing substrate and EAD. In order to evaluate the impact of the timing of EAD electrical activation, we also tested one EAD specimen (PEN with a film thickness of 8 µm, equipped with g = 400 µm and w = 7300 µm electrodes). These tests were performed at various levels of DC voltage and with a 1.8 kPa pre-load, but with the EAD being activated before coming into contact with the testing material. The adhesive shear stresses obtained from this configuration were then compared to those already obtained for the same specimen when subjected to activation only after contact with the

testing material. The results, presented below, reveal the following: There is a significant decrease in performance when the EAD is activated before contacting the testing material. However, this action is still sufficient and, if necessary, can be improved by activating the EAD with a bipolar square wave (BPSW) voltage signal.

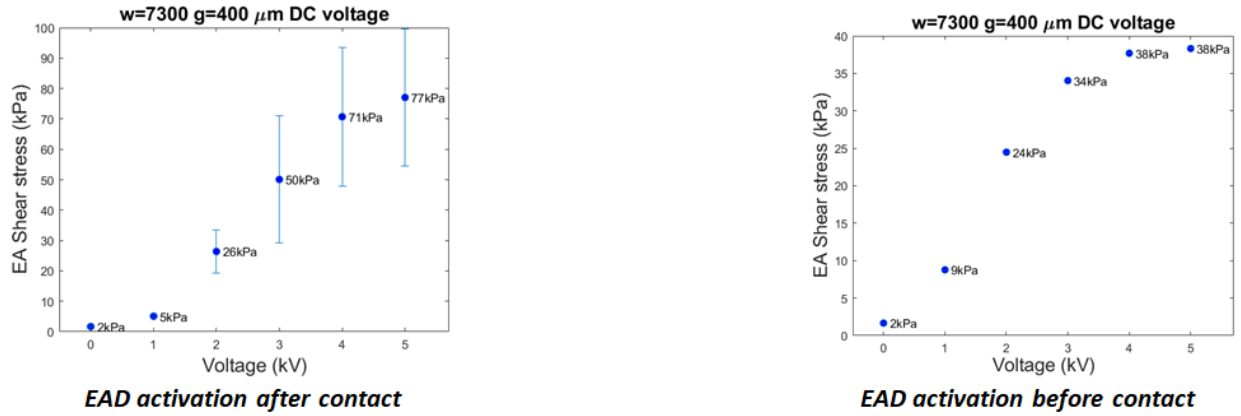

Figure 58 Evaluation of ESS performance activating the EAD before and after the contact with the testing substrate

The previous tests mainly employed DC electrical activation for our EAD specimens. To understand how the form of electrical activation affects grasping performance, we conducted tests on four EAD specimens made from different materials (25 µm PET, 8 µm PEN, 25 µm PI, and 23 µm PEEK). These specimens all had the same electrode geometry (g = 400 µm and w = 7300 µm) and were tested using 4 kV amplitude bipolar square wave (BPSW) signals at various frequencies, all while maintaining a 1.8 kPa pre-load. The results, revealed a few key findings:

- Different substrate materials exhibited distinct behaviors.

- Performance saw a significant decline beyond a specific frequency, with the exact frequency dependence varying by material.

- The relationship between EAD response and frequency, especially across different materials, warrants further in-depth investigations.

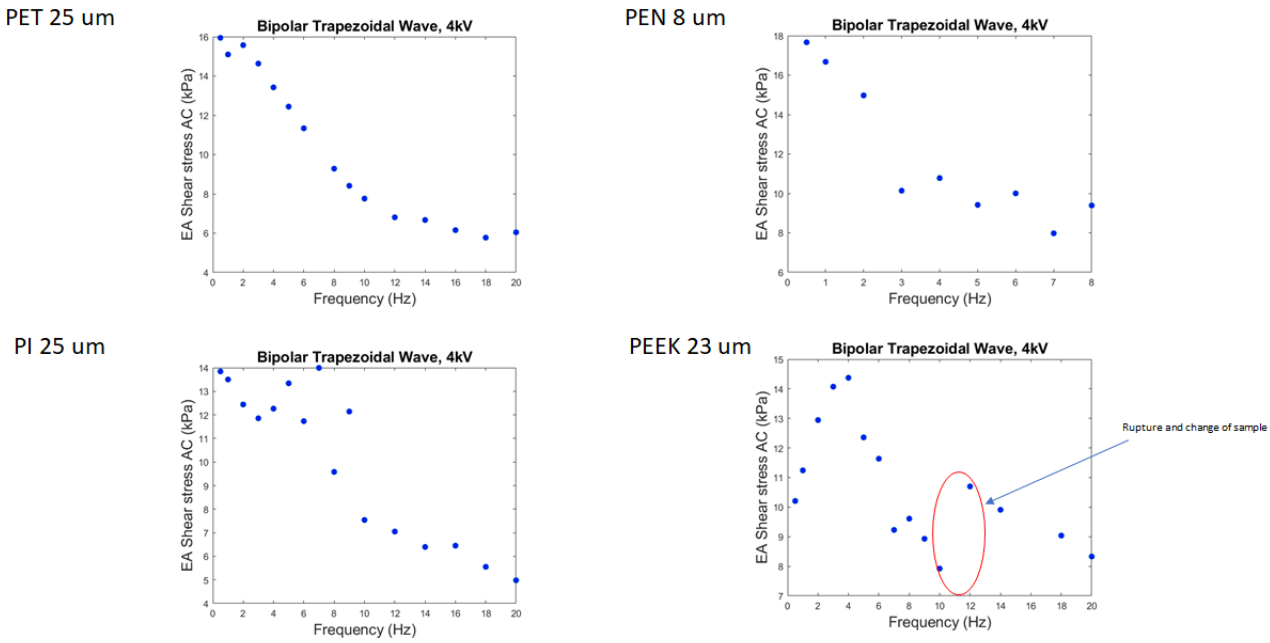

Figure 59 Frequency scan at 4kV to understand its influence on ESS performance

9.3 2nd characterization study

The initial study on electroadhesive performance concerning the laminated material has led to valuable conclusions on various aspects: the optimal geometry, the direction in which the material should be pulled relative to the gap direction, the response of different materials with similar dielectric characteristics, and the waveform and frequency used to power the EAD. It provided a solid foundation upon which to construct a more extensive experimental campaign, involving various new materials for comparison while focusing on a few specific geometries. Given that the gap width does not seem to significantly influence the device's performance in this application, the decision was made to solely vary the electrode thickness.

So, a second characterization study was conducted to evaluate the performance of different Electroadhesive (EAD) specimens. A total of four samples were prepared for each type, and all specimens shared an active area of approximately 15 x 24 mm². These specimens were fabricated using various dielectric films, including PEEK (23 µm thickness), Mylar (25 µm thickness), PI (25 µm thickness), PI (12 µm thickness), PET (12 µm thickness), and PEN (8 µm thickness). For each dielectric film, we considered multiple electrode geometries:

1. Gap: 400 µm, Width: 400 µm
2. Gap: 400 µm, Width: 1000 µm
3. Gap: 400 µm, Width: 7300 µm

Each EAD sample underwent testing using our described setup. The testing conditions included varying normal pre-loads:

- 1.8 kPa

- 4.5 kPa

- 6.5 kPa

- 8.5 kPa

Furthermore, we examined different types of electrical activation methods:

- DC: In this case, we used single steps at six equally spaced voltage levels, up to 70% of the EAD specimen's breakdown voltage.

- AC: We employed bipolar square waves (BPSW) at ten equally-spaced frequencies, reaching up to 10 Hz. The voltage level selected was approximately 35% of the tested EAD specimen's breakdown voltage.

Throughout the experiments, various parameters were monitored. These included tangential stress on the packaging material, which was used to assess prehension capability. We also measured EAD voltage and current to evaluate energy consumption and determined electrical capacitance to understand electrical requirements and their dependency on the testing material position. The results of our investigation are presented in the following sections.

The considered dielectric films have been selected as they are among the best polymer dielectrics that are available on the market in the form of thin films_

1) PEEK 23 um: RS Pro PEEK Thermal Insulating Film RS Stock No: 764-8719

Not specifically designed for dielectric applications. It is commercialized for thermal insulation, but also offers good electrical insulation properties and resistance to chemicals, abrasion and impact. Its quality is limited: the film presents scratches and wrinkles that may limit performance and repeatability. A commercial PEEK film specifically developed for dielectric applications is Victrex Aptive, which was not available and could be considered for next investigations.

2) Mylar 25 um: DuPont Mylar A

A Polyethylene terephthalate (PET) film specifically designed for dielectric applications (also for electrical capacitors). Its quality is high.

3) PI 25 um and 12 um: Caplinq PIT1N and Caplinq PIT0.5N

Not specifically designed for dielectric applications. They are commercialized for thermal insulation, but also offer good electrical insulation properties. Their quality is limited: the films present wrinkles that may limit performance and repeatability. A commercial film specifically developed for dielectric applications is DuPont Kapton, which was not available and could be considered for next investigations.

4) PET 12 um: Moretti S.r.l. ISOLANTE POLIESTERE MM 0,012

A PET film specifically designed for generic insulation applications (but not for electrical capacitors). Its quality is good but not as high as that of Mylar, which was not available at 12 um thickness and could be considered for next investigations.

5) PEN 8 um: PolyK Technologies LLC PEN-8.0um

A Polyethylene naphthalate (PEN) film specifically designed for dielectric applications (also for electrical capacitors). Its quality is high.

A comparison table is shown below (Table 7) that enables to choose the material based on the most important requirements (electrical, mechanical, sustainability) of the application.

	PEEK (e.g. Aptive by Victrex)	PI (e.g. Kapton by DuPont)	PEN (e.g. Kaladex and Teonex by DuPont)	PET (e.g. Mylar A by DuPont)
Dielectric Properties	Good	Very Good	Excellent	Excellent
Mechanical Properties @ 23°C	Good	Very Good	Very Good	Very Good
Mechanical Properties @ 150°C	Very Good	Very Good	Fair	Poor
Folding endurance	Excellent	Very Good	Fair	Poor
Abrasion / Wear resistance (*)	Excellent	Good	-	-
Recyclable	YES	NO	YES	YES
Cost	High	Very High	Fair	Low
(*) tests are required to confirm this property				

Table 7 Intuitive comparison between materials studied

9.3.1 Geometry

The three electrode geometries considered for the tests are schematized in the figures below.

For all of them, the gap size between the interdigitated electrodes is g = 400 um. This size has been chosen since it was found to be the best choice during the 1st characterization results .

The three geometries have a similar active EAD area and differ for the width of electrode lines:

- w = 400 um has been chosen to have a width equal to the gap, which is a typical choice found in the literature (this provides 10 pairs of electrode lines)

- w = 7300 um has been chosen since it is the configuration with the minimum number of electrode lines (namely, a single pair of electrode lines), thereby providing the highest coverage of the active EAD area with electrodes.
- w = 1000 um has been chosen as an intermediate geometry (this provides 5 pairs of electrode lines).

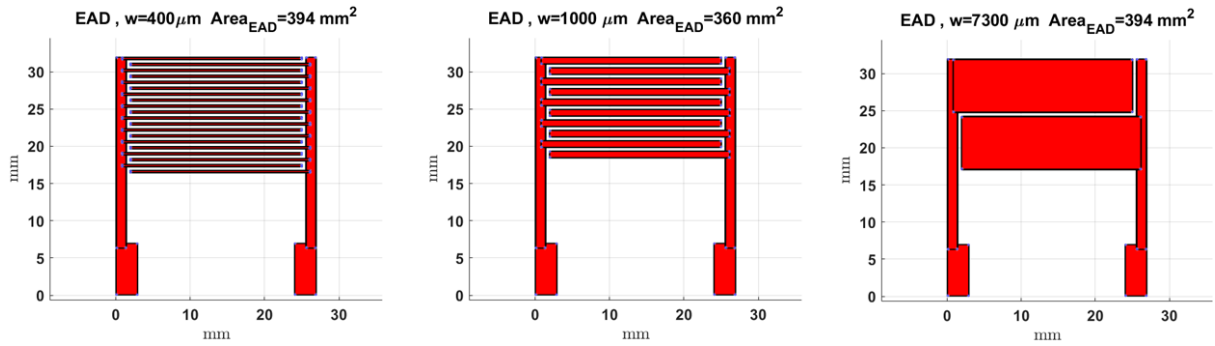

Figure 60 Geometries chosen for second experimental campaign

Testing of all the 72 manufactured EAD specimens has been performed with the same shear-stress test-bench described in 7.3 . Each of the 72 specimens has been tested with the following 4 different normal pressures (realized with loads of different weights as depicted in the schematic): 1.8 kPa this is a minimum value to prevent lack of adhesion between the two surfaces, 4.5 kPa , 6.5, 8.5 kPa

Results

Following data acquisition, the shear force, voltage, and current data obtained during the tests are subjected to further analysis to derive the specific parameters presented in the subsequent sections:

1. Friction Shear Stress: This value is computed by dividing the shear force measured at zero activation voltage by the active EAD area. For each EAD material, the Friction Shear Stress is plotted as a function of applied normal pressure. Different lines are used to represent each EAD geometry.
2. EAD Shear Stress: The EAD Shear Stress is determined by dividing the shear force measured during various activation states (both AC and DC) by the active EAD area. For each combination of EAD material and geometry, EAD Shear Stress is depicted as follows:
    a. For AC tests: It is shown as a function of frequency, with separate lines indicating different normal pressure values.
    b. For DC tests: It is presented as a function of voltage, with distinct lines representing varying normal pressure values.

3. EAD Shear Stress: To isolate the electrical contribution in the grasping action, supplementary plots are provided, displaying the EAD Shear Stress minus the Friction Shear Stress for the DC tests. EAD Shear Stress is presented as follows:
    c. As a function of voltage, with separate lines for each normal pressure value.
    d. As a function of normal pressure, with distinct lines representing different voltage values.
4. Activation Energy: This metric quantifies the energy necessary for the EAD to achieve full electrification, indicating the time when the EAD current stabilizes after the asymptotic decay caused by dielectric relaxation and the sweep of mobile ions toward the electrodes. The calculation involves determining the integral of the power delivered to the EAD from the moment the voltage command is initiated until the current has decayed to less than 5% of its peak.
5. Mean Power: This figure represents the power consumed by the EAD to maintain the grasping action. The mean power is computed between the time after the full electrification process is complete and the moment just before the application of the shear. This power is associated with the leakage of current resulting from the finite volume resistivity of the EAD materials in use.

Figure 61 shows Friction shear stress results. Each plot reports the response of three specimens made with the same dielectric films but with the three different electrode geometries (w = 400 um, w = 1000 um and w = 7300 um).

Linear interpolation of the results reported in the plots below provides the following friction coefficients:

- Mylar 25 um: 1.09 for w = 400, 1.123 for w = 1000, 1.192 for w = 7300 um; 1.135 mean (0.052 std)
- PEEK 23 um: 1.47 for w = 400, 1.198 for w = 1000, 1.219 for w = 7300 um; 1.295 mean (0.151 std)
- PI 25 um: 1.645 for w = 400, 1.167 for w = 1000, 1.177 for w = 7300 um; 1.329 mean (0.273 std)
- PET 12 um: 1.053 for w = 400, 0.8432 for w = 1000, 1.37 for w = 7300 um; 1.088 mean (0.265 std)
- PEN 8 um: 1.139 for w = 400, 1.139 for w = 1000, 1.137 for w = 7300 um; 1.138 mean (0.012 std)

- PI 12 um: 0.8 for w = 400, 0.847 for w = 1000, 1.105 for w = 7300 um; 0.917 (0.1642 std)

Overall:

- Mylar 25 um and PEN 8 um exhibit the most repeatable response, which confirms the good quality of these films.
- The other materials exhibit non-negligible different responses for different electrode geometries, indicating that these films have friction properties that vary along their surface. This confirms the limited quality of these films.

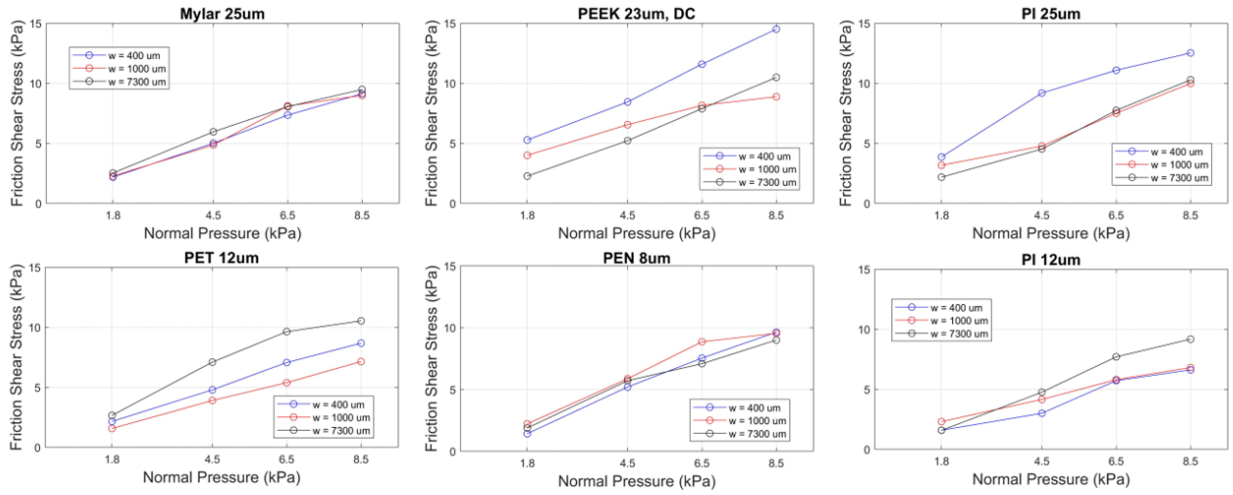

Figure 61 Friction test results

9.3.2 AC tests

To explore the influence of frequency on the shear stress developed by the EAD, we initiated our investigation with AC tests. Specifically, we conducted a series of tests on each of the 72 fabricated EAD specimens for four distinct normal pressure values: 1.8 kPa, 4.5 kPa, 6.5 kPa, and 8.5 kPa. For each of the 72 EAD specimens, we executed tests using bipolar square wave (BPSW). These tests were conducted at a singular voltage level, equal to 35% of the EAD specimen's breakdown voltage, which had been determined through breakdown tests on separate EAD specimens for each material and electrode geometry case. To capture the full frequency spectrum, we conducted tests at 11 different equally spaced frequencies, ranging from 0 Hz (DC tests) up to 10 Hz. The selected voltage level was chosen to minimize the effects of power supply saturation on EAD specimen activation, especially at higher frequencies. Nevertheless, it still ensured a sufficient shear stress produced by the EAD. The outcomes of these tests are presented across six plots depicting EAD shear stress as a

function of frequency. Specifically, there is a result for each material (Mylar 25 um, PEEK 23 um, PI 25 um, PET 12 um, PEN 8 um, and PI 12 um). Within each result figure, there is a distinct plot for each electrode geometry (w = 400 um, w = 1000 um, and w = 7300 um). Each plot is color-coded to represent different normal pressure values (1.8 kPa, 4.5 kPa, 6.5 kPa, and 8.5 kPa). In the plots, the circle markers denote mean values obtained from sixteen trials, which include four tests conducted under identical electrical and normal pressure conditions for each of the four nominally identical EAD specimens produced with the same material and geometry. Additionally, error bars are displayed alongside the circle markers to visualize the data's variability across the sixteen trials.

Mylar

The graphs in Figure 62 presents the outcomes of the AC tests performed on specimens constructed with a 25 μm thick Mylar dielectric film. The key observations from the results are as follows:

1. The error bars in the plots are notably small, underscoring the high-quality performance of the 25 μm thick Mylar dielectric film. This level of quality aligns with the findings from the friction results presented before.
2. Irrespective of the electrode case, the highest shear stress is consistently achieved under DC activation conditions. This implies that DC activation is more effective in generating shear stress than AC activation for all electrode configurations.
3. The shear stress exhibits a subtle and gradual decrease with increasing frequency, a trend that is particularly evident for the electrode configuration w = 7300 μm and in scenarios involving lower normal pressure conditions. This observation suggests that higher frequencies tend to reduce the shear stress produced by the EAD, with the effect being more pronounced for specific electrode geometries and lighter normal pressures.
4. At each frequency and electrode configuration, the EAD shear stress is consistently greater when the normal pressure is increased. This correlation aligns with the relationship between normal pressure and shear stress resulting from friction. In other words, higher normal pressure values are associated with increased shear stress, highlighting the direct link between these two parameters.

These findings shed light on the behavior of EAD specimens constructed with a 25 μm thick Mylar dielectric film when subjected to AC tests, revealing valuable insights into the impact of frequency, electrode geometry, and normal pressure on shear stress generation.

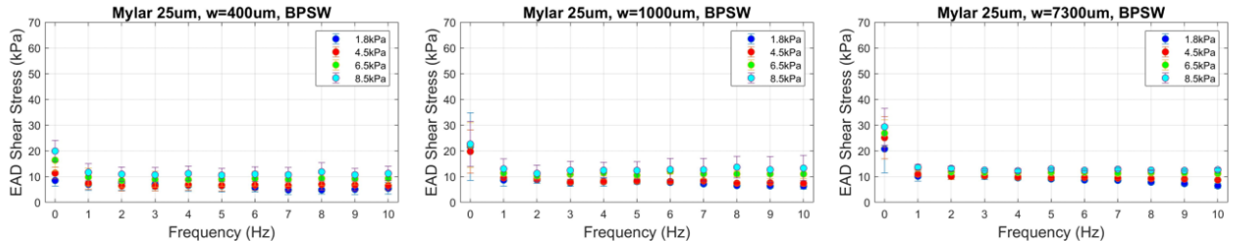

Figure 62 AC results for Mylar

Polyimide

The graphs in Figure 63 represent the outcomes of the AC tests carried out on specimens with a 25 μm thick PI dielectric film. The key observations from the results are as follows:

1. Notably, the error bars for the cases with lower applied normal pressure are significant. This finding underlines the limited quality of the 25 μm thick PI dielectric film used, which is consistent with the findings from the friction results. The larger error bars suggest a higher degree of variability in the data for these conditions.
2. For all electrode configurations, the highest shear stress is consistently achieved under DC activation conditions. This indicates that, regardless of electrode geometry, DC activation outperforms AC activation in terms of shear stress generation.
3. The shear stress experiences a mild, nearly monotonic decrease with increasing frequency across all electrode cases, particularly in scenarios involving lower normal pressure conditions. However, it's important to note that this trend is influenced by the variability of the data mentioned in point (1).
4. In general, the EAD shear stress tends to be higher at higher normal pressure values for each frequency and electrode configuration. This aligns with the expected relationship between normal pressure and shear stress as seen in friction. Any discrepancies from this general trend can be attributed to the variability in the data highlighted in point.

These findings provide insights into the performance of specimens with a 25 μm thick PI dielectric film during AC tests, highlighting the influence of frequency, electrode geometry, and normal pressure on shear stress. The presence of variability in the data, especially in cases with lower normal pressure, emphasizes the importance of material quality in EAD performance.

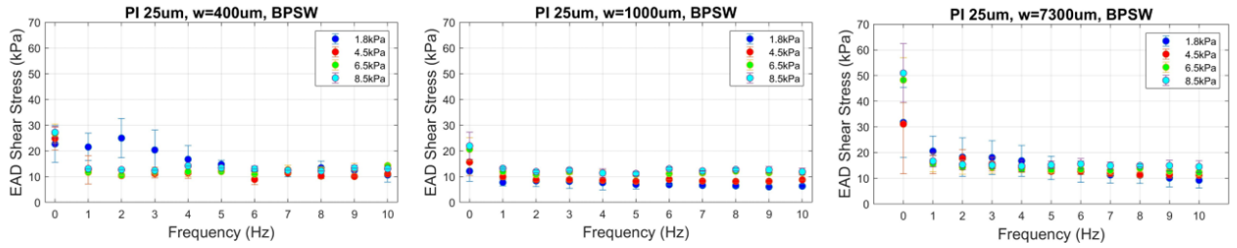

Figure 63 AC Results for Polyimide

PEEK

The graphs in Figure 64 represent the results of the AC tests conducted on specimens using a 23 µm thick PEEK dielectric film. The key observations from the results are as follows:

1. The error bars for all normal pressure cases are relatively large. This indicates that the employed 23 µm thick PEEK dielectric film's quality is limited, a finding consistent with the friction results. The presence of larger error bars suggests increased variability in the data for these conditions.
2. Similar to previous cases, the highest shear stress is consistently achieved under DC activation conditions for all electrode configurations. This confirms that DC activation outperforms AC activation in terms of shear stress generation, regardless of electrode geometry.
3. The shear stress shows a mild, nearly monotonic decrease with increasing frequency across all electrode cases. This trend is clearer for the electrode cases w = 400 µm and w = 7300 µm, particularly in scenarios with lower normal pressure conditions. However, the data for the w = 1000 µm case is challenging to interpret due to the highlighted variability.
4. In general, the EAD shear stress tends to be higher at higher normal pressure values for each frequency and electrode configuration. This aligns with the anticipated relationship between normal pressure and shear stress, as observed in the friction results. Any deviations from this general trend can be attributed to the variability in the data.

These findings provide insights into the performance of specimens with a 23 µm thick PEEK dielectric film during AC tests, highlighting the effects of frequency, electrode geometry, and normal pressure on shear stress. The presence of data variability, especially in cases with lower normal pressure, underscores the importance of material quality in EAD performance.

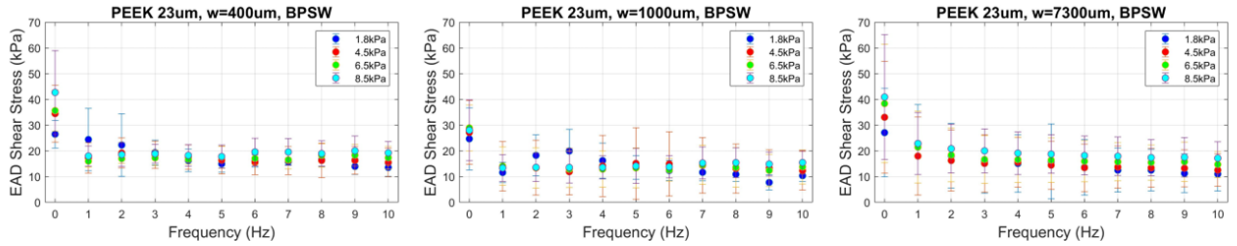

Figure 64 AC results for PEEK

PET

The graphs in Figure 65 represent the results of the AC tests conducted on specimens using a 12 µm thick PET dielectric film. The key findings from these results are as follows:

1. Error bars are relatively small, indicating that the AC results for this material are minimally affected by the limited quality of the employed 12 µm thick PET dielectric film. This contrasts with earlier findings where the quality of the dielectric film significantly influenced the results in the friction tests.
2. Similar to previous cases, the highest shear stress is consistently achieved under DC activation conditions for all electrode configurations. This reiterates that DC activation outperforms AC activation in terms of shear stress generation, irrespective of electrode geometry.
3. The shear stress displays a mild, nearly monotonic decrease with increasing frequency, particularly noticeable for the electrode case w = 7300 µm and under lower normal pressure conditions.
4. For each frequency and electrode case, the EAD shear stress increases with higher normal pressure values. This alignment with the expected relationship between normal pressure and shear stress, as observed in the friction results, emphasizes the impact of normal pressure on shear stress due to friction.

In summary, these results offer insights into the performance of specimens using a 12 µm thick PET dielectric film during AC tests, taking into account factors such as frequency, electrode geometry, and normal pressure. The relatively small error bars suggest that the performance of this material is less affected by dielectric film quality issues, as seen in previous friction tests.

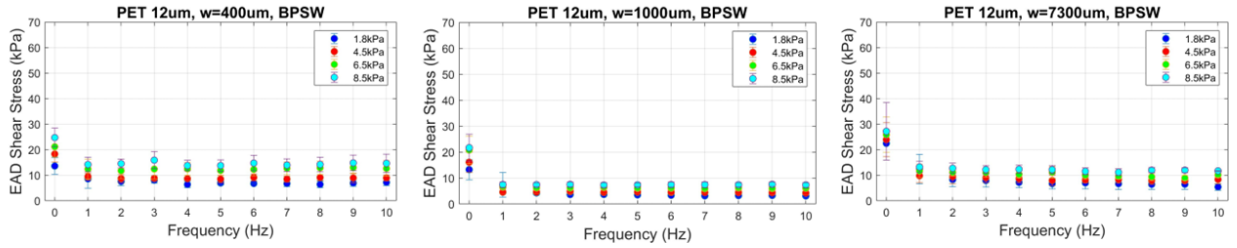

Figure 65 AC results for PET

PEN

The graphs in Figure 66 represent the results of the AC tests conducted on specimens using an 8 µm thick PEN dielectric film. The key findings from these results are as follows:

1. Error bars are relatively small, confirming that the performance is not significantly affected by the high quality of the employed 8 µm thick PEN dielectric film. This aligns with the positive outcomes observed in the friction results.
2. Similar to previous cases, the highest shear stress is consistently achieved under DC activation conditions for all electrode configurations. This reaffirms the superiority of DC activation in terms of shear stress generation, irrespective of electrode geometry.
3. The shear stress demonstrates a gradual, nearly monotonic reduction as the frequency increases, particularly notable for the electrode cases with widths of 1000 µm and 7300 µm, and under lower normal pressure conditions.
4. For each frequency and electrode case, the EAD shear stress increases with higher normal pressure values. This relationship between normal pressure and shear stress aligns with the expected pattern, consistent with the results obtained from friction tests, highlighting the role of normal pressure in shear stress due to friction.

In summary, these results provide insights into the performance of specimens using an 8 µm thick PEN dielectric film during AC tests, taking into account various factors such as frequency, electrode geometry, and normal pressure. The relatively small error bars confirm that the quality of the dielectric film has a limited impact on the material's performance, as also demonstrated in earlier friction tests.

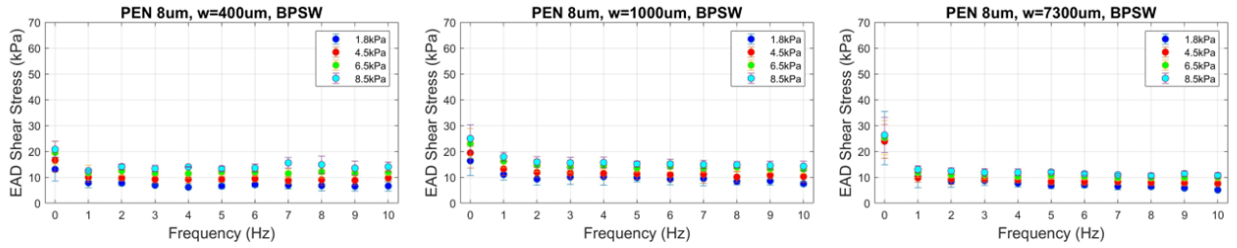

Figure 66 AC Results for PEN

In summary, the AC tests have provided valuable insights into the performance of the EAD specimens. Several important conclusions can be drawn from these tests: The highest shear stress is consistently achieved at 0 Hz, which corresponds to the conditions of DC tests. This trend is observed across all tested materials, electrode geometries, and normal pressure cases. For frequencies higher than 0 Hz, the influence of frequency on shear stress is either very modest or negligible. In cases where a dependency is evident, it primarily involves a mild decrease in shear stress. This reduction is more noticeable for larger electrode widths and under lower normal pressure conditions. The repeatability of the test results, and thus the ease of their interpretation, is influenced by the quality of the dielectric films. Specifically, Mylar with a thickness of 25 μm and PEN with a thickness of 8 μm exhibited the best repeatability, while PEEK with a thickness of 23 μm demonstrated the lowest repeatability. Overall, the AC tests emphasize that the highest shear stresses are consistently achieved when the EAD is operated under DC activation, regardless of the material or electrode geometry used. To further compare these material, electrode geometry, and normal pressure cases, we will exclusively consider the results from DC tests.

9.3.3 DC tests

In the pursuit of a comprehensive understanding of the Electrostatic Adhesive Device (EAD) performance, a systematic evaluation was conducted for each of the four normal pressure values of interest: 1.8 kPa, 4.5 kPa, 6.5 kPa, and 8.5 kPa. This investigation involved rigorous testing of all 72 fabricated EAD specimens using DC step signals.

The tests encompasses six different voltage levels evenly distributed from 0 V to 70% of the breakdown voltage specific to each material and electrode geometry. This breakdown voltage was determined through destructive tests on separate EAD specimens. The selected maximum voltage level was carefully chosen to balance EAD lifetime considerations while still achieving substantial shear stress values. The results obtained from this meticulous testing regimen are presented in various forms, each shedding light on critical aspects of EAD behavior. These include EAD shear stress vs. Voltage plots, where distinct colored circle markers delineate different normal pressure values. Additionally, EAD shear stress vs. Voltage plots, featuring varied circle markers based on normal pressure values, serve to emphasize the effective shear stress generated solely through electrical activation. To further explore the interplay between effective shear stress and applied normal pressure, EAD shear stress vs. Normal pressure plots are provided. These plots incorporate a spectrum

of colored circle markers and lines, each associated with a specific voltage value. Such comprehensive analysis enables a more profound understanding of the dependency of effective shear stress on the varying normal pressure conditions.

The presentation of these plots follows a structured format for clarity and ease of interpretation:

- Each material type, including Mylar 25 um, PEEK 23 um, PI 25 um, PET 12 um, PEN 8 um, is allocated an individual paragraph, ensuring that the data remains organized and accessible.

- Within each paragraph, a series of plots is provided, each corresponding to one of the three electrode geometries considered: w = 400 um, w = 1000 um, and w = 7300 um. This separation facilitates a detailed analysis of the impact of electrode geometry on EAD performance for each material.

- The data presented in these plots represents the mean values, meticulously derived from sixteen trials. Each of these trials comprises four tests carried out under identical electrical and normal pressure conditions. This method offers robust and representative results.

- To provide a comprehensive picture of data variability, the shear stress vs. voltage plots are supplemented with error bars, giving insight into the dispersion of data points across the sixteen trials. This approach ensures transparency and a thorough understanding of the data's reliability.

This organized structure serves to facilitate the assessment and comparison of EAD performance across materials and electrode geometries, ultimately contributing to a more comprehensive analysis of the experimental results.

Mylar

This paragraph presents the results of the DC tests performed on four nominally identical EAD specimens, with four tests conducted for each specimen and test condition. These specimens were constructed using a 25 um thick Mylar dielectric film. The findings indicate several key observations:

- Shear stress exhibits a significant increase with higher voltages across all electrode and normal pressure cases.

- There is a positive correlation between shear stress and electrode width, with wider electrodes producing higher shear stress levels for each voltage and normal pressure case.

- Shear stress is also positively associated with increased normal pressure, with higher pressure levels leading to greater shear stress. This trend aligns with the established relationship between normal pressure and shear stress due to friction.

- Some data dispersion is observed; however, this is attributed to variations among the four nominally identical EAD specimens. These variations may arise from differences in dielectric film material properties or electrode manufacturing processes.

A comparison with the preceding results reveals several key findings. Firstly, the EAD shear stresses continue to be maximized with the larger electrode width (w = 7300 um). Notably, there is a slight reduction in data dispersion, which may be attributed to variations in the frictional properties of nominally identical EAD specimens. These findings contribute to a deeper understanding of the interplay between electrode geometry, voltage activation, and resultant shear stress in Mylar EADs with 25 um thickness.

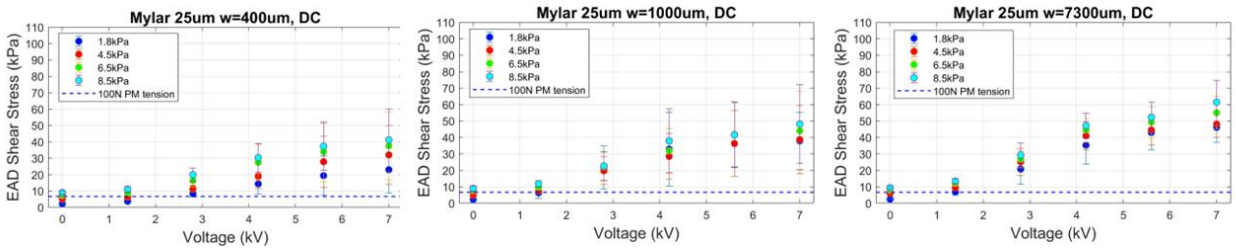

Figure 67 DC results Mylar

PEEK

Here are presented the results of DC tests conducted on four nominally identical EAD specimens, with four tests carried out for each specimen and test condition. These specimens were fabricated using a 23 um thick PEEK dielectric film. The findings reveal several important insights:

- Shear stress experiences a significant increase with higher voltage levels across all normal pressure and electrode configurations.

- Shear stress levels are relatively higher and similar for electrode widths of both 400 um and 7300 um, regardless of voltage and normal pressure conditions.

- There is a consistent trend of higher shear stress with increased normal pressure, aligning with the known relationship between normal pressure and shear stress due to friction.

- The data exhibit notable dispersion, primarily attributed to variations among the four nominally identical EAD specimens stemming from differences in dielectric film material properties or electrode manufacturing processes.

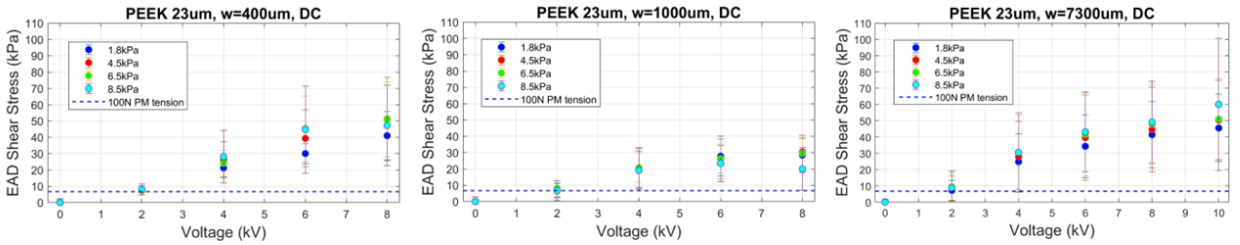

Figure 68 DC results PEEK

Polyimide

Here are presented the results of DC tests performed on four nominally identical EAD specimens, with four tests conducted for each specimen and test condition. These specimens were constructed using a 25 um thick PI dielectric film. The findings reveal several key observations:

- Shear stress exhibits a substantial increase with higher voltage levels across all normal pressure and electrode configurations.

- Shear stress is notably higher, similar, and more consistent for electrode widths of 400 um and 1000 um, regardless of voltage and normal pressure conditions.

- There is a consistent pattern of higher shear stress with increased normal pressure, in line with the expected relationship between normal pressure and shear stress due to friction.

- The data display significant dispersion, primarily attributed to variations among the four nominally identical EAD specimens stemming from differences in dielectric film material properties or electrode manufacturing processes.

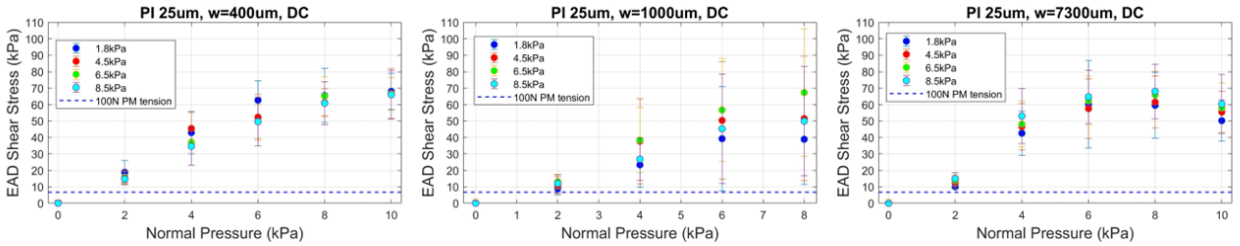

Figure 69 DC results Polyimide

PET

Here are presented the EAD shear stress versus voltage results of the DC tests conducted on four nominally identical EAD specimens, with four tests conducted for each specimen and test condition. These EAD specimens were constructed using a 12 um thick PET dielectric film. The findings reveal several key observations:

- Shear stress exhibits a notable increase with higher voltage levels across all normal pressure and electrode configurations.

- Shear stress is consistently higher for the electrode width w = 7300, irrespective of voltage and normal pressure conditions.

- There is a consistent pattern of higher shear stress with increased normal pressure, aligning with the anticipated relationship between normal pressure and shear stress due to friction.

- The data display significant dispersion, primarily attributed to variations among the four nominally identical EAD specimens resulting from differences in dielectric film material properties or electrode manufacturing processes.

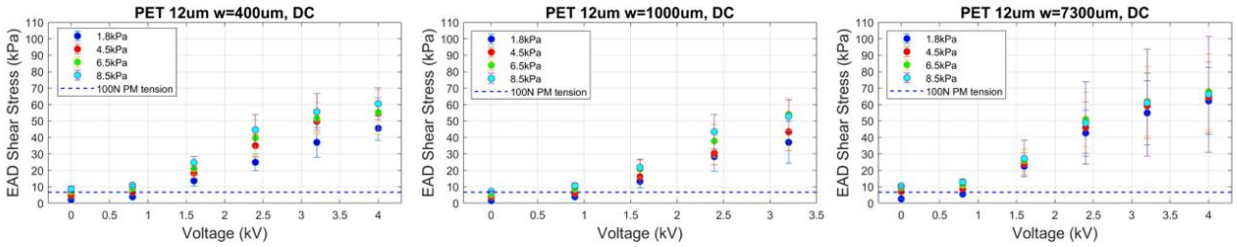

Figure 70 DC results PET

PEN

Here are presented the outcomes of DC tests focusing on EAD shear stress in relation to voltage. These tests involved four nominally identical EAD specimens, with four tests conducted for each specimen and test condition, all of which were constructed using an 8 um thick PEN dielectric film. The key findings are as follows:

- Shear stress demonstrates a substantial increase with higher voltage levels, across all normal pressure and electrode configurations.

- Shear stress consistently registers as higher for the electrode width w = 7300, regardless of the specific voltage and normal pressure conditions.

- There is a persistent pattern of higher shear stress corresponding to elevated normal pressure levels, aligning with the expected relationship between normal pressure and shear stress due to friction.

- The data exhibit some dispersion, primarily attributed to variances among the four nominally identical EAD specimens stemming from differences in dielectric film material properties or electrode manufacturing processes.

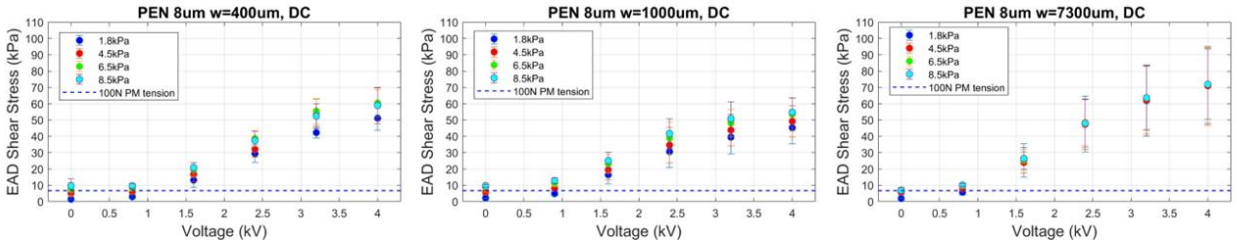

Figure 71 DC results PEN

9.3.4 Energy Consumption

The same DC experiments that were carried out to examine the shear stress response of the fabricated EAD specimens, were also employed to assess their energy consumption. Specifically, two key parameters were investigated:

1. Activation Energy: This metric represents the energy required by the EAD to achieve full electrification upon activation. It encompasses the energy consumed during EAD capacitance charging, as well as the subsequent dielectric relaxation and the sweep of mobile ions toward the electrodes. These processes are influenced by the non-ideal behavior of the dielectric film.

2. Mean Power: Mean power characterizes the average power consumed by the EAD to maintain grasping after complete activation. This power consumption is primarily attributed to current leakage due to the finite volume resistivity of the dielectric film.

The results regarding electrical consumption are presented in the following formats:

- Activation Energy vs. Voltage Plot: Each plot employs different colored circle markers to represent data points for each normal pressure value.

- Mean Power vs. Voltage Plot: Similar to the activation energy plots, each plot uses variously colored circle markers to denote different normal pressure values.

These plots are structured as follows:

- Each material (Mylar 25 um, PEEK 23 um, PI 25 um, PET 12 um, and PEN 8 um) is allocated to a dedicated plot.

- Within each plot, individual plots correspond to specific electrode geometries (w = 400 um, w = 1000 um, and w = 7300 um).

- Different colored circle markers are used within each plot to differentiate between normal pressure values (1.8 kPa, 4.5 kPa, 6.5 kPa, and 8.5 kPa).

- In all plots, reported circle markers represent the mean values derived from sixteen trials, where four tests were conducted under identical electrical and normal pressure conditions for each of the four nominally identical EAD specimens produced with the same material and geometry.

- Error bars are also incorporated alongside the circle markers in these plots to provide insight into the variability of the data from the sixteen trials.

The graphs report the EAD Activation energy and Mean power vs. Voltage results for all the

1) Activation energy and Mean power increase sensibly with voltage, for all electrode and normal pressure cases.
2) Activation energy shows a little dependency on normal pressure and appreciably increases with increasing electrode width.
3) Mean power shows a negligible dependency on normal pressure and significantly decreases with increasing electrode width.

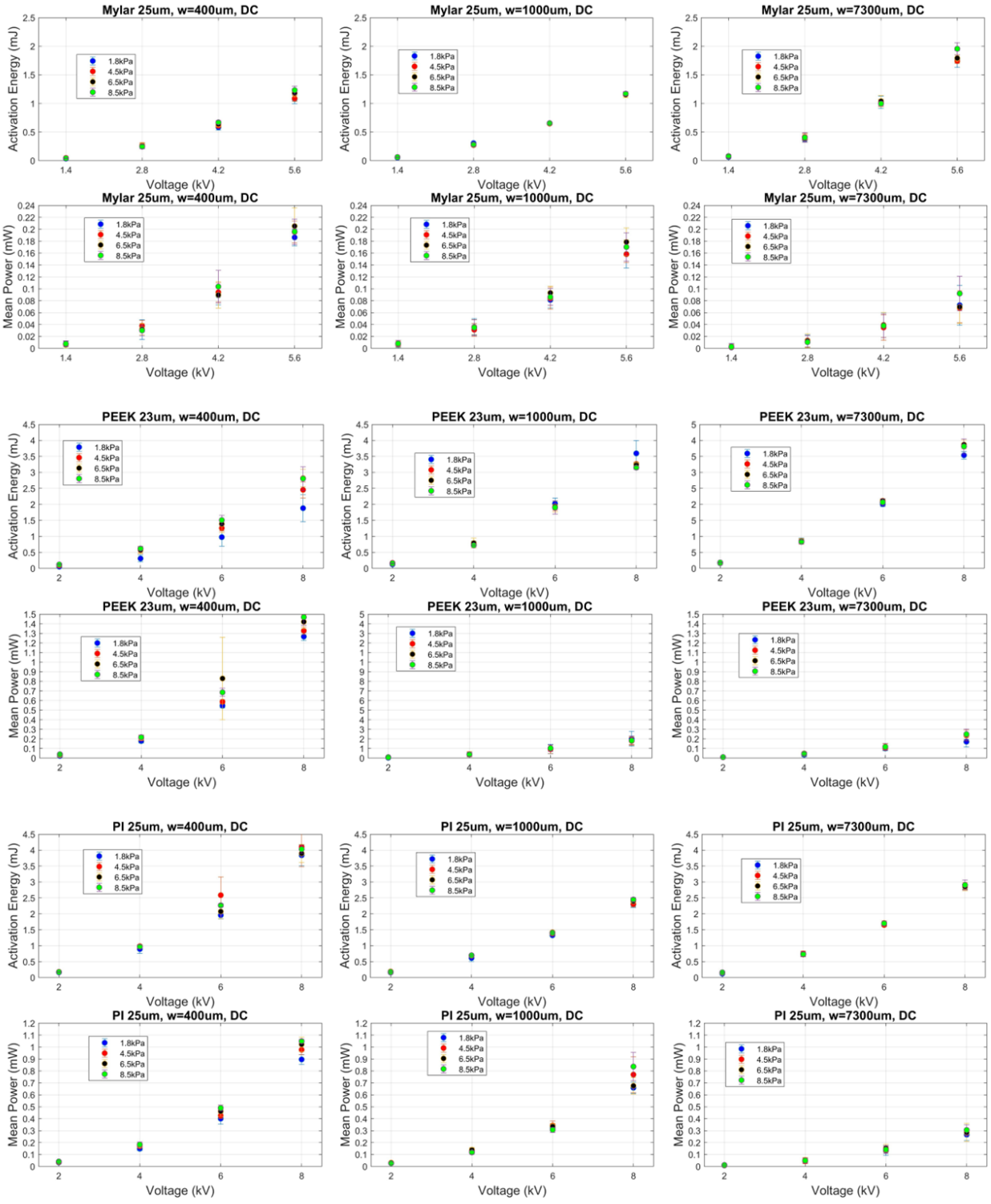
Mylar 25um, w=400um, DC
Mylar 25um, w=1000um, DC
Mylar 25um, w=7300um, DC
PEEK 23um, w=400um, DC
PEEK 23um, w=1000um, DC
PEEK 23um, w=7300um, DC
PI 25um, w=400um, DC
PI 25um, w=1000um, DC
PI 25um, w=7300um, DC
Activation Energy (mJ)
Mean Power (mW)
Voltage (kV)
1.8kPa
4.5kPa
6.5kPa
8.5kPa

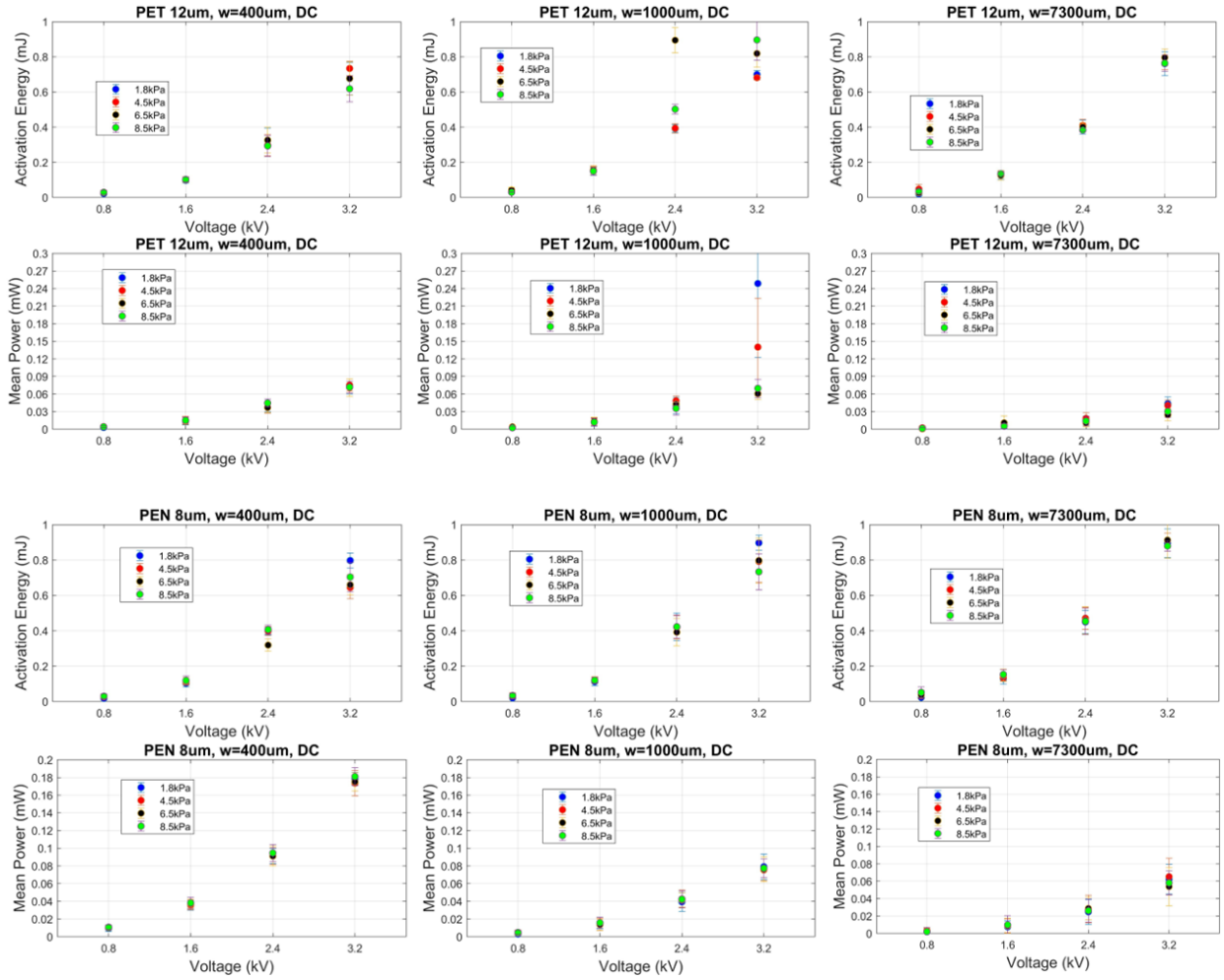

Figure 72 Mean power and activation energy of the different geometries and different materials

9.3.5 EAD Specimen Capacitance

This section presents the results of capacitance measurements conducted on all 72 manufactured EAD specimens. The following key details characterize these tests:

1. The measurements were executed at a constant normal pressure value of 6.5 kPa. This choice was made after establishing, with a reduced sample size, that capacitance displays negligible dependency on normal pressure for values exceeding the minimum threshold considered here (1.8 kPa).
2. Each EAD specimen underwent four separate trials, resulting in a total of 16 trials for every combination of the six materials and the three electrode configurations.

The outcomes are organized in the following tabulated format, featuring both mean and standard deviation (STD) values for each material and electrode combination. The key observations from these results are as follows:

- Capacitance values exhibit a consistent similarity across all combinations of materials and electrodes.
- Capacitance demonstrates a decreasing trend as the electrode width increases.
- With the exception of Mylar 25 um and PEN 8 um, the data reveal a notable degree of variability, confirming the superior quality of the Mylar 25 um and PEN 8 um dielectric films.

This variation, in conjunction with the findings from the friction results helps explain the considerable data dispersion observed in the shear stress plots, especially for materials other than Mylar 25 um and PEN 8 um. This variation is attributed to the dependence of EAD shear stress on the friction coefficient between the contacting surfaces of the EAD and testing material, as well as on the changes in capacitance during the detachment of the EAD and testing material along the direction perpendicular to the contacting surfaces.

It's noteworthy to mention that the significant data variability predominantly arises among tests performed on four nominally identical EAD specimens, rather than among the four trials conducted on the same EAD specimen.

C (pF)	Mylar 25 µm	PEEK 23 µm	PI 25 µm	PET 12 µm	PEN 8 µm	PI 12 µm
w = 7300						
Mean	21	19	21	18	23	22
STD	1	4	3	4	2	3
w = 1000 µm						
Mean	21	19	22	23	27	22
STD	2	2	4	2	1	5
w = 400 µm						
Mean	22	21	26	25	29	24
STD	2	3	2	2	1	1

Table 8 Capacitance of the EADs with different geometry and dielectric substrate

The results presented in this section shed light on the extensive characterization of Electro-Adhesive Devices (EADs) in the context of different dielectric materials, electrode geometries, and operating conditions. These investigations aimed to comprehensively understand the performance and behavior of EADs, with a specific focus on the influence of electrical activation methods.

To this end, a diverse range of EAD specimens was utilized, incorporating different dielectric materials such as 25 um PET, 8 um PEN, 25 um PI, and 23 um PEEK. Despite the variation in materials, all specimens shared a consistent electrode geometry characterized by a gap (g) of 400 um and a width (w) of 7300 um. The electrical activation employed in these experiments involved the

use of 4 kV amplitude bipolar square wave (BPSW) signals at various frequencies, all under a constant 1.8 kPa pre-load. The results of these tests have provided valuable insights:

1. Material-Dependent Variations: It became evident that different dielectric materials yield diverse responses when subjected to the same electrical activation conditions. This underscores the significance of material selection in optimizing EAD performance.

2. Frequency Dependency: An intriguing observation emerged, indicating a substantial influence of the operating frequency on EAD performance. As the frequency increased, a significant decrease in performance was noted. However, the specific frequency at which performance declined significantly varied depending on the dielectric material employed.

These findings have highlighted the complex relationship between material properties, electrode geometry, and electrical activation, motivating further in-depth investigations. The influence of frequency on EAD response for different materials presents a promising avenue for future research, warranting more detailed exploration.

In summary, these experiments have furnished critical insights into the behavior of EADs, particularly regarding material variations and the role of frequency in their performance. These findings lay the groundwork for more extensive experimental campaigns, which will explore a broader range of materials and focus on a select set of geometries. Notably, it has been discerned that the gap's value does not significantly impact device performance in this specific application, leading to the decision to vary only the electrode thickness to streamline future investigations. These comprehensive studies pave the way for a deeper understanding of EAD behavior and its potential applications across various domains.

Chapter 10. Some Applications

10.1 Introduction

In this chapter, we delve into secondary endeavors related to the applications of electro-adhesion in various contexts. Through collaborations with companies and the exploration of alternative uses of electro-adhesion beyond the shear grip discussed in the earlier examples, the technology has been pushed to its limits. Our initial attempts focused on harnessing the force acting perpendicular to the surface of objects, enabling us to grasp a wide array of materials, ranging from conductive to dielectric, from organic to vitreous. Subsequently, we implemented electro-adhesion as an end effector in a delta robot, where we scrutinized the gripping dynamics in a pick-and-place system for paper bundles. We also examined its braking effect on specific materials, such as embossed paper, shedding light on its potential applications in unique scenarios. Moreover, electro-adhesive devices were utilized unconventionally as simple capacitive systems in the development of an electrostatic motor. These multifaceted experiments and explorations not only showcase the versatility of electro-adhesion but also extend its utility beyond traditional boundaries. The applications span a spectrum of industries, offering innovative solutions that leverage the capabilities of this technology in unexpected and promising ways.

10.2 Normal Force empirical evaluation

Until now, in this thesis work, electro-adhesive force has been extensively studied concerning its shear direction on the electroactive surface and the surface of the grasped object. Now, we describe the methodology for empirically testing the normal grasping of objects of various natures. This methodology, simple in its nature, allows for an initial assessment of the effectiveness of the Electro-Adhesion Device (EAD) on different types of materials, whether conductive, dielectric, or of mixed nature. Furthermore, it offers clear insights into the most suitable electrode geometry for effective grasping and the optimal material for the gripping substrate. While a detailed analysis of the geometry, as performed in Chapter 9. cannot be replaced by empirical evaluation, this preliminary test can effectively guide the study. Various handles have been constructed to facilitate the safe handling of the electro-adhesive devices. These handles were 3D-printed using resin with a FormLab Form 2 printer, using white Rigid 4000 and blue Tough resins. The CAD model of the handle is

depicted in Figure 73 Handles to empirical evaluation of normal EA performance. The handle consists of a hollow cylinder with internal cavities to accommodate the connection cables between the power supply and the device. The electro-adhesive device is affixed at the handle's end, ensuring that its adhesive surface faces downward, protruding by 2 mm to ensure contact solely between the device and the object to be gripped. Electrical connections are embedded within the structure, ensuring proper electrical insulation for safe handling without electrical risk. The electro-adhesive devices are manufactured following the standard procedure outlined in Chapter 7. Electrodes are deposited using DoD inkjet printing with the JetLab x4 by Microfab, employing silver nanoparticle-based ink (Anapro) on a thin plastic film substrate, which can be PET, PI, Mylar, etc. After printing the electrodes and sintering the ink in an oven for an hour, a layer of PDMS (Silpuran 6000/05) is applied to insulate the electrodes. Prior to this, the surface is treated with oxygen plasma and silicone primer. The handles described, depicted in Figure 73, were employed. Figure 73, on the bottom, represents EADs of three different materials and geometries. From the left, Kapton (PI) with wider electrodes (w=21mm) and thinner electrodes (w=0.4mm) is used as electroactive layer. The last on the right side is made with a thin layer of silicone, or PDMS. Table 9 summarizes the successful test cases, by meaning the complete lifting of the object, along with details of the waveform utilized, the voltage supplied to the device, and the device geometry, named as follows: 2 electrodes refers to w=21mm, Thin interdigit refers to w=0.4mm.

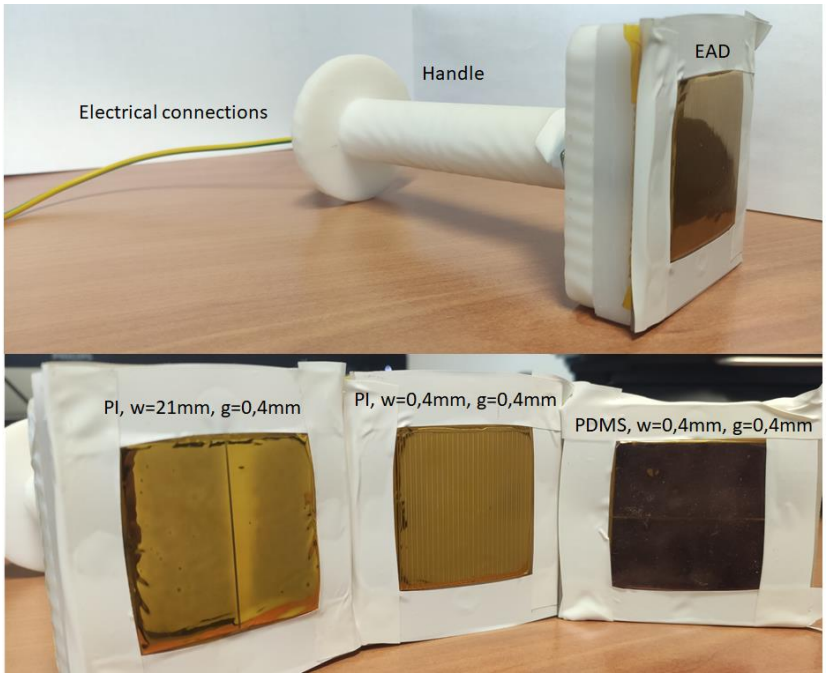

Figure 73 Handles to empirical evaluation of normal EA performance

It is fundamental to establish the supplied voltage dynamics to optimize force performance. Specifically, other than the amplitude setting, waveform shape and frequency significantly influence

the polarization dynamics of the material and so the electrostatic attraction between the device and the object. Once again, the optimal choice is contingent upon the material to which the device adheres, both in shear and normal directions. Empirical findings have indicated that for holding action, a DC voltage supplied is more effective than alternate. Conversely, for a gripping action in shear direction, a square wave at a frequency of 2.5 Hz performed the best in most of the cases, by allowing the EAD to be adaptively adhered onto the object surface. In the case of normal gripping, outcomes have been observed to be contingent upon the inherent nature of the material, whether conductive or dielectric. The devices are powered by a 10kV high voltage power supply, bipolar (Ultravolt 10HVA24-BP1), 1W power.

Material	El. Property	Geometry	Waveform	Voltage applied
Sheet of paper	Dielectric	2 electrodes	DC	2 kV
Letter Envelope	Dielectric	2 electrodes	DC	3 kV
Tea bag wrapper	Dielectric	2 electrodes	AC trapezoidal	2 kV
Tea sachet	Dielectric	2 electrodes	AC trapezoidal	2 kV
Cardboard	Dielectric	2 electrodes	DC	4 kV
Fiberglass	Dielectric	2 electrodes	DC	4 kV
Carbon fiber	Conductive	2 electrodes	AC trapezoidal	2 kV
Epoxy resin sheet	Dielectric	2 electrodes	AC trapezoidal	2 kV
Poly-laminated cardboard	Dielectric	2 electrodes	AC trapezoidal	2 kV
Solid Aluminum	Conductive	2 electrodes	DC	3 kV
Aluminum foil	Conductive	2 electrodes	DC	1 kV
Copper	Conductive	2 electrodes	DC	3 kV
Brass	Conductive	2 electrodes	DC	3 kV
PET foil	Dielectric	Thin inderdigit	DC	4 kV
Kapton foil	Dielectric	Thin inderdigit	DC	4 kV

Table 9 Successful normal prehension cases

This gripping method, after empirical testing using the handles mentioned above and gaining a clearer understanding of suitable materials and waveforms for different material types, was integrated into a delta robot for pick and place operations. The devices were created following the procedure detailed in Chapter 7. A 25.4 μm Polyimide substrate was chosen as the dielectric to generate the adhesive force. A two-electrode geometry was selected (Figure 74) to be printed using the Inkjet Printing method with the JetLab x4 DoD inkjet printer. The ink composing the electrodes is based on silver nanoparticles (by Anapro) and is deposited using the methodology described earlier. The insulating layer consists of PDMS (Silpuran 6000/05) deposited through doctor blade casting.

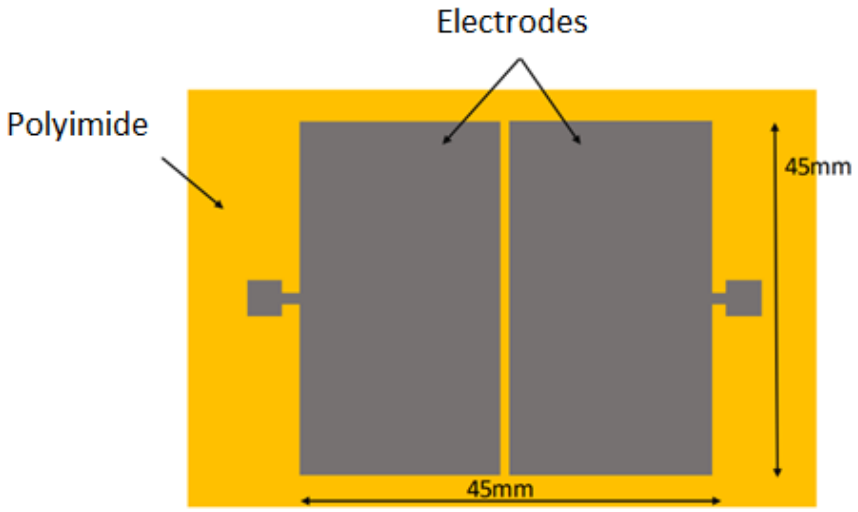

Figure 74 Electrode geometry designed for EAD working in a delta robot application

The implementation of the device is the same of the handles; it is positioned at the lower end of a structure containing electrical connections to the high-voltage power supply. All electrical connections are embedded within the structure to prevent dangerous dissipation for the delta robot's framework. A bipolar power supply of 10 kV (Ultravolt 10HVA24-BP1) was used for the power source. The entire control of the robot and high voltage is managed through an IPC Beckhoff, handling the entire system in real-time.

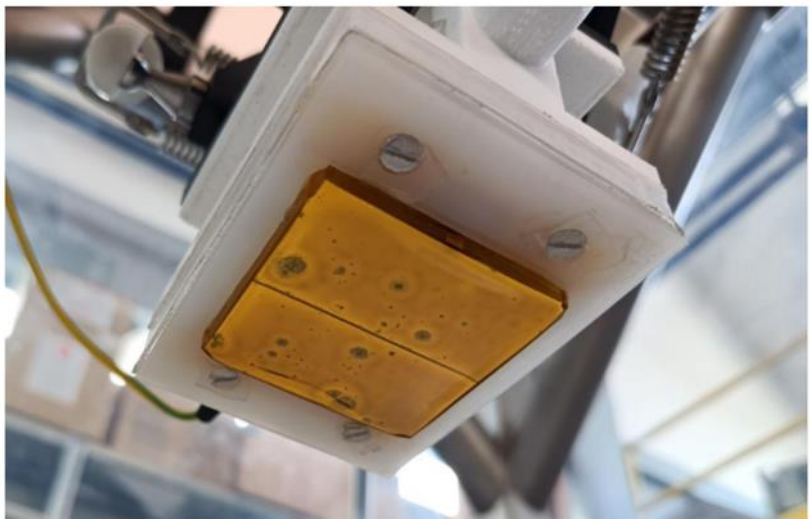

Figure 75 EAD mounted on end-effector of delta robot

The dynamics of the system can be divided into three parts:

1) Gripping: The initial phase involves engaging the electro-adhesive device with the target object. Based on the material of the object, the appropriate waveform and voltage are selected to generate an adequate adhesive force. Once the device adheres to the object, it's ready for the next phase.

2) Lifting and Transport: After gripping, the delta robot moves upward to lift the object off its initial surface. The object is held securely by the adhesive force.
3) Release: When the robot reaches the desired destination, it releases the object by applying a damped sinusoidal signal.

Figure 76 Normal prehension on a carboard pack

In the pick and place application, the target object is a cardboard box. This system allows the delta robot to perform pick and place tasks efficiently using electro-adhesion, providing a versatile and adaptable solution for handling a variety of materials. The application has yielded a significant outcome in terms of reliability and repeatability of the operation, even at high acceleration and velocity dynamics. It is necessary to find the optimum voltage activation during movement, i.e., to determine the moment of maximum contact area between the device and the package. This would be facilitated by introducing a system to measure the pre-load applied when in contact, such as a load cell placed at the end effector.

10.3 Shear Force as brake system for Embossed Paper

In order to evaluate the braking action of an electroadhesive device on embossed paper, samples produced in Polyimide as described in Chapter 7. were manufactured and tested according to the methodology expressed in 7.3 . The challenge in testing the effectiveness of electroadhesion on a substrate with such an uneven surface lies in the minimal microscopic contact area that is created. Given the tremendous effectiveness it has demonstrated on smooth substrates, thus maximizing the contact area between the two, it is expected that a pattern like embossing significantly and negatively affects electrostatic adhesion. Therefore, tests were conducted by applying both AC and DC potential. Considering all the empirical results obtained previously, the samples were designed with two

electrodes separated by a gap, to create an electric field that extends more into space. The electrodes were deposited using DoD inkjet printing on a 25.4 µm Polyimide substrate. The test bench used is the same as described in 7.3 for the evaluation of cutting forces on thin films.

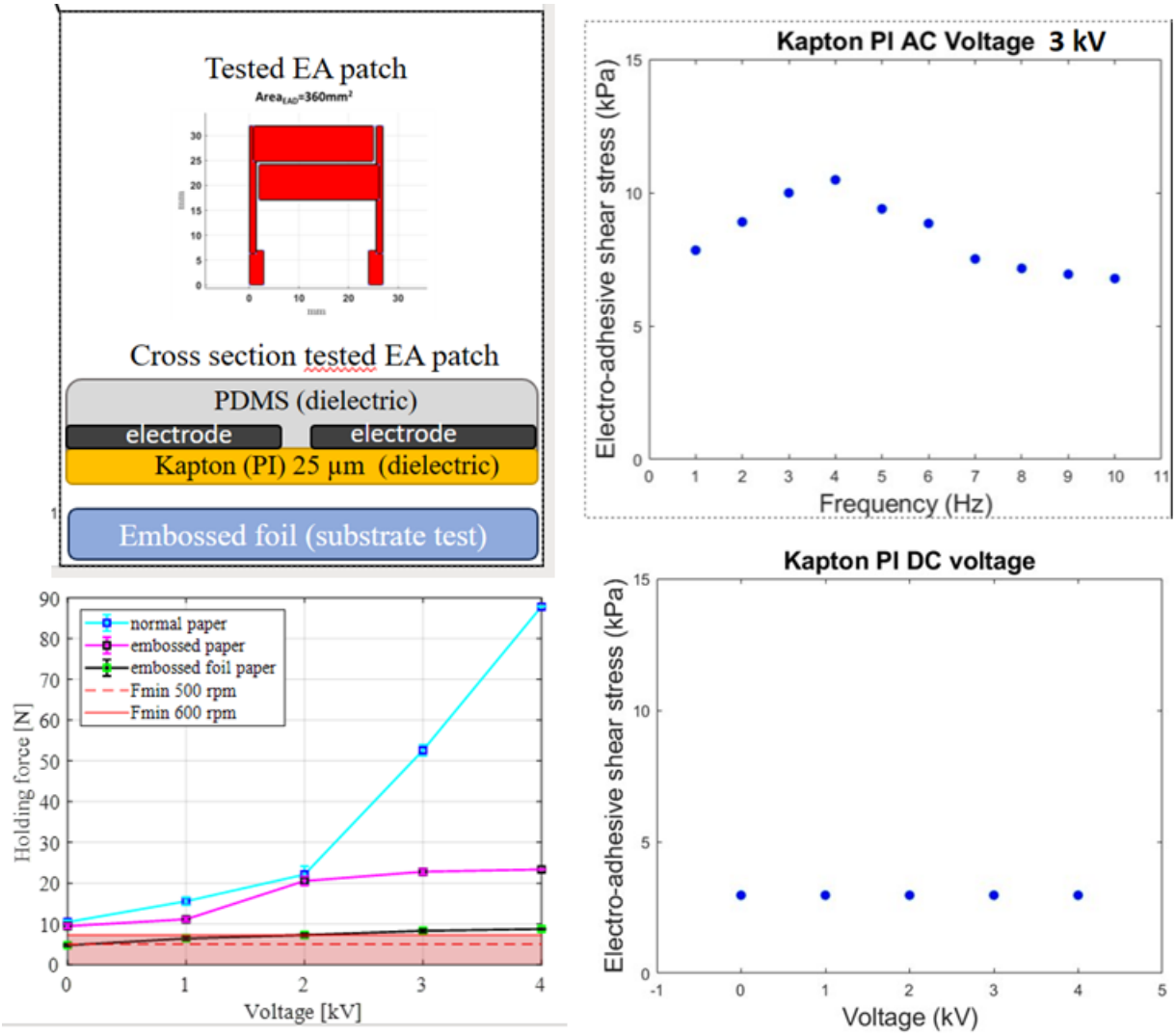

Figure 77 Top left: Manufacturing scheme of EAD produced. Right: DC and AC voltage results for ESS performance. Bottom Left: holding force with respect to normal paper

The results were then compared with other types of paper used. Figure 77 presents the force results related to the hypothetical braking force required in a rotating system. It is noticeable how the difference compared to the regular printer paper is very evident, given the surface pattern of the embossed paper. In any case, the force effect is significant and proves to be sufficient for the hypothetical braking action. This application confirms the great potential of an electro-adhesive system to replace vacuum or mechanical systems in certain applications.

Chapter 11. Conclusions

The concluding remarks of this doctoral thesis provide a comprehensive overview of electroadhesion technology in both theoretical and practical contexts. The physical nature of the phenomenon is described, drawing comparisons with analogous technologies, and its potential application fields are explored with a theoretical treatment. The devices utilizing electroadhesion (Electro-adhesive Devices or EADs) to adhere to and manipulate objects are detailed. Typically, these devices consist of a pair of electrodes generating an electric field and two dielectric materials serving as insulation and a polarized gripping surface. The historical development of these devices is referenced, emphasizing early applications with a focus on achieving optimal cutting force performance. Notably, advanced manufacturing processes, specifically the Drop on Demand (DoD) inkjet printing technique, were employed in this thesis to produce electro-adhesive devices. This alternative approach aimed to optimize geometric aspects, such as material thickness and electrode geometry.

The utilization of statistical analyses, such as the Design of Experiments (DOE), is presented for optimizing the print parameters of the inkjet printer in relation to the outcome of electrode geometry. This work represents a frontier that explores the application of statistical methods for predicting outcomes and optimizing the manufacturing process of these devices. The precise definition of electrode parameters is crucial, and employing statistical techniques like DOE enables a systematic approach to understanding and enhancing the manufacturing process.

In another study, an ink with excellent dielectric properties was printed to allow for the adjustment of the gripping layer thickness, aiming to enhance the performance of Electro-adhesive Devices (EADs). This innovative technique resulted in a force three times greater than the maximum value reported in the literature for this class of devices.

An empirical study was conducted to optimize the electrode geometry in a specific application where the electroadhesive device was used as a brake on a poly-laminate film. The study led to the identification of the optimal geometry, considering factors such as maximum cutting force, breakdown resistance, energy consumption, activation time, and the definition of the power dynamics involved in the process.

References

[1] A. Prehension, “An Analysis of Activities,” *Relig. Educ.*, vol. 16, no. 4, pp. 232–232, 1921, doi: 10.1080/0034408210160417.

[2] J. Guo, K. Elgeneidy, C. Xiang, N. Lohse, L. Justham, and J. Rossiter, “Soft pneumatic grippers embedded with stretchable electroadhesion,” *Smart Mater. Struct.*, vol. 27, no. 5, 2018, doi: 10.1088/1361-665X/aab579.

[3] R. Chen, Y. Huang, and Q. Tang, “An analytical model for electrostatic adhesive dynamics on dielectric substrates,” *J. Adhes. Sci. Technol.*, vol. 31, no. 11, pp. 1229–1250, 2017, doi: 10.1080/01694243.2016.1249689.

[4] J. Shintake, V. Cacucciolo, D. Floreano, and H. Shea, “Soft Robotic Grippers,” *Adv. Mater.*, vol. 30, no. 29, 2018, doi: 10.1002/adma.201707035.

[5] K. Asano, F. Hatakeyama, and K. Yatsuzuka, “Fundamental study of an electrostatic chuck for silicon wafer handling,” *IEEE Trans. Ind. Appl.*, vol. 38, no. 3, pp. 840–845, 2002, doi: 10.1109/TIA.2002.1003438.

[6] J. Singh, “Electro-Adhesive Gripper Component Selection for Pick and Place of Commonly Used Materials,” 2019.

[7] B. C. Leung, N. R. Goeser, L. A. Miller, and S. Gonzalez, “Validation of electroadhesion as a docking method for spacecraft and satellite servicing,” *IEEE Aerosp. Conf. Proc.*, vol. 2015-June, 2015, doi: 10.1109/AERO.2015.7119283.

[8] T. Nakamura and A. Yamamoto, “Modeling and control of electroadhesion force in DC voltage,” *ROBOMECH J.*, vol. 4, no. 1, 2017, doi: 10.1186/s40648-017-0085-3.

[9] C. Cao, X. Sun, Y. Fang, Q. H. Qin, A. Yu, and X. Q. Feng, “Theoretical model and design of electroadhesive pad with interdigitated electrodes,” *Mater. Des.*, vol. 89, no. January, pp. 485–491, 2016, doi: 10.1016/j.matdes.2015.09.162.

[10] M. Vaezi, H. Seitz, and S. Yang, “A review on 3D micro-additive manufacturing technologies,” *Int. J. Adv. Manuf. Technol.*, vol. 67, no. 5–8, pp. 1721–1754, 2013, doi: 10.1007/s00170-012-4605-2.

[11] J. Guo, J. Leng, and J. Rossiter, “Electroadhesion Technologies for Robotics: A Comprehensive Review,” *IEEE Trans. Robot.*, vol. 36, no. 2, pp. 313–327, 2020, doi:

10.1109/TRO.2019.2956869.

[12] C. Balakrishnan, “Johnsen-Rahbek effect with an electronic semi-conductor,” *Br. J. Appl. Phys.*, vol. 1, no. 8, pp. 211–213, 1950, doi: 10.1088/0508-3443/1/8/304.

[13] B. A. D. Stuckes and A. P. Inst, “Johnsen-Rahbek effect,” *J. Inst. Electr. Eng.*, vol. 2, no. 15, pp. 173–175, 1956, doi: 10.1049/jiee-3.1956.0066.

[14] P. M. Taylor, G. J. Monkman, and G. J. F. Farnworth, “Principles of electroadhesion in clothing robotics,” *Int. J. Cloth. Sci. Technol.*, vol. 1, no. 3, pp. 14–20, 1989, doi: 10.1108/eb002951.

[15] H. Prahlad, R. Pelrine, S. Stanford, J. Marlow, and R. Kornbluh, “Electroadhesive robots - Wall climbing robots enabled by a novel, robust, and electrically controllable adhesion technology,” *Proc. - IEEE Int. Conf. Robot. Autom.*, pp. 3028–3033, 2008, doi: 10.1109/ROBOT.2008.4543670.

[16] G. Monkman, “Electroadhesive microgrippers,” *Ind. Rob.*, vol. 30, no. 4, pp. 326–330, 2003, doi: 10.1108/01439910310479595.

[17] S. M. J. Mahmoudzadeh Akherat, M. A. Karimi, V. Alizadehyazdi, S. Asalzadeh, and M. Spenko, “A tunable dielectric to improve electrostatic adhesion in electrostatic/microstructured adhesives,” *J. Electrostat.*, vol. 97, no. July 2018, pp. 58–70, 2019, doi: 10.1016/j.elstat.2018.12.001.

[18] Pearson, Ed., *griffiths.pdf*, 2013th ed. Boston.

[19] B. N. J. Persson and P. G. Institut-, “General theory of electroadhesion,” 2021.

[20] S. Parameters, “Analysis of Potential of Raising Forces Acting on Electroadhesive Pads Depending on Polarization and,” 2021.

[21] S. J. Woo and T. Higuchi, “Electric field and force modeling for electrostatic levitation of lossy dielectric plates,” *J. Appl. Phys.*, vol. 108, no. 10, 2010, doi: 10.1063/1.3487938.

[22] D. J. Griffiths and C. Inglefield, *Introduction to Electrodynamics*, vol. 73, no. 6. 2005.

[23] N. Berdozzi *et al.*, “Rapid Fabrication of Electro-Adhesive Devices With Inkjet Printed Electrodes,” *IEEE Robot. Autom. Lett.*, vol. 5, no. 2, pp. 2770–2776, Apr. 2020, doi: 10.1109/LRA.2020.2972838.

[24] British Standards Institution, “BS EN ISO 8295:2004 Plastics — Film and sheeting — Determination of the coefficients of friction,” *BSI Stand. Publ. BS 82952004*, vol. 3, no. 1,

2004.

[25] A. Ceramics, *Alumina as an electrical insulator 13*. 2019.

[26] A. Society, *3 Plastic Properties and Testing 3.1*. 2018.

[27] T. Com-, I. Liquids, and U. Disk, "Standard Test Method for Dielectric Breakdown Voltage and Dielectric Strength of Solid Electrical Insulating Materials Under Direct-Voltage," *Astm*, vol. 97, no. Reapproved 2004, pp. 1–6, 2012, doi: 10.1520/D0149-09R13.2.

[28] R. Liu, R. Chen, H. Shen, and R. Zhang, "Wall climbing robot using electrostatic adhesion force generated by flexible interdigital electrodes," *Int. J. Adv. Robot. Syst.*, vol. 10, 2013, doi: 10.5772/54634.

[29] J. Guo, T. Bamber, M. Chamberlain, L. Justham, and M. Jackson, "Optimization and experimental verification of coplanar interdigital electroadhesives," *J. Phys. D. Appl. Phys.*, vol. 49, no. 41, 2016, doi: 10.1088/0022-3727/49/41/415304.

[30] A. V. Mamishev, K. Sundara-Rajan, F. Yang, Y. Du, and M. Zahn, "Interdigital sensors and transducers," *Proc. IEEE*, vol. 92, no. 5, pp. 808–844, 2004, doi: 10.1109/JPROC.2004.826603.

[31] S. Schlatter, S. Rosset, and H. Shea, "Inkjet printing of carbon black electrodes for dielectric elastomer actuators," *Electroact. Polym. Actuators Devices 2017*, vol. 10163, p. 1016311, 2017, doi: 10.1117/12.2258615.

[32] B. Andò, S. Baglio, A. R. Bulsara, T. Emery, V. Marletta, and A. Pistorio, "Low-cost inkjet printing technology for the rapid prototyping of transducers," *Sensors (Switzerland)*, vol. 17, no. 4, pp. 1–11, 2017, doi: 10.3390/s17040748.

[33] D. Ruffatto, J. Shah, and M. Spenko, "Increasing the adhesion force of electrostatic adhesives using optimized electrode geometry and a novel manufacturing process," *J. Electrostat.*, vol. 72, no. 2, pp. 147–155, 2014, doi: 10.1016/j.elstat.2014.01.001.

[34] J. Guo, T. Bamber, T. Hovell, M. Chamberlain, L. Justham, and M. Jackson, "Geometric Optimisation of Electroadhesive Actuators Based on 3D Electrostatic Simulation and its Experimental Verification," *IFAC-PapersOnLine*, vol. 49, no. 21, pp. 309–315, 2016, doi: 10.1016/j.ifacol.2016.10.574.

[35] G. D. Martin, S. D. Hoath, and I. M. Hutchings, "Inkjet printing - The physics of manipulating liquid jets and drops," *J. Phys. Conf. Ser.*, vol. 105, no. 1, 2008, doi: 10.1088/1742-6596/105/1/012001.

[36] B. J. De Gans, P. C. Duineveld, and U. S. Schubert, “Inkjet printing of polymers: State of the art and future developments,” *Adv. Mater.*, vol. 16, no. 3, pp. 203–213, 2004, doi: 10.1002/adma.200300385.

[37] J. Li, F. Rossignol, and J. Macdonald, “Inkjet printing for biosensor fabrication: Combining chemistry and technology for advanced manufacturing,” *Lab Chip*, vol. 15, no. 12, pp. 2538–2558, 2015, doi: 10.1039/c5lc00235d.

[38] G. K. Lau and M. Shrestha, “Ink-jet printing of micro-elelectro-mechanical systems (MEMS),” *Micromachines*, vol. 8, no. 6, pp. 1–19, 2017, doi: 10.3390/mi8060194.

[39] M. Technology, “Control of Droplet Formation in Inkjet Printing Using Ohnesorge Number Category: Materials and Processes,” 2008.

[40] B. Derby, “Inkjet Printing Ceramics : From Drops to Solid,” vol. 10.

[41] P. Letellier, A. Mayaffre, and M. Turmine, “Drop size effect on contact angle explained by nonextensive thermodynamics . Young ’ s equation revisited,” vol. 314, pp. 604–614, 2007, doi: 10.1016/j.jcis.2007.05.085.

[42] Y. Thabet, D. Lunter, and J. Breitkreutz, “Continuous inkjet printing of enalapril maleate onto orodispersible fi lm formulations,” *Int. J. Pharm.*, vol. 546, no. 1–2, pp. 180–187, 2018, doi: 10.1016/j.ijpharm.2018.04.064.

[43] J. Mei, M. R. Lovell, M. H. Mickle, and L. Fellow, “Formulation and Processing of Novel Conductive Solution Inks in Continuous Inkjet Printing of 3-D Electric Circuits,” vol. 28, no. 3, pp. 265–273, 2005.

[44] H. Dong, W. W. Carr, and J. F. Morris, “An experimental study of drop-on-demand drop formation,” *Phys. Fluids*, vol. 18, no. 7, 2006, doi: 10.1063/1.2217929.

[45] B. W. Jo, A. Lee, K. H. Ahn, and S. J. Lee, “Evaluation of jet performance in drop-on-demand (DOD) inkjet printing,” *Korean J. Chem. Eng.*, vol. 26, no. 2, pp. 339–348, 2009, doi: 10.1007/s11814-009-0057-2.

[46] S. D. Hoath, W. K. Hsiao, S. Jung, G. D. Martin, and I. M. Hutchings, “Dependence of drop speed on nozzle diameter, viscosity and drive amplitude in drop-on-demand ink-jet printing,” *Int. Conf. Digit. Print. Technol.*, pp. 62–65, 2011.

[47] H. Wijshoff, “The dynamics of the piezo inkjet printhead operation,” *Phys. Rep.*, vol. 491, no. 4–5, pp. 77–177, 2010, doi: 10.1016/j.physrep.2010.03.003.

[48] J. Lessing, A. C. Glavan, S. B. Walker, C. Keplinger, J. A. Lewis, and G. M. Whitesides,

"Inkjet printing of conductive inks with high lateral resolution on omniphobic 'rF paper' for paper-based electronics and MEMS," *Adv. Mater.*, vol. 26, no. 27, pp. 4677–4682, 2014, doi: 10.1002/adma.201401053.

[49] G. Mattana and D. Briand, "Recent advances in printed sensors on foil," *Mater. Today*, vol. 19, no. 2, pp. 88–99, 2016, doi: 10.1016/j.mattod.2015.08.001.

[50] R. P. Tortorich and J. Choi, "Inkjet Printing of Carbon Nanotubes," pp. 453–468, 2013, doi: 10.3390/nano3030453.

[51] F. C. Krebs, "Fabrication and processing of polymer solar cells: A review of printing and coating techniques," *Sol. Energy Mater. Sol. Cells*, vol. 93, no. 4, pp. 394–412, 2009, doi: 10.1016/j.solmat.2008.10.004.

[52] J. Sun *et al.*, "Fabricating High-Resolution Metal Pattern with Inkjet Printed Water-Soluble Sacri fi cial Layer," 2020, doi: 10.1021/acsami.0c01138.

[53] N. Reis, C. Ainsley, and B. Derby, "Ink-jet delivery of particle suspensions by piezoelectric droplet ejectors," *J. Appl. Phys.*, vol. 97, no. 9, 2005, doi: 10.1063/1.1888026.

[54] A. S. Yang, C. H. Cheng, and C. T. Lin, "Investigation of droplet-ejection characteristics for a piezoelectric inkjet printhead," *Proc. Inst. Mech. Eng. Part C J. Mech. Eng. Sci.*, vol. 220, no. 4, pp. 435–444, 2006, doi: 10.1243/09544062C04305.

[55] S. A. Weissman and N. G. Anderson, "Design of Experiments (DoE) and Process Optimization. A Review of Recent Publications," 2015, doi: 10.1021/op500169m.

[56] M. Dadkhah, D. Ruffatto, Z. Zhao, and M. Spenko, "Increasing adhesion via a new electrode design and improved manufacturing in electrostatic/microstructured adhesives," *J. Electrostat.*, vol. 91, no. December 2017, pp. 48–55, 2018, doi: 10.1016/j.elstat.2017.12.005.

[57] J. Fessl, F. Mach, and J. Navrátil, "Design, fabrication and testing of electroadhesive interdigital electrodes," *Open Phys.*, vol. 16, no. 1, pp. 430–434, 2018, doi: 10.1515/phys-2018-0059.

[58] F. Carpi and E. Smela, *Biomedical Applications of Electroactive Polymer Actuators*. 2009.

[59] W. Wang and S. H. Ahn, "Shape Memory Alloy-Based Soft Gripper with Variable Stiffness for Compliant and Effective Grasping," *Soft Robot.*, vol. 4, no. 4, pp. 379–389, 2017, doi: 10.1089/soro.2016.0081.

[60] J. Shintake, S. Rosset, B. Schubert, D. Floreano, and H. Shea, "Versatile Soft Grippers with Intrinsic Electroadhesion Based on Multifunctional Polymer Actuators," *Adv. Mater.*, vol. 28,

no. 2, pp. 231–238, 2016, doi: 10.1002/adma.201504264.

[61] M. Caselli *et al.*, “Experimental characterization of a multilayer silicone-based electroactive patch for gripper applications,” p. 61, 2021, doi: 10.1117/12.2582950.

[62] J. Guo, M. Tailor, T. Bamber, M. Chamberlain, L. Justham, and M. Jackson, “Investigation of relationship between interfacial electroadhesive force and surface texture,” *J. Phys. D. Appl. Phys.*, vol. 49, no. 3, p. 35303, 2015, doi: 10.1088/0022-3727/49/3/035303.